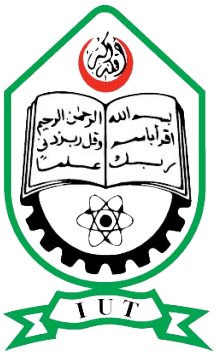

ISLAMIC UNIVERSITY OF TECHNOLOGY(IUT)

Plasmonic Coupling and Thermal Effects on Photothermal Response of Randomly Distributed Nanoparticles

Author:
Hasnat Mohammad Nayeem 190021342
Abrar Fahim 190021318
Md. Ahasanul Adib 190021310

Supervisor:
Mr. Ahmad Shafiullah
LECTURER

A thesis submitted in partial fulfillment of the requirements for the degree of Bachelor of Science (B.Sc.)

in the

Department Electrical and Electronic Engineering

Plasmonic Coupling and Thermal Effects on Photothermal Response of Randomly Distributed Nanoparticles

Approved by:

Lecturer Mr. Ahmad Shafiullah
Supervisor
Department of Electrical and Electronic Engineering
Islamic University of Technology (IUT)
Boardbazar, Gazipur-1704

Date:

Declaration of Authorship

This is to attest that the work presented in this thesis titled, **"Plasmonic Coupling and Thermal Effects on Photothermal Response of Randomly Distributed Nanoparticles"** is the product of research carried out by the students under the supervision of Mr. Ahmad Shafiullah. Lecturer, Department of Electrical and Electronic Engineering (EEE), Islamic University of Technology (IUT).
This work was entirely conducted during our candidacy for a Bachelor of Science (B.Sc) degree at this University. There has been no prior submission of any part of this thesis for any other qualification or degree at this university. Any published work of others and all the main sources of help that were consulted in this thesis have been carefully acknowledged. The sources have been comprehensively cited in cases where a work has been quoted. Apart from any such quotations, this thesis is entirely our own work.

Hasnat Mohammad Nayeem
Student ID: 190021342

Abrar Fahim
Student ID: 190021318

Md. Ahasanul Adib
Student ID: 190021310

ISLAMIC UNIVERSITY OF TECHNOLOGY(IUT)

Abstract

Department Electrical and Electronic Engineering

Bachelor of Science (B.Sc.)

Plasmonic Coupling and Thermal Effects on Photothermal Response of Randomly Distributed Nanoparticles

by Hasnat Mohammad Nayeem 190021342
Abrar Fahim 190021318
Md. Ahasanul Adib 190021310

Plasmonic coupling has attracted considerable attention in research due to its promising applications in thermoplasmonics, which is increasingly utilized across various nanotechnologies, particularly in the fields of biology and medicine. Applications include photothermal cancer therapy, drug delivery, nanosurgery, and photothermal imaging, thanks to their capability to significantly enhance electromagnetic fields. Localized Surface Plasmon Resonances (LSPR) in metal nanostructures enable substantial electromagnetic field enhancement and precise localization at the nanoscale. The characteristics of LSPR, including the resonance wavelengths, can be adjusted by altering the geometry of the nanostructures and are highly sensitive to changes in the surrounding refractive index. The interaction of localized plasmon resonances can lead to the formation of new hybrid modes that individual nanostructures cannot support, surmounting some limitations of standalone LSPR and facilitating novel applications and the active manipulation of plasmon resonances.
In this thesis work, we explore how plasmonic coupling influences the photothermal behavior of randomly distributed silver nanoparticles. We used the discrete dipole approximation method and thermal Green's function to compute the spatial temperature profiles of illuminated nanoparticles. Our findings suggest that plasmonic coupling among nanoparticles in a random assembly, along with thermal accumulation, induces a photothermal response that differs from that observed in isolated nanoparticles. We qualitatively analyzed the individual effects of plasmonic coupling and thermal accumulation on temperature increases in nanoparticle assemblies. Our results indicate that at wavelengths far from a single nanoparticle's plasmonic resonance, plasmonic coupling among clustered nanoparticles can lead to significant temperature increases, an effect not anticipated in the absence of plasmonic coupling. Conversely, at the resonance wavelength of a single nanoparticle, plasmonic coupling results in a lesser temperature rise compared to a group of non-coupled nanoparticles. These insights enhance our understanding of the photothermal dynamics in random nanoparticle systems, with significant implications for their use in biological applications.

Acknowledgements

In the name of Allah, the Most Benevolent, the Most Merciful. At the commencement of this literature, we would like to express our sincerest gratitude to Almighty Allah who has most graciously granted us the knowledge, skills, and competence to carry out this engineering exploration. It is by His blessings, that we were able to outlast all the challenges on the way to this milestone. This work stands as a testament that through perseverance, hard work, and faith, aspirations can be turned into achievements.

Foremost, we are profoundly grateful to our supervisor, Mr. Ahmad Shafiullah, whose unyielding support has been a guiding beacon throughout the entirety of this journey. His deep insights into the subject matter, combined with his immense patience and belief in our capabilities have greatly enriched our academic experience and overall work ethic. To him, we extend a heartfelt gratitude for his indispensable contribution.

We are immensely indebted to our Professor Dr. Rakibul Hasan Sagor for his vast knowledge in this field of engineering and guiding us properly along the way.

We would also like to thank IUT Photonics Research Group(IUTPRG) for the encouragement and valuable resources. They have been a continuous source of support and motivation for each one of us. We would also like to express our gratitude to Mr. A.K.M Rakib for overseeing us constantly throughout our journey.

Finally, we express our heartfelt gratitude to our family, friends, who have shared this journey with us through the best and worst of times providing constructive criticism, moral support and priceless camaraderie. Their encouragement and kindness were essential for our enthusiasm and morale.

This work would not have been possible without the combination of all these efforts and influences. We would like to reiterate our sincerest appreciation for everyone who has been a part of our academic journey.

Contents

List of Figures

List of Tables

Chapter 1

Introduction

Noble metal nanoparticles (NPs) have received over the last decade much interest in nano science due to their remarkable optical properties. [1] In particular, noble metal nanoparticle (NP) under illumination at its plasmonic resonance, which can be tuned from the visible to the infrared frequency ranges, strongly absorbs the light energy. The absorbed energy is converted to heat which raises the temperature of nanoparticle and its immediate surrounding media. [2] These resonances, known as localized surface plasmons (LSPs), are responsible for both enhanced light scattering and enhanced light absorption. For a long time, the absorption and the subsequent NP temperature increase have been considered as side effects in plasmonics applications, which focused on the optical properties of metal NPs. Only recently have scientists realized that this enhanced light absorption, turning metal NPs into ideal nano-sources of heat remotely controllable using light, provides an unprecedented way to control thermal-induced phenomena at the nanoscale.

In this research work, we review the recent progress in the emerging and fast-growing field of thermo-plasmonics. Which investigates the use of plasmonic structures as nano sources of heat. We first describe the physics of heat generation in metal NPs. In particular, we emphasize the differences in the heating mechanisms between continuous and pulsed illuminations. Then, we present the numerical frameworks that have been developed to model the photothermal properties of metal NPs. We also discuss recent experimental works that aim at addressing the intricate problem of probing and imaging the temperature distribution generated around plasmonic nanostructures. Finally, we review the main emerging applications in thermo-plasmonics, from medical therapy and bio-imaging to nano-chemistry and optofluidics.

1.1 Background and Motivation

Over the last two decades, noble metal nanoparticles (NPs) have been the subject of extensive research in the frame of nanotechnology, mainly owing to their unique optical properties. Indeed, the free electron gas of such NPs features a resonant oscillation upon illumination in the visible part of the spectrum. The spectral properties of this resonance depend on the constitutive material, the geometry of the NP and its environment. This resonant electronic oscillation is called localized surface plasmon (LSP), and the field of research that studies the fundamentals and applications of LSP is known as nanoplasmonics. 1 LSPs are accompanied by valuable physical effects such as optical near-field enhancement, heat generation and excitation of hot-electrons. Hence, plasmonic NPs can behave as efficient nanosources of heat, light or energetic electrons, remotely controllable by light. In nanoplasmonics, these properties have stimulated extensive basic research and already led to a wide range of applications in nanotechnologies. Light and heat are physical quantities involved in many mechanisms in physics, chemistry and biology. Hence, a natural trend is to explore possible frameworks that could gain from the unique properties of metal NPs. So far,

biology has been one of the areas of science that has benefited the most from nanoplasmonics. For instance, gold NPs as nanosources of heat are already at the basis of applications ranging from photothermal cancer therapy [3]–[5], bio-imaging [6], drug delivery [7] and nanosurgery [8]. Chemistry is another field of science that can potentially greatly profit from plasmonic NPs. Indeed, heat is a major parameter in any chemical reaction, light can be used to achieve high selectivity in chemical mechanisms thanks to quantum selection rules and adjustable photon energies, and electron transfer is the basis of redox reactions. Hence, the idea to use metal NPs as efficient nanosources of heat, light and electrons appears to be an appealing concept to both boost the yield of chemical reactions and improve their spatial and temporal control. The first section gives the readers the basics of nanoplasmonics.

1.2 Principles of Plasmonic Effect

The free electron gas in a solid, when moving against a positive background of ions, may be regarded as plasma. Just as a wave of light can be quantified as a photon and a lattice vibration can be quantified as a phonon, the collective oscillation of the free electron gas in a solid's positive ion background can be regarded as an elementary excitation that can also be quantized as a type of quasiparticle, i.e., the plasmon. As we know, the momentum matching condition can be tuned for different wavelengths by changing the incident angle of the plane wave. Depending on their different boundary conditions, plasmons in metals can be divided into bulk plasmons and surface plasmons (SPs). Furthermore, surface plasmons can be subdivided into two categories: the first is conductive **Surface Plasmon Polaritons (SPPs)**, which occur at the metal-dielectric interface in the form of longitudinal waves, and the second is **Localized Surface Plasmons (LSPs)**, which are bound near metal structures. These three different forms are illustrated in **figure: 1.1**.

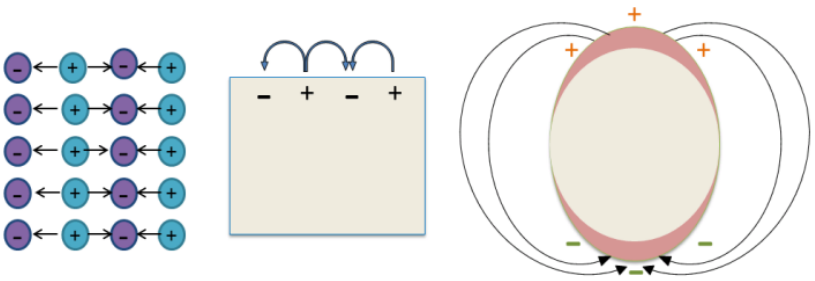

FIGURE 1.1: Three different oscillations. Adapted from Ref. [8]

As collective photon–electron oscillations makes them attractive candidates for energy applications, when light is incident on metal, it can lead to plasma oscillation inside the metal, and when the metal has boundaries, such as a metal-dielectric interface or a boundary of the metal nanoparticles' geometry, the field will be coupled with the plasmon oscillation within the metal and will form a new oscillation mode, i.e., a conductive surface plasmon oscillation or a localized surface plasmon oscillation.

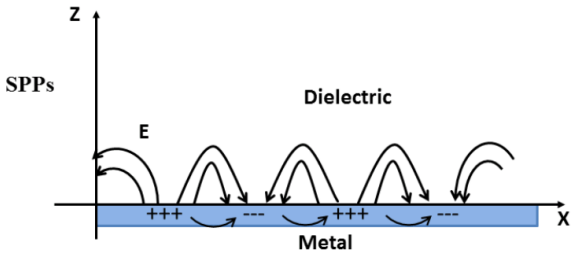

FIGURE 1.2: Surface Plasmon Polaritons

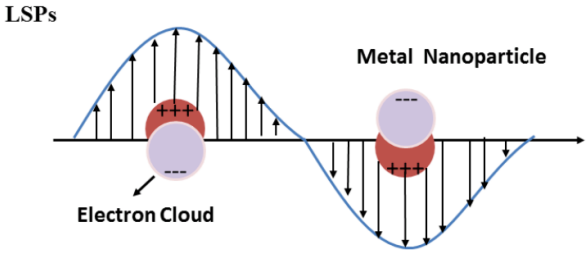

FIGURE 1.3: Localized Surface Plasmons

figure: 1.3. depicts the nanostructures of the surface plasmon polaritons (SPPs) and the localized surface plasmons (LSPs). In SPPs, the free electrons interact with the electromagnetic fields to generate dense electron waves that propagate along the metal surface [9], thus requiring one-dimensional metal structure which is close to the excited wavelength. In general, the wave vector of SPP dispersion curve is larger than that of the light while the frequency remains the same, the SPP dispersion relation can be calculated for short-pitch metal gratings for various depths, the dispersion of electromagnetic surface mode can be obtained and described by

$$k_{spp} = k_0 \sqrt{\frac{\epsilon_1 \epsilon_2}{\epsilon_1 + \epsilon_2}} \tag{1.1}$$

where k_{spp} is the wave vector of the SPP, k_0 is the wave vector of the incident radiation, and ϵ_1 and ϵ_2 are the frequency-dependent dielectric functions of the two media on either side of the interface [10].

The theory here is based on the characteristics of surface plasmons when coupled with some excitons, which are confined to the metal surface on a nanometer scale and thus greatly compressed the spatial distribution of the electromagnetic field. This forms a theoretical basis for exploration of the coupling effect between surface plasmons and excitons.

1.3 Problem Statement

The main concern of this paper is to find the answer of this question. In this paper, we use the discrete dipole approximation (DDA) method and thermal Green's function [8], [11] to investigate the effects of plasmonic coupling and thermal superposition on temperature increase of randomly distributed nanoparticles. To the best of our knowledge, this is the first study that determines quantitatively the separate contributions of each of these two effects to the photothermal behavior of illuminated NPs assembly. Here, we have considered silver NPs because silver NPs, due to their stronger and sharper plasmon resonance, recently

have been intensively used in diagnosis and the treatment of cancer and as the drug carriers [5], [6], [12]–[16]. As an experimentally relevant example of the structure that we have investigated in this paper, one can consider the application of NPs as nano-source of heat in aqueous medium such as in medicine and biology.

In general, when the NPs interact, the photothermal behavior of each NP in the distribution can be very different in comparison with a single isolated NP. In fact, in an assembly of NPs, two different effects determine the photothermal properties of each NP; the effect of plasmonic coupling with the other NPs and thermal accumulation effect. While extensive studies made on plasmonic coupling for a pair of nanoparticles [17]–[23], there is much less effort being expended on the ensemble of random NPs. The important question that arises about the effect of plasmonic coupling on the photothermal behavior of random NPs is that will plasmonic coupling work in favor of the application, because of the field enhancement? Or will it work against it, because it shifts the plasmonic resonance wavelength? The main concern of this paper is to find the answer of this question. In this paper, we use the discrete dipole approximation (DDA) method and thermal Green's function [8], [11] to investigate the effects of plasmonic coupling and thermal superposition on temperature increase of randomly distributed nanoparticles.

Why and how Plasmonic Coupling effects on photothermal ?

- **Enhanced Sensitivity :** Plasmonic coupling enhances the sensitivity of sensors by increasing the local electromagnetic field.
- **Improved Photothermal Efficiency:** Coupling leads to higher temperature increases, beneficial for applications like Photothermal Imaging and Cancer therapy
- **Efficient Heat Generation :** Coupled nanoparticles can generate more heat, making treatments like hyperthermia therapy more effective.
- **Advanced Nanophotonic Devices :** Enables the development of devices with enhanced optical properties for use in telecommunications and computing.

1.4 Plasmonics in applications

The optical properties of metals have a huge potential for applications. The range of application based on the plasmonic properties is very wide such as enhanced spectroscopies, bio and chemical sensing, solar cells, color generation, heat treatment, sub-wavelength optical imaging and plasmonic lasing.

1.4.1 Color Generation

The plasmonic properties of metallic nanoparticles is used for ages in order to create the colors in mesoscale. The most popular examples are the Lycurgus Cup produced in Roman Empire (4^{th} century). The glass of this cup contains gold and silver powder.

When the cup is shined from outside (Fig. 1.9a) it looks green due to the scattering caused by LSPR in green range. When the cup is shined from inside (Fig. 1.9b) glass

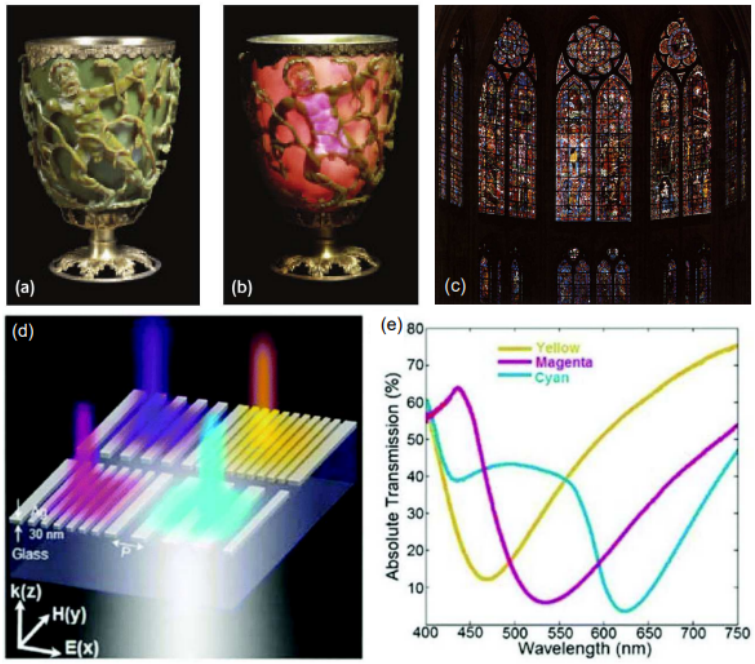

FIGURE 1.4: Lycurgus roman cup (a) in reflected (b) and in transmitted light [37]. (c) Stained glasses on the vitrines of the Cathedral of Troyes. (d) Schematic of the grating color filter of 30 nm thick Ag grating with different periods. (e) Measured transmission spectra corresponding to yellow, magenta and cyan colors for the structure in (d). [24]

appear to be red due to the LSPR causing absorption in the green range. Another example of a color generation caused by the optical properties of metallic nanoparticles is pictured on the **figure: 1.4c**. The progress in nanofabrication processes allow to produce nano or microstructures of different configurations show a color generation at microscale using nanostructured silver pallets of different size and periods (distance between the pallets) [24]. **figure: 1.4d** is shown the schematics of different pallets and on the **figure: 1.4e** is drawn the transmission spectra obtained experimentally. We can see the clusters show different colors at nanoscale, which can be used for examples for high resolution screens with very small pixel size.

1.4.2 Bio-Sensing

Multiple papers have been published on a bio-chemical sensing based on plasmonic resonances. Cooper reviewed an example of plasmonic sensor in order to determine the affinity and kinetics of a wide variety of molecular interactions in real time, without the need of molecular labeling **figure: 1.5**. This kind of bio-sensor is envisaged to characterize the interactions between receptors that are attached to the biosensor surface and ligands that are in solution above the surface. SPR is changed due to the refractive index changes in the intermediate.

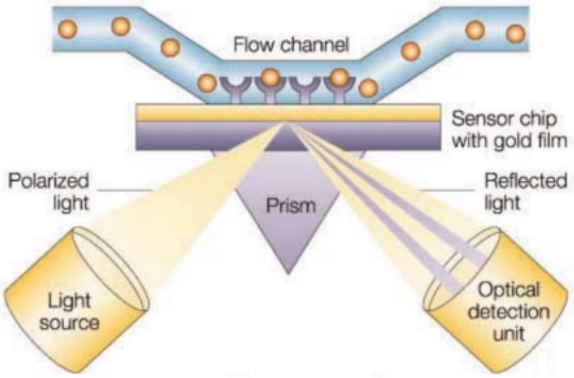

FIGURE 1.5: Experimental setup for an SPR based biosensor. SPR detects changes in the refractive index in the immediate vicinity of the surface layer of a sensor chip. SPR s observed as a sharp shadow in the reflected light from the surface at an angle that is dependent on the mass of material at the surface. (The figure and the caption are adopted from [24])

SPR is observed as a dip in the reflected light spectrum from the surface at an angle that is dependent on the refractive index of solution [24]. The refractive index of the solution defined by mass of "ligands". Besides the SPR, the LSPR changes caused by the refractive index variation can be used in biosensing. The molecules bound in the vicinity of nanoparticles causes a change of the effective refractive index, which leads to a shift of the resonance peak position.

Horrer et al. showed experimentally and numerically a nice example of a sensor based on LSPR. They used an array of MIM (metal-insulator-metal) structures for the sensing. In Fig. **??**a is shown the single element schematic of the array.

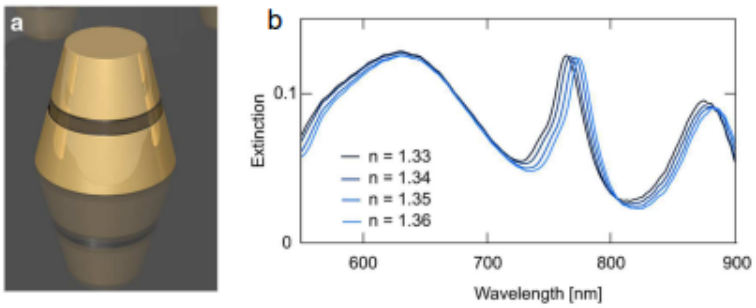

FIGURE 1.6: (a) Schematic of the vertical gold–SiO2–gold dimer. (b)Sensitivity measurements in water–glycerin solutions with different mixing ratios to vary the refractive index. [25]

The array shows three peak position corresponding respectively to symmetric dipole (around 630 nm), lattice mode (around 770 nm) and antisymmetric dipole mode (around 880 nm). The main resonance shifts are recorded for lattice mode and anti-symmetric dipole mode, when the water–glycerin solutions of different refractive indexes are tested. They demonstrate a sensor based on LSPR, which is sensitive for refractive indexes changes with step of 0.01. The highest sensitivity was reported as 0.003 [26].

1.5 Thesis Outline

The dissertation thesis is organized into ten chapters that cover the various aspects of Principles of Plasmonics, introduction to plasmonic coupling effectts on nanoparticles applications.
Following the thesis introduction in Chapter 1, Chapter 2 offers an overview of introduction to plasmonics of Nanoparticles. Chapter 3 delves into the theory of plasmonic of photothermal response. Chapter 4 discusses the Numerical Methods for Plasmonic Coupling. Chapter 5 covers the Light Scattering and Absorption by Nanoparticles Chapter 6 presents the theoretical Calculation of Temperature Distribution in the steady state regime. Chapter 7 discusses the experimentals methods, set up, structure of Experiments and Outcomes. Chapter 8 is basically Result analysis and conclusion of our whole thesis work. Chapter 9 discussed compares advantages and disadvantages, and explores various nanoparticles applications and future directions of the investigated approaches. PICs. Finally, Chapter 10 presents the Demonstration of Outcome Based Education.

Chapter 2

Introduction to Plasmonics of Nanoparticles

The interaction of an external electromagnetic (EM) wave and the conduction band electrons at a metal interface may result in plasmons [27]–[29]. It is defined commonly as a quantum of plasma oscillations [30], whose theory was proposed by Pines and Bohm in 1952 [29]. Plasmons often refer to plasmon polaritons which is the coupled state between plasmon and photon. Wood in 1902 published firstly an experimental observation anomalies caused by surface plasmon polaritons [31]. He noticed dark stripes in the spectrum of the diffracted light, when a metallic diffraction grating was illuminated by a polychromatic light. The dark stripes represent the losses of the light in the grating at certain wavelengths, which were not transmitted. This phenomenon is known as Wood-Raleigh anomalies. In 1957 Ritchie predicted that the electron energy losses should describe the collective modes (surface plasmons) of metal thin films . Then, in 1959 Powel and Swan verified experimentally the concept proposed by Ritchie.

2.1 Plasmons

The term **plasmon** was introduced by *Pines* in 1956 in the introduction of a review article [32]. In Pines' work we find the following definition:

The valence electron collective oscillations resemble closely the electronic plasma oscillations observed in gaseous discharges. We introduce the term 'plasmon' to describe the quantum of elementary excitation associated with this high-frequency collective motion. A plasmon is therefore a quantum quasi-particle representing the elementary excitations, or modes, of the charge density oscillations in a plasma. Note that the study of these oscillations started earlier, even if they were not known or identified as plasmons [33]. We will come back to the notion of elementary excitations or modes of a system in the next section. Although the term 'plasmon' is sometimes used in a broader context, the formal definition given above is the definition of reference. It draws its origin from quantum mechanics, even though we will see that quantum mechanics is, in fact, not necessary to study plasmons. A useful analogy to understand the meaning of this definition is to recall the formal definition of a photon: it is the quantum particle representing the elementary excitations, or modes, of the free electromagnetic field oscillations.

A plasmon is therefore simply to the plasma charge density what photons are to the electromagnetic field. Many properties of photons can be studied within a classical framework, using Maxwell's equations. Similarly, many properties of plasmons can be studied within a classical description of the plasma and its interactions. There is, may be, a small difference in the vocabulary between plasmons and photons, but it is only artificial: people typically

only use the term 'photon' when dealing with quantum aspects of the electromagnetic fields (such as absorption or emission by an atom). In classical situations, the term electromagnetic wave, or electromagnetic mode, is usually preferred. For reasons that are more historical than scientific, the term 'plasmon' tends to be used in all situations, quantum or classical, instead of equivalent (classical) denominations such as charge density oscillations . A more important and fundamental difference is that a photon is a real quantum particle while a plasmon is a quasi-particle because it is always 'lossy' and highly interacting. A charge density oscillation, if not maintained by an external source of energy, will always decay because of various loss mechanisms (collisions, etc.).

2.2 Maxwell's Equations

The interaction of light with metals and dielectrics can be described by Maxwell's equations, which provide the mathematical framework to describe the behavior of the electric field **B** and magnetic field **H** to their sources. At their fundamental level, Maxwell's equations are formulated without the consideration of specific material properties [34]

$$\begin{aligned} \nabla \cdot \mathbf{D} &= \rho_{\text{ext}} \\ \nabla \cdot \mathbf{B} &= 0 \\ \nabla \times \mathbf{E} &= -\frac{\partial \mathbf{B}}{\partial t} \\ \nabla \times \mathbf{H} &= \frac{\partial \mathbf{D}}{\partial t} + \mathbf{J}_{\text{ext}} \end{aligned} \tag{2.1}$$

where **B** is the magnetic flux density, ρ is the charge density, **J** is the current density, and **D** is the electric displacement field. When considering electromagnetic fields in a vacuum, these equations can be expressed as follows:

$$\begin{aligned} \nabla \cdot \mathbf{D} &= \rho_{\text{ext}} \\ \nabla \cdot \mathbf{B} &= 0 \\ \nabla \times \mathbf{E} &= -\frac{\partial \mathbf{B}}{\partial t} \\ \frac{1}{\mu_0} \nabla \times \mathbf{H} &= \frac{1}{\epsilon_0} \frac{\partial \mathbf{E}}{\partial t} + \mathbf{J}_{\text{ext}} \end{aligned} \tag{2.2}$$

where, in the last equation, the constants ϵ_0 and μ_0 represent the vacuum electrical permittivity and vacuum magnetic permeability, respectively. In vacuum, the relationship between electric displacement and electric field, and the magnetic flux density and the magnetic field is:

$$\begin{aligned} \mathbf{D} &= \epsilon_0 \mathbf{E} \\ \mathbf{B} &= \mu_0 \mathbf{H} \end{aligned} \tag{2.3}$$

2.3 Properties of metals

2.3.1 Optical Properties

The optical properties of metals depend strongly on the frequency of EM wave. The metals are highly reflective for frequencies up to visible and EM cannot propagate through. In Fig. 1.1 is shown the chart of the light frequency versus the wavelength.

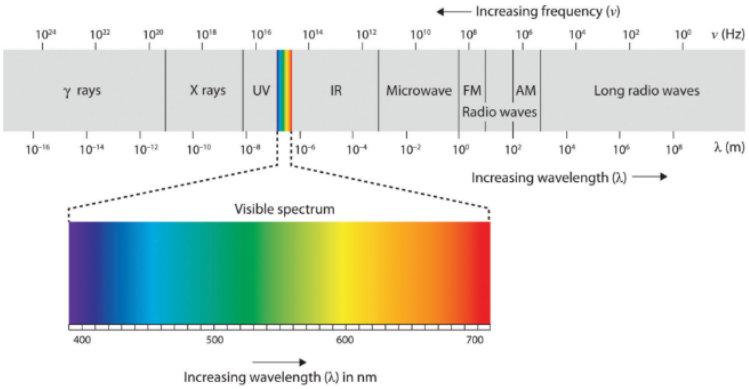

FIGURE 2.1: Light wavelength versus frequency chart [34]

At high frequencies (UV-γray) the majority of metals demonstrate dielectric-like character allowing EM field to penetrate through. It depends on their electronic band structure, for example alkali metals (Li, Na, K, Rb, Cs, Fr) are transparent in UV. Though, the noble metals (Au, Ag, Cu) have strong absorption in UV caused by interband transitions. These are described by the complex dielectric function called dielectric permittivity - $\epsilon(\omega)$. In other words, $\epsilon(\omega)$ draws the dispersive properties of metals. $\epsilon(\omega)$ is governed by the conduction band electrons and inter-band transitions. The conduction electrons are generally described by the Drude model. Following the Drude model's description, the conduction electrons form an electron gas and move freely through a metal. The illustration of the Drude model is shown in Fig. 2.1 The basic assumptions are that electron-electron and ion-interactions are neglected, and electrons move in straight line in the absence of electric field. Moreover, they achieve thermal equilibrium by collision with lattice. The collisions are interpreted by the kinetic theory. The mean free time (relaxation time) between collisions is τ and the probability of collisions is $1/\tau$.

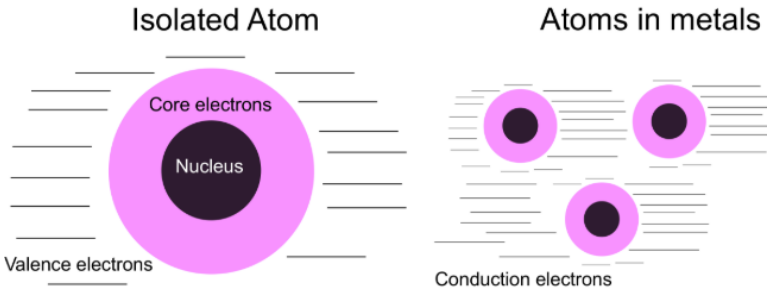

FIGURE 2.2: Drude model representation [34]

When the electric field is applied the valence electrons are displaced by $\vec{r}$ and induce a macroscopic polarization ($\vec{P}$):

$$\mathbf{P} = -n \cdot e \cdot \mathbf{r}, \quad n = \frac{N}{V} \tag{2.4}$$

where in the equation (2.18), n is the electron density per unit volume (V), e is the electron charge, N is the number of electrons. Let's link the polarization and the dielectric function.

2.3.2 Materials Properties

Equations (2.3) can be used to calculate the fields where all sources are known. In bulk materials, this would mean knowing the exact charges and positions of all atoms at any given

time. However, computing the exact number of individual contributions when dealing with complex systems is often impossible and unnecessary. Instead, it is common practice to calculate average macroscopic fields using material equations. These equations express the impact of the fields on the material's structure observed over large distances. By employing material equations, one can effectively describe the effects of the material's microstructure without needing to consider every individual component. In this case, equations (2.3) can be reformulated as follow [35]:

$$\begin{aligned} \mathbf{D} &= \epsilon_0 \mathbf{E} + \mathbf{P} = \epsilon_0 (1 + \chi_e) \mathbf{E} \\ \mathbf{B} &= \mu_0 \mathbf{H} + \mathbf{M} = \mu_0 (1 + \chi_m) \mathbf{H} \end{aligned} \tag{2.5}$$

where $\mathbf{P}$ is the polarization, χ_e is the electric susceptibility tensor, χ_m is the magnetic susceptibility tensor, and $\mathbf{M}$ is the magnetization. $\mathbf{P}$ is the polarization is

$$\mathbf{P} = \epsilon_0 \chi_e \mathbf{E}$$

Polarization and magnetization represent the distribution of electric and magnetic dipole moments that arise in response to an external field. This implies that both of these vectors are functions of the external field. As a result, when the expressions (2.5) for the electric displacement and magnetic field are substituted into the equations (2.3), the Maxwell's equations in the medium have a similar form to those in a vacuum. For non-magnetic materials and most materials within the optical frequency spectrum, the magnetization component $\mathbf{M}$ can be neglected. Two new constants can be introduced:

$$\begin{aligned} \epsilon_r &= (1 + \chi_e) \\ \mu_r &= (1 + \chi_m) \end{aligned} \tag{2.6}$$

called relative electric permittivity and relative magnetic permeability. Using these notations, the displacement and magnetic induction can be written in a simpler form:

$$\begin{aligned} \mathbf{D} &= \epsilon_0 \epsilon_r \mathbf{E} \\ \mathbf{B} &= \mu_0 \mu_r \mathbf{H} \end{aligned} \tag{2.7}$$

Also, $\mathbf{D} = \epsilon_0 \epsilon_r \mathbf{E} = \epsilon_m \mathbf{E}$ and $\mathbf{B} = \mu_m \mathbf{H}$ where ϵ_m and μ_m are permittivity and permeability of the medium respectively.Finally, Maxwell equations take the form of

$$\begin{aligned} \nabla \cdot \mathbf{E} &= \frac{\rho_{\text{ext}}}{\epsilon_m} \\ \nabla \cdot \mathbf{B} &= 0 \\ \nabla \times \mathbf{E} &= -\frac{\partial \mathbf{B}}{\partial t} \\ \nabla \times \mathbf{B} &= \mu_m \epsilon_m \frac{\partial \mathbf{E}}{\partial t} + \mu_m \mathbf{J}_{\text{ext}} \end{aligned} \tag{2.8}$$

In the absence of external current and charge, by taking curl of 2nd equation 2.10 and then inserting 3rd equation into it, one can obtain

$$\nabla \times \nabla \times \mathbf{E} = -\mu_0 \frac{\partial^2 \mathbf{D}}{\partial t^2} \tag{2.9}$$

By using vector identity ($\nabla \times \nabla \times \mathbf{E} = \nabla(\nabla \cdot \mathbf{E}) - \nabla^2 E$) and being aware of , in this case, one can form an electromagnetic wave equation

$$\nabla^2 \cdot \mathbf{E} = \mu_m \sigma \frac{\partial \mathbf{E}}{\partial t} + \mu_m \epsilon_m \frac{\partial^2 \mathbf{E}}{\partial t^2} \tag{2.10}$$

where σ is the conductivity of the metal which come from the ohms law $\mathbf{J}_{ext} = \sigma \mathbf{E}$. Assuming a harmonic form for E-field- $\mathbf{E}(t) = \mathbf{E}(\mathbf{r})e^{-i\omega t}$ inserting $\mathbf{E}(t)$ into 2.11, Helmholtz wave equation can be obtained.

$$\nabla^2 \cdot \mathbf{E} + \omega^2 \mu_m \epsilon_m \mathbf{E}(\mathbf{r}) = 0 \tag{2.11}$$

where ϵ is known as so-called complex permittivity in the form of

$$\epsilon(\omega) = \epsilon'(\omega) + \frac{j\sigma(\omega)}{\omega} \tag{2.12}$$

Here conductivity is also complex and to understand this complex behavior one should be aware of Drude –Sommerfeld model. Valence electrons in a metal behave like a gas of free electrons and oscillate with respect to immobile ion cores. Electronelectron and electron-ion interactions that occur because of collisions are ignored and collisions are assumed instantaneous in the Drude-Sommerfeld model. It describes the response of the electrons to an external driving field revealing information on the optical properties of metals.

2.4 The microscopic response of the medium

Metals such as gold and silver that are well suited for plasmonic applications are well described by the Drude model. In this picture, the metals consist of fixed ion cores, surrounded by freely moving conduction electrons. The electrons do not interact with one-another, but occasionally collide instantaneously and elastically with the ion cores. The Drude model can be derived as a special case of the Lorentz model of the optical polarisability

2.4.1 The Lorentz model

The Lorentz model of the optical polarisability[8] treats a medium as a collection of classical driven damped harmonic oscillators. For an oscillator of mass m, natural frequency ω_0 and damping coefficient γ, displaced from equilibrium a distance $\mathbf{r}$ (assumed small) by force F,

$$\mathbf{F} = m(\frac{d^2\mathbf{r}}{dt^2} + \gamma \frac{d\mathbf{r}}{dt} + \omega_0^2 \mathbf{r}) = -e\mathbf{E} \tag{2.13}$$

For our case the displacing force is created by an electric field $\mathbf{E}$, and acts on electron charge e. Using complex notation for $\mathbf{E}$ and r oscillating at a single frequency ω with time dependence contained in a $e^{-i\omega t}$ factor, and substituting m by the electron effective mass m^* we find-

$$\mathbf{r} = \frac{e\mathbf{E}}{m^*(-\omega^2 - i\gamma\omega + \omega^2)} \tag{2.14}$$

The complex dipole moment $\mathbf{p}$ induced by the charge separation $\mathbf{r}$ is $\mathbf{p} = -e\mathbf{r}$. The linear polarisability α is defined as $\mathbf{p} = \alpha\mathbf{E}$, i.e.

$$\alpha = \frac{e^2}{m^*(-\omega^2 - i\gamma\omega + \omega^2)} \tag{2.15}$$

The macroscopic polarisation of a medium P is linked to its dielectric function by $\epsilon(\omega) = 1 + \frac{\mathbf{p}}{\epsilon_0 \mathbf{E}}$. Assuming that oscillators are non-interacting, we can simply sum all the individual microscopic polarisabilities to find $\mathbf{p}$. So for n electrons, $\mathbf{p} = n\alpha\mathbf{E}$ and

$$\alpha = 1 + \frac{ne^2}{m^*\epsilon_0(-\omega^2 - i\gamma\omega + \omega^2)} \tag{2.16}$$

2.4.2 The Drude model

Ignoring the magnetic field, $\mathbf{B}$, we start by considering an external incident light on a metallic surface. [31] The spatial variation of the field is also ignored. This is acceptable unless the field varies much over distances comparable with the electrons mean free path. In the Drude model, equation of the motion for an electron is

$$m^* \frac{d\mathbf{v}(t)}{dt} = -\frac{m^*}{\tau}\mathbf{v}(t) - e\mathbf{E}(t) \tag{2.17}$$

where e and m^* are charge and effective mass of the electrons in a crystal respectively and τ is the relaxation time. Assuming the driving $\mathbf{E}$-field has harmonic time dependence, $\mathbf{E}(t) = \mathbf{E}_0 e^{-i\omega t}$, and substituting $\mathbf{E}(t)$ into equation (2.16) gives mean velocity as,

$$\mathbf{v}(t) = -\frac{e\tau}{m^*(1 - i\omega\tau)}\mathbf{E}(t) \tag{2.18}$$

which is in the form of $\mathbf{v}(t) = \mathbf{v}_0 e^{-i\omega t}$. By substituting $\mathbf{v}(t)$ into the current density equation, $\mathbf{J}_{\text{ext}} = -ne\mathbf{v}$, one can get

$$\mathbf{J}_{\text{ext}} = \frac{ne^2\tau}{m^*(1 - i\omega\tau)}\mathbf{E}(t) \tag{2.19}$$

where n is the number of conduction electrons per unit volume. Comparing equation (2.19) with Ohm's law $\mathbf{J}_{\text{ext}} = \sigma\mathbf{E}$, conductivity is obtained as

$$\sigma = \frac{ne^2\tau}{m^*(1 - i\omega\tau)} \tag{2.20}$$

By using the complex permittivity equation $\epsilon(\omega) = \epsilon'(\omega) + \frac{i\sigma(\omega)}{\omega}$ which will be obtained from Helmholtz wave equations in part 2.18, an expression for the complex permittivity can be derived as

$$\epsilon(\omega) = \epsilon'(\omega) - \frac{\omega_p^2\epsilon_0}{\omega^2 + i\omega/\tau} \tag{2.21}$$

where ω_p is defined as the plasma frequency;

$$\omega_p^2 = \frac{ne^2}{\epsilon_0 m^*} \tag{2.22}$$

In equation (2.21) the first term is the result of the bound charges in metal and the second one is due to the free electrons. By dividing both sides of the equation, the relative complex permittivity ($\epsilon_r = \epsilon_m/\epsilon_0$) takes the form of

$$\epsilon_r = 1 - \frac{\omega_p^2}{\omega^2 + i\omega/\tau} \tag{2.23}$$

$$\epsilon_r = 1 - \frac{\omega_p^2}{\omega^2 + i\gamma\omega}, \quad \gamma = \frac{1}{\tau} \tag{2.24}$$

To get a better understanding, we separate equation 2.23 into its real and imaginary parts in the form of $\epsilon_r = \epsilon_r' + i\epsilon_r''$, that gives the results,

$$\epsilon_r' = 1 - \frac{\omega_p^2 \tau^2}{1 + \omega^2 \tau^2} \tag{2.25}$$

$$\epsilon_r^{'} = 1 - \frac{\omega_p^2}{\gamma^2 + \omega^2}, \quad \gamma = \frac{1}{\tau} \tag{2.25}$$

$$\epsilon_r'' = \frac{\omega_p^2 \tau^2}{\omega(1 + \omega^2 \tau^2)} \tag{2.25}$$

For the wavelengths that are visible or shorter $\omega\tau \gg 1$ and $\tau \approx 10^{-15}$ s at room temperature [22], so ϵ_r' (real part) can be estimated as

$$\epsilon_r' \approx 1 - \frac{\omega_p^2}{\omega^2} \tag{2.26}$$

- For $\omega < \omega_p$ equation (2.26) becomes negative. Negative real relative permittivity makes metals highly reflective.
- On the other hand $\omega > \omega_p$ condition makes ϵ_r' positive and Helmholtz wave equation (2.15) give oscillatory solutions and the metal becomes transparent.

Therefore, it can be concluded that plasma frequency is the frequency that metal starts to be transparent against the incoming light. The coupling of plasma to the incoming light is the simplest explanation of the formation of SPPs. The major condition in this coupling event is the resonance with plasma frequency.

2.4.3 Interband transitions and real metals

The Drude-Sommerfeld model gives quite precise results for the optical properties of metals in the infrared regime. However it needs to be extended in the visible range by considering the response of bound electrons as well. As an example, for gold, at wavelengths those are shorter than 550 nm, imaginary part of the measured dielectric function increases much more strongly as stated by the Drude-Sommerfeld theory [36]. The reason is that electrons of lower-lying bands can be promoted into the conduction band by higher energy photons. Excitation of the oscillation of bound electrons may describe such transitions, in a classical picture. The equation of motion for a bound electron reads as

$$m\ddot{x} + m\gamma\dot{x} + m\omega_0^2 x = -eE \tag{2.27}$$

where m is the effective mass of the bound electron, which is in general different from the effective mass of a free electron in a periodic potential, γ is the damping constant, and ω_0 is the bound electron resonance frequency. Solving the equation (2.27) to model $\epsilon_r(\omega)$ for noble metals leads us to a term in the form of

$$\epsilon_r(\omega) = 1 + \frac{\omega_p^2}{\omega_0^2 - \omega^2 - i\gamma\omega} \tag{2.28}$$

called the Lorentz oscillator term due to its resonant nature besides the free electron result in the equation 2.23. Equation 2.28 can be rewritten by separating it into real and imaginary parts as $\epsilon_r = \epsilon_r' + i\epsilon_r''$ where

$$\epsilon_r' = 1 + \frac{(\omega_0^2 - \omega^2)\omega_p^2}{(\omega_0^2 - \omega^2)^2 + \gamma^2\omega^2} \tag{2.29}$$

and

$$\epsilon_r'' = \frac{\gamma\omega\omega_p^2}{(\omega_0^2 - \omega^2)^2 + \gamma^2\omega^2} \tag{2.30}$$

While the real part of the equation shows dispersion-like behavior, the imaginary part shows resonant behavior.

2.4.4 Dispersion Relation

SPPs are longitudinal surface waves that propagate along the interface between a dielectric and a metal. In the absence of magnetizable materials and external current densities, equations (2.1) can be expressed as follows [34]:

$$\nabla \times \mathbf{E} = -\mu_0 \frac{\partial \mathbf{H}}{\partial t} \tag{2.31}$$

$$\nabla \times \mathbf{H} = \frac{\partial \mathbf{D}}{\partial t} \tag{2.32}$$

By applying the curl operator to both sides of the first expression and utilizing the second expression, the following is obtained:

$$\nabla \times (\nabla \times \mathbf{E}) = -\mu_0 \frac{\partial^2 \mathbf{D}}{\partial t^2} \tag{2.33}$$

The expression can be rewritten by using the following mathematical identity:

$$\nabla \times (\nabla \times \mathbf{F}) = \nabla(\nabla \cdot \mathbf{F}) - \nabla^2 \mathbf{F} \tag{2.34}$$

and considering the absence of charge accumulation (i.e., $\nabla \cdot \mathbf{D} = 0$):

$$-\nabla^2 \mathbf{E} = -\mu_0 \frac{\partial^2 \mathbf{D}}{\partial t^2} \tag{2.35}$$

When using $c_0 = \frac{1}{\sqrt{\epsilon_0 \mu_0}}$, we obtain the wave equation for the electric field in linear isotropic media:

$$\nabla^2 \mathbf{E} - \frac{\epsilon}{c_0^2} \frac{\partial^2 \mathbf{E}}{\partial t^2} = 0 \tag{2.36}$$

When expressed in complex notation with $\frac{\partial}{\partial t} = i\omega$ and $\mathbf{E} = \mathbf{E}_0 e^{-i\omega t}$:

$$\nabla^2 \mathbf{E} + \epsilon k_0^2 \mathbf{E} = 0 \tag{2.37}$$

2.5 Plasmonic Metals

2.5.1 Silver

Silver is the simplest plasmonic metal to understand, as it is very well modelled by the Drude model (equation 2.17). Its SPP dispersion relation closely resembles the idealised case . Silver has the highest conductivity of any metal, and no strong inter-band transitions in the visible spectrum. Correspondingly, it also has the least damping for plasmonic applications. However, silver's downside is in its tendency to oxidise, which causes a gradual decay in resonance quality and limits its use for applications in ambient conditions. Recent work in our group however, demonstrated that graphene (see section 1.9) transferred on top of a silver layer can protect the surface from oxidation and preserve its properties for plasmonic applications[37].

2.5.2 Gold

Gold's high conductivity and exceptional inertness are its most advantageous properties. For some applications it is also favoured for its surface chemistry and bio compatibility[33]. However as might be deduced from its colour, gold has an inter band transition in the visible part of the spectrum, at around 470 nm, and several more in the ultraviolet, such as at 325 nm[8]. These result in increased damping near these wavelengths when compared to silver, increasing the imaginary component of the dielectric function. Accurately modelling the dielectric function of gold near these transitions requires modification . The presence of these interband transitions is the reason that gold is usually used for plasmonic resonances of wavelength > 600 nm. In this region damping is smaller and gold much more closely resembles an ideal Drude metal[38].

2.5.3 Copper

Copper has similar plasmonic properties to gold, and similarly its colour is an indication that it also has inter-band transitions towards the blue end of the visible spectrum. Copper is more conductive than gold, cheaper than gold and silver, and (unlike gold) is CMOS compatible. However, oxidation is again a major issue, with copper surfaces losing their plasmonic characteristics rapidly upon contact with air. As with silver, copper too can be protected from oxidation with a graphene layer to preserve its plasmonic properties. Graphene protected copper even showed a slight improvement in SPP resonance quality factor[39].

2.5.4 Other plasmonic metals

Many other metals support surface plasmon resonances. Aluminium has an interband transition at 800 nm, which severely limits its application in the visible. However its damping is much lower in the blue and UV part of the spectrum[10]. Like copper, it suffers from rapid oxidation, which limits usefulness for plasmonic applications. Other metals with plasmon resonances include alkali metals such as lithium, sodium and potassium (which are obviously severely limited by their reactivity), as well as nickel, indium, platinum, palladium and rhodium[40]. These metals generally suffer from high losses (except potentially the highly reactive alkali metals), and so are only used in situations where they exhibit some other useful property such as catalysis[10]. Alloys present another interesting possibility which has only recently begun to be investigated for plasmonic applications[37], [41], [42]

2.5.5 Dielectric function of metals

The gas motion has been explained successfully by Newton's second law. Therefore, an electron gas displacement can be described by the following formula:

F = m $d^2\mathbf{r}/dt^2$, $\mathbf{F}=e\mathbf{E}$ (2.19) By combining the equation 1.1 and 1.7 we obtain for the oscillating electric field the following:

$$\mathbf{P}(\mathbf{r},\omega) = -\frac{ne^2}{m\omega^2}\cdot\mathbf{E}(\mathbf{r},\omega), \quad \mathbf{E} = \mathbf{E}_0(\mathbf{r})e^{i\omega t}$$

The displacement field formula (equation 1.3) takes following form:

$$\omega_p^2 = \frac{ne^2}{m\epsilon_0}, \quad \epsilon_r = 1 - \frac{\omega_p^2}{\omega^2}$$

The term in brackets is the frequency dependent dielectric permittivity (ϵ_r). It depends on the mass of electrons and the number of free electrons. We define the plasma frequency ω_p and it has following form:

$$\epsilon_r = 1 - \frac{\omega_p^2}{\omega^2 + i\gamma\omega}, \quad \gamma = \frac{1}{\tau}$$

So far, we have considered that the electrons are simply displaced in the metal by the external electric field force. However, in Drude model of free electrons the collisions exist and that will damp the oscillations with a rate of $1/\tau$. After some calculus taking into account the collisions (damping factor) the er becomes:

$$\sqrt{\epsilon_r} = \tilde{n} = n + ik$$
$$\epsilon' = n^2 - k^2$$
$$\epsilon'' = 2nk$$

where, k is the extinction coefficient and n is the refractive index. When $\omega \leq \omega_p$ the metal has reflectivity of 1, but in the case of $\omega \geq \omega_p$ the metal acts as a dielectric with positive dielectric permittivity. We derive a wave equation (1.13) using the solution of Maxwell's equations and linear algebra, when there is not external charge or current density

$$\mathbf{k}(\mathbf{k}\cdot\mathbf{E}) - \mathbf{k}^2\mathbf{E} = \frac{\epsilon_r\omega^2}{c^2}\mathbf{E}$$

where k is the wave vector, c is the light speed in free space. Let's go to the case, when $\omega = \omega_p$, then $\epsilon(\omega_p)$ tends to zero! So, the right side of the equation becomes zero, and the only solution occurs when the first term and the second term are equal. It is possible if the wave is not transverse, hence the electric field and wave vector are collinear. One may conclude plasmon waves are longitudinal. These plasmons calls bulk or volume plasmons. There are two families of plasmons -

- Bulk (or volume) plasmons and
- Surface Plasmons.

The plasma frequency is linked to bulk plasmons.

2.5.6 Plasma frequency for Ag and Au

This description, although over-simplified, is nevertheless successful in explaining semi-quantitatively the optical response of many real metals. For example, at wavelengths longer than all inter-band transitions, The ω-dependence should then be described by the Drude term (and vary as ω^{-2}). This has been verified experimentally [43] for Ag and Au, from which the same value of $\sqrt{\epsilon_\infty}\omega_p \approx 1.4 \times 10^{16}$ rad s^{-1} is derived. This is in remarkable agreement with the expression for ω_p in Eq. (3.3) derived from the Drude model. Taking an effective mass equal to the electron mass and a density of conduction electrons of the order of $n \approx 6 \times 10^{28}$ m^{-3} (corresponding to a full d band with one free s electron per atom) give precisely This description, although over-simplified, is nevertheless successful in explaining semi-quantitatively the optical response of many real metals. For example, at wavelengths longer than all inter-band transitions, The ω-dependence should then be described by the Drude term (and vary as ω^{-2}). This has been verified experimentally [35] for Ag and Au, from which the same value of $\sqrt{\epsilon_\infty}\omega_p \approx 1.4 \times 10^{16}$ rad s^{-1} is derived. This is in remarkable agreement with the expression for ω_p in derived from the Drude model. Taking an effective mass equal to the electron mass and a density of conduction electrons of the order of $n \approx 6 \times 10^{28}$ m^{-3} (corresponding to a full d band with one free s electron per atom) give precisely

$$\sqrt{\epsilon_\infty}\omega_p \approx 1.4 \times 10^{16} \text{ rad s}^{-1},$$

or $\hbar\omega_p \approx 9.1/\sqrt{\epsilon_\infty}$ eV, or a corresponding wavelength of $\lambda_p \approx 136/\sqrt{\epsilon_\infty}$ nm. The Drude model therefore gives an excellent description of the long-wavelength optical response of Ag and Au. Only the value of ϵ_∞ is missing. This is understandable though, for ϵ_∞ comes from high energy contributions in the deep UV-range, which are not included in this simple treatment of the problem.The frequency-dependent dielectric functions of Ag and Au are of crucial importance for many plasmonics problems.

2.6 Surface Plasmons and Plasmonic Excitations

The wave vector can be real or imaginary depending on the frequency of EM wave (equation 1.14). We have discussed the properties of metals when they are reflective or transparent relied on the illumination frequency. Let's discuss another family of plasmons: surface plasmons. Indeed, the wave vector is complex at the surface with real part that corresponds to the propagation and the imaginary part to the attenuation. The wave at the surface is evanescent, hence do not radiate as electric field and magnetic field are not transverse to each other. We know that for evanescent waves the vertical component of wave vector (k_z) is imaginary and parallel component is real (k_x). Using the boundary conditions for two interfaces (the scheme is shown in Fig. 1.3a) the general dispersion relation of surface wave is derived as:

$$k_x^2 = \frac{\epsilon_1\epsilon_2}{\epsilon_1 + \epsilon_2} \cdot \frac{\omega^2}{c^2} \tag{2.20}$$

where, ϵ_1 is the dielectric permittivity of the light injection medium. We can transform this relation for metal interface by following:

$$k_x^2 = \frac{\epsilon_r}{1 + \epsilon_r} \cdot \frac{\omega^2}{c^2} \tag{2.42}$$

One may find the dispersion curve of surface plasmon polariton (SPP) below (Fig. 2.3b). When $k_x \to 0$, then $\omega \to 0$ and when $k_x \to$ inf then $\omega \to \frac{\omega_p}{\sqrt{2}}$. One may conclude that SPP can exist when $\omega \leq \omega_p/\sqrt{2}$. Here we show how in-plane momentum (k_x) varies with frequency. What about the out-of-plane momentum (k_z)? We already have mentioned that k_z is imaginary for surface evanescent waves. Unlike Fresnel' evanescent wave the field is decaying exponentially on both sides for surface plasmon wave. Note, the charge fluctuations

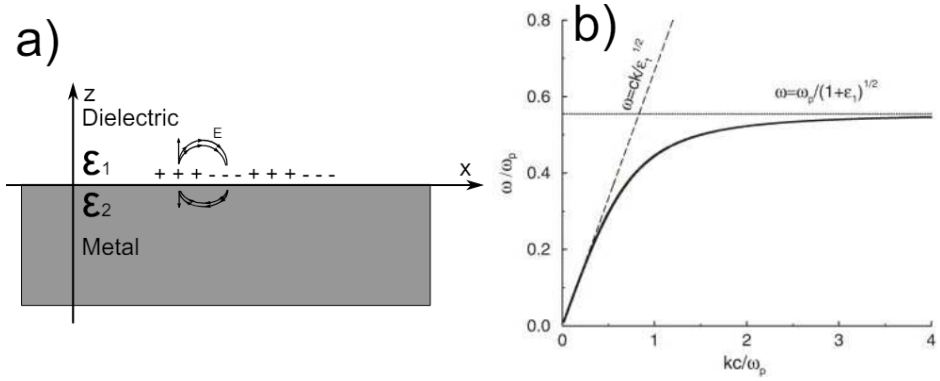

FIGURE 2.3: (a) Schematic of the distribution of the electromagnetic field of SPP at the metal-dielectric interface. (b) Dispersion curve for SPP at interface of Drude metal, when the collisions are negligible (black solid curved). the dash lines show the dispersion of light in the dielectric with dielectric permittivity of e1. (extracted from Ref. [43])

are localized in the z direction within the Thomas-Fermi screening length which is one angstrom. These charge fluctuations associated to the mixed transversal and longitudinal EM field, which dispersers along the surface and the maximum of EM field is at the surface (z=0) position [44], [45]. We deduce that the EM field is very sensitive to the surface properties.

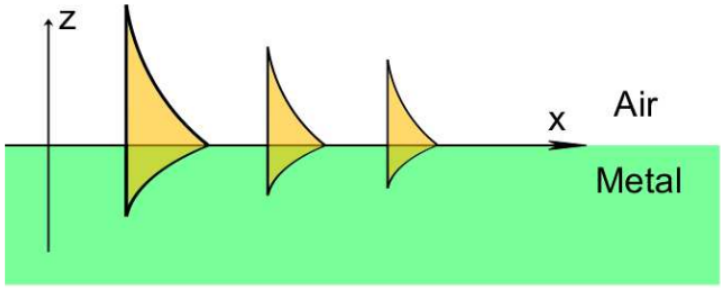

FIGURE 2.4: Schematic of SPP propagation at the metal surface in time. It shows the dissipation of the SPP by traveling some distance.)

For metals, the dielectric permittivity is a complex quantity, which implies that the k_x is complex (equation 1.16). Hence, in-plane complex wave vector can be presented as:

$$k_x = k'_x + ik''_x, \quad k'_x = \frac{\omega}{c} \cdot \sqrt{\frac{\epsilon'}{1+\epsilon'}}$$

$$k''_x = \frac{\omega}{c} \left(\frac{\epsilon'}{1+\epsilon'}\right)^{3/2} \cdot \frac{\epsilon''}{2(\epsilon')^2}$$

The intensity of plasmon wave traveling along the interface (x-axis) is exponentially decaying by $exp^{-2k''_{00}x_0}$ The schematic is shown in Fig. 1.4. We define the propagation length of the surface plasmon polariton as:

$$L_{\mathrm{SPP}} = \frac{1}{2k''_x}$$

Plasmonic Excitations

The most basic systems that can sustain both SPs and SPPs are those that can be considered as a semi-infinite flat isotropic single interface. Modern experiments and applications have now moved beyond investigation of this simple system, however this fundamental example still provides excellent insight into what these phenomena actually are, their properties, and requirements for excitation. A theoretical treatment for a simple SP and SPP system will be described first, followed by brief overviews of LSPP excitations on NPs and coupled LSPP interactions between NP pairs.

2.6.1 Surface Plasmon Polarition

The surface Plasmon polariton(SPP) is formed by the surface Plasmon coupling with photons at the metals/dielectric interface. We can consider a situation which polarized wave reaching a planar interface between metal and dielectric at an incident angle θ_1 (Fig2.5). The polarized incident on the interface, the surface charges undergo a collective oscillation because of the oscillating electric field at the interface. If the frequency and the momentum of SPPs can match that of the photon, the resonance will occur. The radiative surface plasmons are coupled with the propagating electromagnetic wave. Even the wave is totally reflected by the interface, it decays in a direction normal to the interface. (Fig2.2). However, the non-radiative surface plasmons act oppositely. It does not couple with propagating electromagnetic wave. Therefore the perfect SPP should be irradiative. It is a difference from volume Plasmon, which is related to the intrinsic property of those materials, surface plasmon excitation can be understood in artificial plasmonic crystals. Most of the plasmonic crystals can be periodic nanostructure

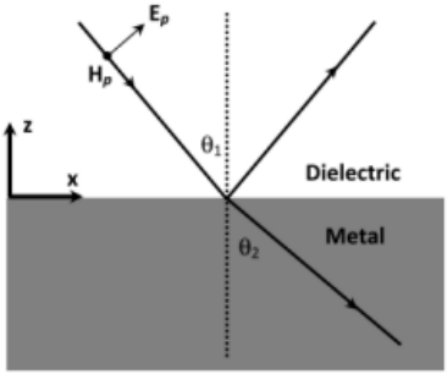

FIGURE 2.5: the Diagram of the polarized electromagnetic incident upon an interface between metal and dielectric.)

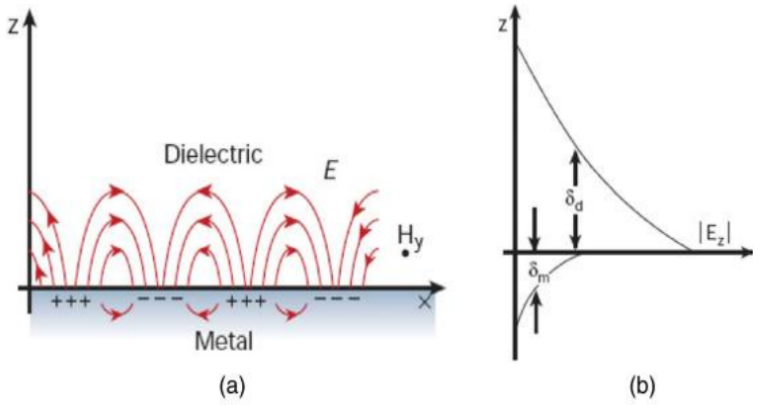

FIGURE 2.6: (a) the Diagram of surface charges and electromagnetic wave at the interface between two media, (b) the changing of locally electric field component with distance to the interface.)

From Maxwell's equation, the properties of SPPs can be derived as the following equations (Equ 2.2-2.4). When the wave propagates in the interface (Z = 0 plane; metal is Z < 0; dielectric is Z > 0), the electric and magnetic fields can express as a function of (t)time and (x, y, z) position[19].

$$E_{x,n}(x,y,z,t) = E_0 e^{ik_x x + ik_{z,n}|z| - i\omega t} \tag{2.21}$$

$$E_{z,n}(x,y,z,t) = \pm E_0 \frac{k_x}{k_{z,n}} e^{ik_x x + ik_{z,n}|z| - i\omega t} \tag{2.45}$$

$$H_{y,n}(x,y,z,t) = H_0 \frac{k_x}{k_{z,n}} e^{ik_x x + ik_{z,n}|z| - i\omega t} \tag{2.46}$$

Which n represents the material when 1 is the metal at z < 0, 2 is the dielectric at z > 0, k is the wave vector and ω is the angular frequency of the waves. After the incident light converts into SPPs on the surface of the metal, it starts to propagate until the metal absorpt all the energy. Therefore the imaginary part of the complex SPP wavevector k_spp limite the propagation length of the SPPs (δ_{spp}) which is the distance after the intensity of SPPs drops to $1/e$ of the starting value[19]

$$k_{spp} = k_{sppr} + ik_{sppi} \tag{2.47}$$

$$\epsilon_m = \epsilon_{mr} + i\epsilon_{mi} \tag{2.48}$$

From the SPPs dispersion relation,

$$k_{spp} = k\sqrt{\frac{\epsilon_d \epsilon_m}{\epsilon_d + \epsilon_m}} \tag{2.49}$$

With equation (2.6),

$$\delta_{spp} = \frac{1}{2k_{sppi}} = \frac{\lambda}{2\pi}\left(\frac{\epsilon_{mr} + \epsilon_d}{\epsilon_{mr}\epsilon_d}\right)^{3/2} \frac{\epsilon_{mr}^2}{\epsilon_{mi}} \tag{2.50}$$

Where ϵ_{mi} and ϵ_{mr} are the imaginary and real parts of the dielectric function of the metal respectively. Consequently, the propagation length of SPPs (δ_{spp}) depends on the dielectric constant of the metal usually, also the incident wavelength.

2.6.2 Localized Surface Plasmon polarition

The planar approximation is no longer true for small metallic objects, and in particular for nano-particles, where the size becomes comparable or smaller than the wavelength. The nature of the electromagnetic modes of the system is then completely modified. In particular, the description in terms of k vector (k_x for a plane) becomes irrelevant, since the translational invariance is lost. The electromagnetic modes then exist for discrete values of ω (instead of having continuous modes described by the dispersion relation $\omega(k_x)$). These modes are then called localized surface plasmon–polaritons (LSPs)[46]. In fact, this is not a property of metals or plasmon–polaritons only. The same happens for photons when the environment exhibits features of the order of the wavelength. Photons correspond to free-space modes of the electromagnetic field (plane waves with well defined ω and k). When boundaries have features much larger than the wavelength, one can apply the 'standard' description giving rise to reflection and refraction at interfaces (Snell's law). All boundaries are approximated by locally planar interfaces, and this 'ray optics' approach is perfectly legitimate. However, when the dimensions of the system become comparable to the wavelength, say in a cavity or a wave-guide, this approach fails. The concept of photon is replaced by that of electromagnetic modes of the cavity (characterized by discrete values of ω, or $\omega(k)$ where k is irrelevant). These modes are highly localized inside the cavity. They are sometimes called cavity polaritons to emphasize their mixed nature of a photon with its optical environment, and are the photon analogs of localized SPPs.

2.7 Surface Plasmon Resonance

Surface Plasmon Resonance (SPR) is a phenomenon when incident light reaches the interface of metal and dielectric where there is different refractive index [20]. SPR is generated i.e. excited collective oscillations of free electrons in conduction band of metal which also known as surface plasmons. At the excitation, SPR creates a dip in reflectance at the specific wavelength which reflects the absorption of optical energy in the metal. Incident light beam or electron bombardment can be used to excite surface plasmons resonance, visible light and infrared light are the typical sources. The incident light has to match the momentum and frequency of that plasmon. For S polarized incident light which polarization is perpendicular to the plane of the light cannot create surface plasmons. Only p polarized light which polarization is parallel to the plane of light can create the SPR at a specific wavelength. There are two main types of SPR which are propagating and localized respectively [21]. Propagating SPR occurs when plasmons propagate along the interface between dielectric and metal film, therefore it is mainly in distance of the order of microns. On the other hands, localized SPR focusing on the incident light interacts with nano metal much smaller than the incident wavelength resulting in distance of the order of nanometer.

2.8 Localized Surface Plasmon Resonance

When metal nanoparticles sizes is smaller than the incident light wavelength, strong dipolar excitations are formed and defined as localized surface plasmon resonance (LSPR). LSPR is a non-propagating excitation of the electrons in conduction band of nanoparticles coupling with the incident electromagnetic field [21]. The resonance frequency of the oscillation related to the surface plasmon energy is determined by several factors, for example the particles size, the distance between particles, and the dielectric properties of metal and

surrounding medium. A large resonant enhancement of the local electromagnetic field inside and near the nanoparticles is caused by the 9 collective charge oscillation. This field enhancement can be used in different potential applications in optical devices.

The LSP modes of a nano-particle can be excited by an incident wave with the appropriate polarization and frequency. Efficient coupling to LSP modes will then result in a resonant optical response at the LSP frequency. As opposed to PSPP on planar interfaces, LSPs are radiative modes (with an absorptive component because of optical absorption in the metal). The resonant response therefore, not only appears in absorption (which is analogous to the reflectivity experiments for a plane interface), but also in scattering (or similarly extinction) measurements. These resonances, sometimes called LSP resonances (LSPR) to differentiate them from SPR (based on PSPPs), are sensitive to the environment and, like SPR, can be used for applications in refractive-index and chemical sensing. The LSP resonances also manifest themselves, as for PSPP modes, as large local field enhancements inside the metal, and more importantly on the surface outside. This effect is the basis for most surface-enhanced spectroscopies, including SERS. It is interesting to highlight the main **differences between SPR and LSPR**:

- The SPR condition requires conservation of both k_x and ω. This is more difficult to fulfill than only ω conservation for LSPR. In particular, k_x conservation typically requires a more complex setup, such as the ATR configuration.
- SPRs offer more liberty in the implementation, either in terms of angle-modulation or wavelength-modulation, whereas only wavelength modulation can be used for LSPRs.
- SPRs are typically much sharper resonances compared to LSPRs. This can be an advantage or a disadvantage depending on the application. It should for example in principle result in a larger sensitivity but only on a more limited range of parameters. For SERS, resonances must be broad enough to encompass both the exciting laser and the Stokes frequencies, and SPRs are typically too sharp to fulfill that condition.
- The active surface for SPRs is a single planar interface, while for LSPRs it is the nanoparticle surface (which can therefore be spread in a 3D volume, for example by dispersing the particles in water).
- There are more degrees of freedom to tailor or engineer the LSPRs (shape, size, etc.) as opposed to the SPRs, which may open more possibilities, but also more problems (such as poly-dispersity).

In summary, the use of SPR vs LSPR will depend on the exact application. LSPRs are more versatile (easier to implement) but the resonances are not as well defined as for SPRs.

2.8.1 Mie solutions

In this work the tip apex NPs are of too large diameter ($a \approx 150$ nm $\sim \lambda/5$) to be accurately modelled using the quasi-static approximation and hence the exact Mie solutions are more appropriate to yield further insight into LSPPs supported on such NPs. The Mie solutions are obtained by first re-expressing Maxwell's wave equation in polar coordinates via use of Debye potentials. By considering a single uniform incident infinite plane-wave, boundary conditions are imposed to ensure continuity of the fields at $r = a$ and hence solutions for the Debye potentials are found in terms of spherical harmonics [34]. The electric and magnetic

field solutions are therefore reconstructed in terms of vector spherical harmonics. The far-field response is described by the scattering coefficients $\tilde{a}_\ell$ and $\tilde{b}_\ell$ that are given by

$$\tilde{a}_\ell = \frac{\eta^2\psi_\ell(\eta\alpha)\psi_\ell(\alpha) - \psi_\ell(\alpha)\psi'_\ell(\eta\alpha)}{\eta^2\psi_\ell(\eta\alpha)\xi^2_\ell(\alpha) - \xi_\ell(\alpha)\psi'_\ell(\eta\alpha)} \tag{2.57}$$

where $\eta = (\tilde{n}_m/n_d)$, the size parameter $\alpha = 2\pi a n_d/\lambda_0$ and the Riccati-Bessel functions $\psi_\ell(z) = zj_\ell(z)$ and $\xi_\ell(z) = zh^{(1)}_\ell(z)$ with j_ℓ and $h^{(1)}_\ell$ denoting spherical Bessel and Hankel functions respectively. Here the prime $'$ denotes the derivative of the function with respect to the argument. There is no m dependence in Eqns. (2.57) as for uniform infinite single plane-wave excitation the boundary conditions at $r = a$ require $m = 1$ for all ℓ. By considering the Poynting vector of the total electromagnetic field surrounding the NP the far-field scattering and extinction cross-sections are given by [47]

$$C_{\text{sca}} = \frac{2\pi}{k^2}\sum_{\ell=1}^{\infty}(2\ell+1)\left(|\tilde{a}_\ell|^2 + |\tilde{b}_\ell|^2\right) \tag{2.58}$$

$$C_{\text{ext}} = \frac{2\pi}{k^2}\sum_{\ell=1}^{\infty}(2\ell+1)\Re\left[\tilde{a}_\ell + \tilde{b}_\ell\right] \tag{2.59}$$

where $k = 2\pi n_d/\lambda_0$ is the wavenumber of the incident light in the surrounding dielectric medium. The absorption cross-section C_{abs} can be obtained via Eqn. (2.41). The Mie solutions show significant modifications to the quasi-static results are required for NPs with $a \gtrsim 20$ nm. The three most prevalent corrections are

- For noble metals, an additional overall red-shift of the dipole and higher-order modes with increasing NP diameter due to retardation of the exciting and depolarisation fields.
- Retardation creates a non-uniform field over the volume of a NP and hence higher-order (e.g. quadrupole) LSPP modes can be excited by the incident light even for spherically symmetric NPs. This effect becomes significant when $a \gtrsim 100$ nm.
- A new decay channel: radiation damping due to direct radiative decay of LSPPs into photons. For increasing NP diameter the radiative damping becomes significant and the decrease in absorption and hence the LSPP resonances are broadened.

Radiation damping increases the homogeneous LSPP mode energy linewidth $\Gamma^\ell_{\text{LSPP}}$ (as shown in Fig. (2.7)) and thus reduces the LSPP mode lifetime (dephasing time) τ^ℓ_{LSPP} according to

$$\tau^\ell_{\text{LSPP}} = \frac{2\hbar}{\Gamma^\ell_{\text{LSPP}}} \tag{2.60}$$

The strength of the LSPP mode can hence be expressed in terms of a mode quality factor Q^ℓ_{LSPP} via $Q^\ell_{\text{LSPP}} = E^\ell_{\text{LSPP}}/\Gamma^\ell_{\text{LSPP}}$, where E^ℓ_{LSPP} is the resonant energy associated with the LSPP mode. The Mie solutions thus give the dependence of τ^ℓ_{LSPP} on particle diameter and dielectric surroundings and yields values between 2 – 10 fs for NPs between 150 – 20 nm diameter[15] in air, for $\ell = 1$. For NPs of $\lesssim 10$ nm diameter spatially non-local effects, primarily non-local screening due to finite penetration of induced-surface-charge into the NP interior, act to broaden the LSPP modes significantly. Therefore the LSPP mode lifetimes are substantially reduced compared to those calculated assuming spatially local response only.

Finally, it is important to note that both the traditional quasi-static and Mie solutions assume a single infinite incident plane-wave. In experiment this condition is never met. For example, under the DF illumination conditions used in this work, both the incident and

scattered light are defined over certain angular ranges given by the Numerical Aperture (NA) of the various optical components. This can modify the measured optical response considerably [40] and hence must be acknowledged when comparisons are made between experiment and theory. It has also been reported that the measured optical response can be significantly altered when LSPPs are excited with non-homogeneous illumination, e.g. a focussed Gaussian beam [34].

Chapter 3

Plasmonic coupling of photothermal response

Here we introduce the **second fundamental excitation of plasmonics** [48]- localized surface plasmons. We have already seen in the preceding chapters that SPPs are propagating, dispersive electromagnetic waves coupled to the electron plasma of a conductor at a dielectric interface. Localized surface plasmons on the other hand are non-propagating excitations of the conduction electrons of metallic nanostructures coupled to the electromagnetic field. We will see that these modes arise naturally from the scattering problem of a small, subwavelength conductive nanoparticle in an oscillating electromagnetic field.

The curved surface of the particle exerts an effective restoring force on the driven electrons, so that a resonance can arise, leading to field amplification both inside and in the near-field zone outside the particle. This resonance is called the localized surface plasmon or short localized plasmon resonance. We explore the physics of localized surface plasmons by first considering the interaction of metal nanoparticles with an electromagnetic wave in order to arrive at the resonance condition. Subsequent sections discuss damping processes, studies of plasmon resonances in particles of a variety of different shapes and sizes, and the effects of interactions between particles in ensembles. Other important nanostructures apart from solid particles that support localized plasmons are dielectric inclusions in metal bodies or surfaces, and nanoshells. The chapter closes with a brief look at the interaction of metal particles with gain media.[43], [49]

For gold and silver nanoparticles, the resonance falls into the visible region of the electromagnetic spectrum. A striking consequence of this are the bright colors exhibited by particles both in transmitted and reflected light, due to resonantly enhanced absorption and scattering. This effect has found applications for many hundreds of years, for example in the staining of glass for windows or ornamental cups.

3.1 Nano-Metals Plasmonic Coupling Effect

Surface plasmons mainly occur at the surface of metals where the collective free electron density oscillation in response to an external electric field.[50], [51] (Fig. 3.1) When the interparticle distance is much larger than the particles size, the surface Plasmon resonance is affected by the geometry of the nanoparticle, also the dimension of it. However, the 7 surface plasmons can interact with the adjacent nanoparticles; their close proximity would give rise to Plasmon coupling appear.

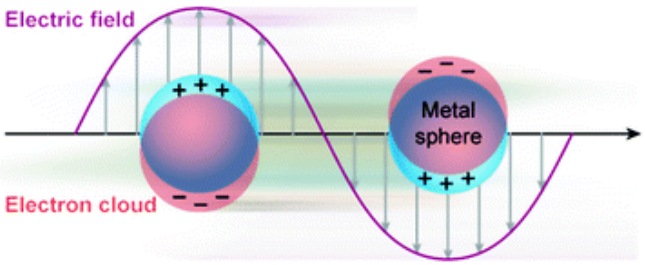

FIGURE 3.1: e Diagram of Electric Field on Electron Delocalization

Figure 3.1 the Diagram of Electric Field on Electron Delocalization The main consequence of plasmonic coupling between nanoparticles is the changing of metals optical properties [52]. The optical properties of the coupled particles can be much different from that of an individual particle in bulk state because of the close interaction of coherent oscillation of electrons. The effect of plasmon coupling can vary enormously (Fig 3.2). there are many inter-play factors in plasmon coupling, such as interparticle spacing, nanoparticle shape and size, number of plasmon-coupled nanoparticles, light polarization etc.[53]. Taking the plasmon coupling of gold nanospheres as the example, there is the noteworthy shift of the overall extinction peak, which is dominated by absorption, from lower absorbance spectrum in green to the higher wavelengths on red as the interparticle spacing is decreased.

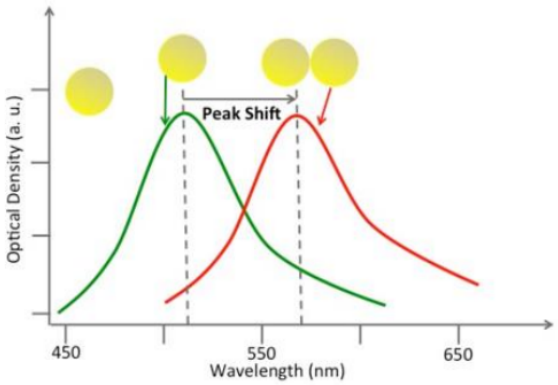

FIGURE 3.2: The changing of the absorbance spectrum of single gold nanosphere.

3.2 Metals Plasmonic Coupling

When more details of plasmon coupling are investigated, more properties of plasmonic effect are discovered. Plasmon coupling can further enhance the properties of individual metal nanoparticles creating new resonances in close proximity. (Fig 3.5) Because of the localized electric fields are enhanced between the nanoparticles, the optical resonance wavelengths become adjustable under strong electromagnetic fields [54].

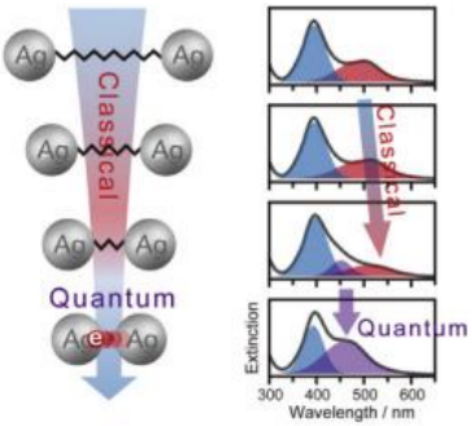

FIGURE 3.3: The relation between silver nanoparticles in nanometer distance and the change of the optical resonance wavelengths [55]

The simple structure we considered, such as sphere, ellipsoid, can reduce the number of variables controlling the plasmonic effect so that the plasmonic coupling can only be governed by the change in the distance between nanoparticles. From classical electromagnetic model, the shorter interparticle distance creates the stronger plasmon coupling shifting which moves to longer wavelengths. However, this classical model no longer valid when the gap distance is less than 1 nm, then Quantum effects including electron tunnelling, nonlocality of dielectric function play the main role in this regime [56]. The quantum effect is not within this investigation.

3.2.1 Plasmonic property of Ag

In recent survey, gold and silver are the two most often used metals for plasmonic devices because of their low energy loss in the visible and near infrared ranges compared to other metallic resources. For example, silver has been used for the fabrication of hyperlens [52], superlens [52], and has a negative refractive index material in the visible range [52]. Although the alkali metals, such as potassium and sodium have lower energy loss than silver and gold, those metals are too reactive in air and with water, limiting their use. Since the electric field distribution in a material depends on the real part of permittivity, and the energy loss depends on the imaginary part. In fact, the real part of the silver permittivity is negative with wavelengths less than or equals to 326 nm. It makes silver becomes an attractive plasmonic material (Fig 3.5)

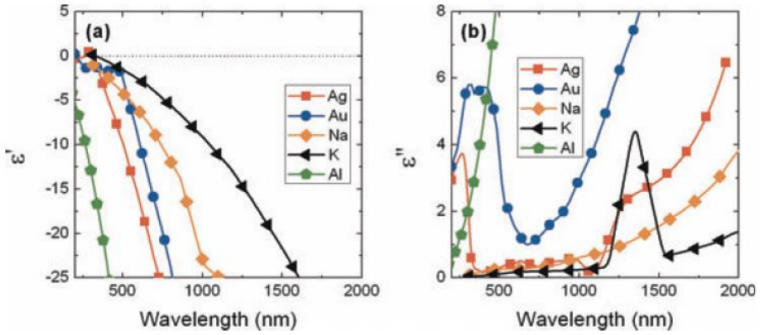

FIGURE 3.4: The (a) real part and (b) imaginary part of the permittivity of Ag, Au, Na, K and Al [57]

Consider the quality factors of localized surface plasmon resonance (LSPR) and surface plasmon polaritons (SPP) systems, the LSPR and SPP system are denoted as Q_{LSPR} and Q_{SPP} respectively. SPP and LSPR systems can enhance the local field performance at the surface of the metal films, therefore the definition of their quality factors is defined as below:

$$Q_t = \frac{\text{Enhanced local electric field}}{\text{Incident field}} \tag{3.1}$$

Quality factor for LSPR is affected by the shape of the nanoparticles as well. For a spherical particle, Q_{LSPR} can be defined as follows: **reference25**

$$Q_{LSPR}(\omega) = \frac{-\epsilon'(\omega)}{\epsilon''} \tag{3.2}$$

Quality factor for SPP assumes the same form as the above equation. Q_{SPP} can be simplified as the ratio of the real part of the propagation wave vector (k'_x) to the imaginary part of the wave vector (k''_x) [43]:

$$Q'_{SPP}(\omega) = \frac{k'_x(\omega)}{k''_x(\omega)} = \frac{\epsilon'_m(\omega) + \epsilon_d(\omega)}{\epsilon''_m(\omega)} \frac{\epsilon'_m(\omega)^2}{\epsilon''_m(\omega)\epsilon_d(\omega)} \tag{3.3}$$

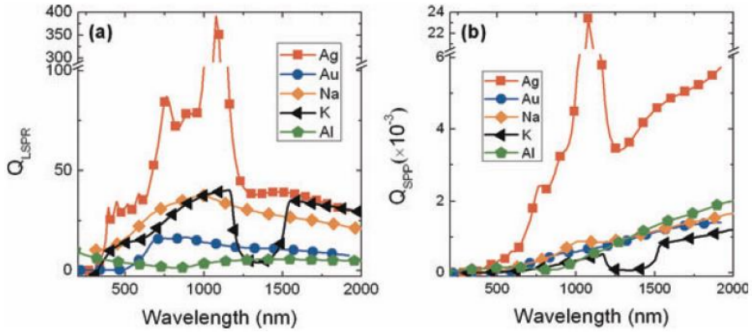

FIGURE 3.5: T(a) Quality factor of LSPR and (b) Quality factor of SPP of Ag, Au, Na, K and Al [58]

3.3 Localized surface plasmon resonances in metal nanoparticles

Metal nanoparticles display strong and unique optical resonances in the visible and near-infrared (NIR) region of the electromagnetic spectrum due to the resonant response of their free electrons to the electric field of light [59]–[57]. This free electron response is described by the dielectric function of the metal as per the Drude model [34]:

$$\epsilon_{Drude} = 1 - \frac{\omega_p^2}{\omega^2 + i\gamma\omega} \tag{3.1}$$

where ω is the angular frequency of the light, γ is the electron collision frequency in the bulk, and ω_p is the bulk plasma frequency of the free electrons, which is determined by the density of free electrons N in the metal and the effective mass m_e of the electrons as:

$$\omega_p = \sqrt{\frac{Ne^2}{\epsilon_0 m_e}} \tag{3.4}$$

In the case of real metals, bound electrons contribute to the dielectric function, for instance due to inter-band transitions from the valence to conduction band, especially in the

high frequency.region of the spectrum. A high-frequency part ϵ_∞ [60], therefore, has to be added to the Drude contribution for accurately describing the response of the metal electrons to the electromagnetic field:

$$\epsilon = \epsilon_\infty - \frac{\omega_p^2}{\omega^2 + i\gamma\omega} \tag{3.5}$$

When the metallic nanoparticle is subject to light excitation, the electric field of the light induces waves of collective electron oscillations confined to the surface of the nanoparticle, a phenomenon known as a localized surface plasmon resonance [61]–[62]. This wave motion is composed of different orders, from the lowest dipolar to higher order multipoles [63], depending on the size of the nanoparticle relative to the wavelength of light. However, in the case of particles of size much smaller than the wavelength of light, (i.e., radius $r \ll \lambda$), the electron oscillation can be considered to be predominantly dipolar in nature. In this limit, the collective response of the electrons in a small metal nanoparticle to the electric field of the light (assumed to be uniform across the particle) is described by the dipolar polarizability α [64]:

$$\alpha = (1 + \kappa)\epsilon_0 V \left(\frac{\epsilon - \epsilon_m}{\epsilon + \kappa\epsilon_m} \right) \tag{3.6}$$

where V is the volume of the particle and ϵ_m is the medium dielectric constant. κ is a shape factor that incorporates the dependence of the polarizability on the geometry of the surface that defines the electron oscillations. While $\kappa = 2$ for a sphere, for more polarized shapes such as ellipsoids with a high surface curvature along a...

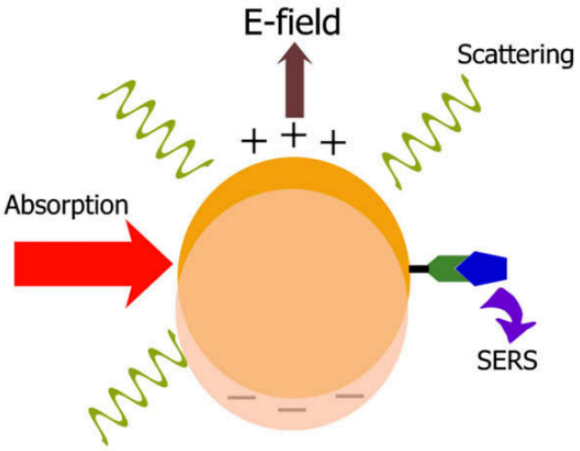

FIGURE 3.6: Scheme showing the coherent collective oscillation of electrons of a metallic nanoparticle constituting a localized surface plasmon resonance (LSPR) mode. The LSPR results in an enhancement in the optical properties of the nanostructure, i.e., the electric field intensity near the particle, light scattering, light absorption, and surface enhanced scattering from adsorbed molecules are all enhanced at the LSPR frequency.

given dimension (e.g., triangles, rod-shaped particles), the value of κ can be much higher along that dimension [65].

The polarizability α becomes maximum (representing a strong resonance between the free electrons and the light field) at the frequency at which:

$$\mathrm{Re}(\epsilon) = -\kappa\epsilon_m \tag{3.7}$$

Here Re denotes the real part. This frequency ω_{sp} corresponds to the localized surface plasmon resonance (LSPR) frequency of the particle. From Eqs. (3) and (5), we see that the LSPR frequency is determined by the bulk plasma frequency ω_p of the metal free electrons (however modulated by the presence of inter-band transitions) and further tuned by the geometry of the nanostructure (κ) and the medium surrounding the particle (ϵ_m).

$$\omega_{sp} = \sqrt{\frac{Ne^2}{m_e \epsilon_0 (\epsilon_\infty + \kappa \epsilon_m)}} \tag{3.8}$$

While the real part of the metal dielectric function $\mathrm{Re}(\epsilon)$ governs the frequency position of the electron oscillation resonance, the imaginary part $\mathrm{Im}(\epsilon)$ incorporates the broadening and absorptive dissipation of the resonance due to damping and dephasing of the electron oscillations.

3.4 Plasmon resonances in assemblies of metal nanoparticles

When two metal nanoparticles are brought in proximity to each other, the near-field on one nanoparticle can interact with that on the other particle [48], [57], [64], [66]. Thus, the electric field E felt by each particle is the sum of the incident light field E_0 and the near-field E_{nf} of the neighboring particle.

$$E = E_0 + E_{\mathrm{nf}} \tag{3.9}$$

As a result of this near-field interaction, plasmon oscillations of the two nanoparticles become coupled. This plasmon coupling modulates the LSPR frequency of the coupled-nanoparticle system. For instance, in spherical gold nanoparticles, assembly or aggregation into a close-packed structure results in a strong red-shift of the LSPR wavelength from the LSPR maximum of ~ 520 nm of an isolated colloidal nanoparticle **reference35**, **reference36**. In a larger assembly (by particle number), each particle would be subject to the near-field of a large number of particles, resulting in a much stronger coupling and hence a larger red-shift. In addition, the distance between the nanoparticles in the assembly also determines the amount of plasmon red-shift, due to the rapid decay of a nanoparticle's near-field with distance. The closer the particles in the assembly, the larger is the red-shift of the plasmon resonance [44], [45], [67]. The distance-dependence of plasmon coupling is described in significant detail later in this Letter.

3.5 Normal Modes of Sub-Wavelength Metal Particles

The interaction of a particle of size d with the electromagnetic field can be analyzed using the simple quasi-static approximation provided that $d \ll \lambda$, i.e. the particle is much smaller than the wavelength of light in the surrounding medium. In this case, the phase of the harmonically oscillating electromagnetic field is practically constant over the particle volume, so that one can calculate the spatial field distribution by assuming the simplified problem of a particle in an electrostatic field. The harmonic time dependence can then be added to the solution once the field distributions are known. As we will show below, this lowest-order approximation of the full scattering problem describes the optical properties of nanoparticles of dimensions below 100 nm adequately for many purposes.

We start with the most convenient geometry for an analytical treatment: a homogeneous, isotropic sphere of radius a located at the origin in a uniform, static electric field $E = E_0 \hat{z}$ (Fig. 3.8). The surrounding medium is isotropic and non-absorbing with dielectric constant ϵ_m, and the field lines are parallel to the z-direction at sufficient distance from the sphere.

The dielectric response of the sphere is further described by the dielectric function $\epsilon(\omega)$, which we take for the moment as a simple complex number ϵ.

In the electrostatic approach, we are interested in a solution of the Laplace equation for the potential, $\nabla^2\Phi = 0$, from which we will be able to calculate the electric field $E = -\nabla\Phi$. Due to the azimuthal symmetry of the problem, the general solution is of the form [68]

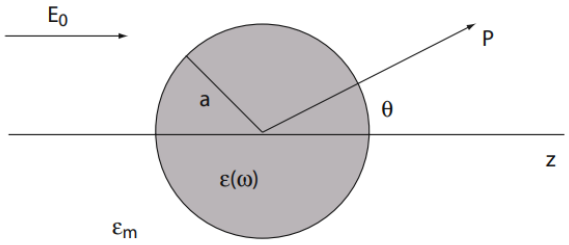

FIGURE 3.7: Sketch of a homogeneous sphere placed into an electrostatic field.

$$\Phi(r,\theta) = \sum_{l=0}^{\infty} \left(A_l r^l + B_l r^{-(l+1)} \right) P_l(\cos\theta), \tag{3.13}$$

where $P_l(\cos\theta)$ are the Legendre Polynomials of order l, and θ the angle between the position vector r at point P and the z-axis (Fig. 3.8). Due to the requirement that the potentials remain finite at the origin, the solution for the potentials Φ_{in} inside and Φ_{out} outside the sphere can be written as

$$\Phi_{\text{in}}(r,\theta) = \sum_{l=0}^{\infty} A_l r^l P_l(\cos\theta) \tag{3.14a}$$

$$\Phi_{\text{out}}(r,\theta) = \sum_{l=0}^{\infty} \left(B_l r^l + C_l r^{-(l+1)} \right) P_l(\cos\theta). \tag{3.14b}$$

The coefficients A_l, B_l, and C_l can now be determined from the boundary conditions at $r \to \infty$ and at the sphere surface $r = a$. The requirement that $\Phi_{\text{out}} \to -E_0 z = -E_0 r\cos\theta$ as $r \to \infty$ demands that $B_1 = -E_0$ and $B_l = 0$ for $l \neq 1$. The remaining coefficients A_l and C_l are defined by the boundary conditions at $r = a$. Equality of the tangential components of the electric field demands that

$$-\frac{1}{a}\frac{\partial\Phi_{\text{in}}}{\partial\theta}\bigg|_{r=a} = -\frac{1}{a}\frac{\partial\Phi_{\text{out}}}{\partial\theta}\bigg|_{r=a}, \tag{3.15}$$

and the equality of the normal components of the displacement field

$$-\epsilon_0\epsilon\frac{\partial\Phi_{\text{in}}}{\partial r}\bigg|_{r=a} = -\epsilon_0\epsilon_m\frac{\partial\Phi_{\text{out}}}{\partial r}\bigg|_{r=a}. \tag{3.16}$$

Application of these boundary conditions leads to $A_l = C_l = 0$ for $l \neq 1$, and via the calculation of the remaining coefficients A_1 and C_1 the potentials evaluate to **Jackson1999**

$$\Phi_{\text{in}} = -\frac{3\epsilon_m}{\epsilon + 2\epsilon_m} E_0 r\cos\theta \tag{3.17a}$$

$$\Phi_{\text{out}} = -E_0 r\cos\theta + \frac{\epsilon-\epsilon_m}{\epsilon+2\epsilon_m}E_0\frac{a^3\cos\theta}{r^2}. \tag{3.17b}$$

It is interesting to interpret equation (5.5b) physically: Φ_{out} describes the superposition of the applied field and that of a dipole located at the particle center. We can rewrite Φ_{out} by introducing the dipole moment p as

$$\Phi_{\text{out}} = -E_0 r\cos\theta + \frac{p\cdot r}{4\pi\epsilon_0\epsilon_m r^3}, \tag{3.18a}$$

$$p = 4\pi\epsilon_0\epsilon_m a^3\frac{\epsilon-\epsilon_m}{\epsilon+2\epsilon_m}E_0. \tag{3.18b}$$

We therefore see that the applied field induces a dipole moment inside the sphere of magnitude proportional to $|E_0|$. If we introduce the polarizability α, defined via $p = \epsilon_0\epsilon_m\alpha E_0$, we arrive at

$$\alpha = 4\pi a^3\frac{\epsilon-\epsilon_m}{\epsilon+2\epsilon_m}. \tag{3.19}$$

Equation (5.7) is the central result of this section, the (complex) polarizability of a small sphere of sub-wavelength diameter in the electrostatic approximation. We note that it shows the same functional form as the Clausius-Mossotti relation [47].

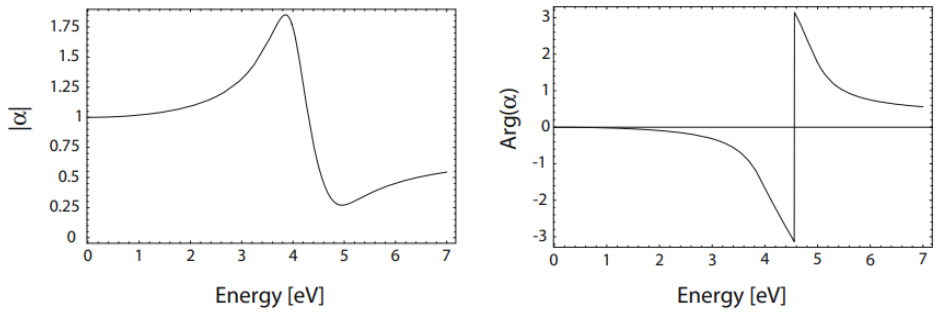

FIGURE 3.8: Absolute value and phase of the polarizability α (5.7) of a sub-wavelength metal nanoparticle with respect to the frequency of the driving field (expressed in eV units). Here, $\epsilon(\omega)$ is taken as a Drude fit to the dielectric function of silver [47].

Fig. 5.2 shows the absolute value and phase of α with respect to frequency ω (in energy units) for a dielectric constant varying as $\epsilon(\omega)$ of the Drude form (1.20), in this case fitted to the dielectric response of silver. It is apparent that the polarizability experiences a resonant enhancement under the condition that $|\epsilon+2\epsilon_m|$ is a minimum, which for the case of small or slowly-varying Im $[\epsilon]$ around the resonance simplifies to

$$\text{Re}[\epsilon(\omega)] = -2\epsilon_m. \tag{3.20}$$

This relationship is called the Fröhlich condition and the associated mode (in an oscillating field) the dipole surface plasmon of the metal nanoparticle. For a sphere consisting of a Drude metal with a dielectric function (1.20) located in air, the Fröhlich criterion is met at the frequency $\omega_0 = \omega_p/\sqrt{3}$. Equation (3.20) further expresses the strong dependence of the resonance frequency on the dielectric environment: The resonance red-shifts as ϵ_m is increased.

We note that the magnitude of α at resonance is limited by the incomplete vanishing of its denominator, due to Im $[\epsilon(\omega)] \neq 0$. This will be elaborated in the last section of this chapter on nanoparticles in gain media.

The distribution of the electric field $E = -\nabla\Phi$ can be evaluated from the potentials (5.5) to

$$E_{\text{in}} = \frac{3\epsilon_m}{\epsilon + 2\epsilon_m} E_0 \tag{3.21a}$$

$$E_{\text{out}} = E_0 + \frac{3n(n \cdot p) - p}{4\pi\epsilon_0\epsilon_m} \frac{1}{r^3}. \tag{3.21b}$$

As expected, the resonance in α also implies a resonant enhancement of both the internal and dipolar fields. It is this field-enhancement at the plasmon resonance on which many of the prominent applications of metal nanoparticles in optical devices and sensors rely.

3.5.1 Dipolar radiation

We will now leave this short summary of the properties of dipolar radiation, and refer to standard textbooks on electromagnetism such as Classical Electrodynamics Third Edition 3rd Edition by John David Jackson (Author) for further particulars. From the viewpoint of optics, it is much more interesting to note that another consequence of the resonantly enhanced polarization α is a concomitant enhancement in the efficiency with which a metal nanoparticle scatters and absorbs light. The corresponding cross sections for scattering and absorption C_{sca} and C_{abs} can be calculated via the Poynting-vector determined from (5.10) **Bohren1983** to

$$C_{\text{sca}} = \frac{k^4}{6\pi}|\alpha|^2 = \frac{8\pi}{3}k^4a^6\left|\frac{\epsilon - \epsilon_m}{\epsilon + 2\epsilon_m}\right|^2 \tag{3.28}$$

$$C_{\text{abs}} = k\text{Im}[\alpha] = 4\pi ka^3\text{Im}\left[\frac{\epsilon - \epsilon_m}{\epsilon + 2\epsilon_m}\right]. \tag{3.29}$$

For small particles with $a \ll \lambda$, the efficiency of absorption, scaling with a^3, dominates over the scattering efficiency, which scales with a^6. We point out that no explicit assumptions were made in our derivations so far that the sphere is indeed metallic. The expressions for the cross sections (5.13) are thus valid also for dielectric scatterers, and demonstrate a very important problem for practical purposes. Due to the rapid scaling of $C_{\text{sca}} \propto a^6$, it is very difficult to pick out small objects from a background of larger scatterers. Imaging of nanoparticles with dimensions below 40 nm immersed in a background of larger scatterers can thus usually only be achieved using photothermal techniques relying on the slower scaling of the absorption cross section with size.

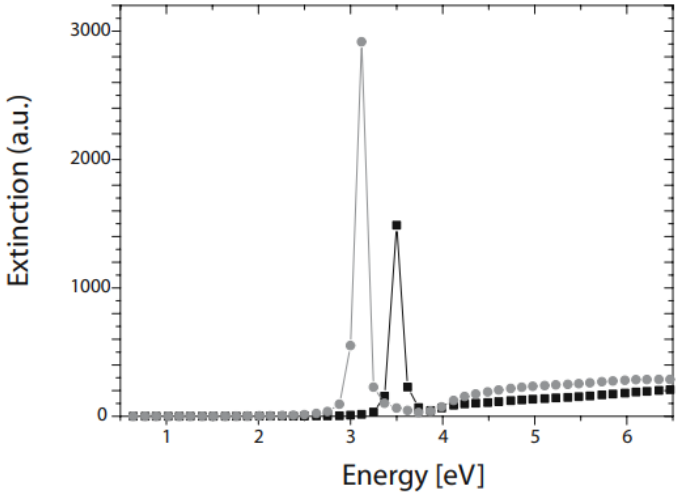

FIGURE 3.9: Extinction cross section calculated using (5.14) for a silver sphere in air (black curve) and silica (gray curve), with the dielectric data taken from **Johnson1972**.

Equations (5.13) also shows that indeed for metal nanoparticles both absorption and scattering (and thus extinction) are resonantly enhanced at the dipole particle plasmon resonance, i.e. when the Fröhlich condition (5.8) is met **Kreibig1995**. For a sphere of volume V and dielectric function $\epsilon = \epsilon_1 + i\epsilon_2$ in the quasi-static limit, the explicit expression for the extinction cross section

$$C_{\text{ext}} = C_{\text{abs}} + C_{\text{sca}} \tag{3.30}$$

is

$$C_{\text{ext}} = \frac{9\omega}{c}\epsilon_m^{3/2} V \frac{\epsilon_2}{(\epsilon_1 + 2\epsilon_m)^2 + \epsilon_2^2}. \tag{3.31}$$

Fig. 5.3 shows the extinction cross section of a silver sphere in the quasi-static approximation calculated using this formula for immersion in two different media.

We now relax the assumption of a spherical nanoparticle shape. However, it has to be pointed out that the basic physics of the localized surface plasmon resonance of a subwavelength metallic nanostructure is well described by this special case. A slightly more general geometry amenable to analytical treatment in the electrostatic approximation is that of an ellipsoid with semiaxes $a_1 \leq a_2 \leq a_3$, specified by $\frac{x^2}{a_1^2} + \frac{y^2}{a_2^2} + \frac{z^2}{a_3^2} = 1$. A treatment of the scattering problem in ellipsoidal coordinates **Bohren1983** leads to the following expression for the polarizabilities α_i along the principal axes (i = 1, 2, 3):

$$\alpha_i = \frac{4\pi a_1 a_2 a_3 (\epsilon(\omega) - \epsilon_m)}{3\epsilon_m + 3L_i(\epsilon(\omega) - \epsilon_m)} \tag{3.32}$$

L_i is a geometrical factor given by

$$L_i = \frac{a_1 a_2 a_3}{2} \int_0^\infty \frac{dq}{(a_i^2 + q) f(q)} \tag{3.33}$$

where $f(q) = \sqrt{(q + a_1^2)(q + a_2^2)(q + a_3^2)}$. The geometrical factors satisfy $\sum L_i = 1$, and for a sphere $L_1 = L_2 = L_3 = \frac{1}{3}$. As an alternative, the polarizability of ellipsoids is also often

expressed in terms of the depolarization factors $\tilde{L}_i$, defined via $E_{1i} = E_{0i} - \tilde{L}_i P_{1i}$, where E_{1i} and P_{1i} are the electric field and polarization induced inside the particle by the applied field E_{0i} along a principal axis i, respectively. $\tilde{L}$ is linked to L via

$$\tilde{L}_i = \frac{\epsilon - \epsilon_m}{\epsilon - 1} \frac{L_i}{\epsilon_0 \epsilon_m}. \tag{3.34}$$

An important special class of ellipsoids are spheroids. For prolate spheroids, the two minor axes are equal ($a_2 = a_3$), while for oblate spheroids, the two major axes are of same size ($a_1 = a_2$). An examination of (5.15) reveals that a spheroidal metal nanoparticle exhibits two spectrally separated plasmon resonances, corresponding to oscillations of its conduction electrons along the major or minor axis, respectively. The resonance due to oscillations along the major axis can show a significant spectral red-shift compared to the plasmon resonance of a sphere of the same volume. Thus, plasmon resonances can be lowered in frequency into the near-infrared region of the spectrum using metallic nanoparticles with large aspect ratio. For a quantitative treatment, we note however that (5.15) is only strictly valid as long as the major axis is significantly smaller than the excitation wavelength.

Using a similar analysis, the problem of spheres or ellipsoids coated with a concentric layer of a different material can be addressed. Since core/shell particles consisting of a dielectric core and a thin, concentric metallic shell have recently attracted a great amount of interest in plasmonics due to the wide tunability of the plasmon resonance, we want to state the result for the polarizability of a coated sub-wavelength sphere with inner radius a_1, material $\epsilon_1(\omega)$ and outer radius a_2, material $\epsilon_2(\omega)$ **Bohren1983**. The polarizability evaluates to

$$\alpha = \frac{4\pi a_2^3 (\epsilon_2 - \epsilon_m)(\epsilon_1 + 2\epsilon_2) + f(\epsilon_1 - \epsilon_2)(\epsilon_m + 2\epsilon_2)}{(\epsilon_2 + 2\epsilon_m)(\epsilon_1 + 2\epsilon_m) + f(2\epsilon_2 - 2\epsilon_m)(\epsilon_1 - \epsilon_2)}, \tag{3.2}$$

with $f = \frac{a_1^3}{a_2^3}$ being the fraction of the total particle volume occupied by the inner sphere.

3.6 Mie Theory

We have seen that the theory of scattering and absorption of radiation by a small sphere predicts a resonant field enhancement due to a resonance of the Beyond the Quasi-Static Approximation and Plasmon Lifetime 73 polarizability α (5.7) if the Frölich condition (5.8) is satisfied. Under these circumstances, the nanoparticle acts as an electric dipole, resonantly absorbing and scattering electromagnetic fields. This theory of the dipole particle plasmon resonance is strictly valid only for vanishingly small particles; however, in practice the calculations outlined above provide a reasonably good approximation for spherical or ellipsoidal particles with dimensions below 100 nm illuminated with visible or near-infrared radiation. However, for particles of larger dimensions, where the quasi-static approximation is not justified due to significant phase-changes of the driving field over the particle volume, a rigorous electrodynamic approach is required. In a seminal paper, Mie in 1908 developed a complete theory of the scattering and absorption of electromagnetic radiation by a sphere, in order to understand the colors of colloidal gold particles in solution [Mie, 1908]. The approach of what is now know as Mie theory is to expand the internal and scattered fields into a set of normal modes described by vector harmonics. The quasi-static results valid for sub-wavelength spheres are then recovered by a power series expansion of the absorption and scattering coefficients and retaining only the first term. Since Mie theory is treated in a variety of books such as [Bohren and Huffman, 1983, Kreibig and Vollmer, 1995] and a detailed knowledge of the higher order terms is not required for our purpose, we will not

present it in this treatment, but rather examine the physical consequences of the first-order corrections to the quasi-static approximation.

3.7 Physics of plasmonic heating

In this section, we consider a metal NP of complex relative permittivity $\epsilon(\omega)$ immersed in a dielectric surrounding medium of real relative permittivity $\epsilon_s = n_s^2$. This NP is illuminated by monochromatic light at an angular frequency ω with $E_0(\mathbf{r};\omega)$ the complex amplitude of the incident electric field. (For any physical quantity $A(\mathbf{r},t)$, we define its complex amplitude $A(\mathbf{r})$ such that $A(\mathbf{r},t) = \Re[A(\mathbf{r})e^{i\omega t}]$.) We define $\omega = k_0 c_0 = 2\pi c_0/\lambda_0 = 2\pi c_0/n_s\lambda = c_0 k/n_s$, where c_0 is the speed of light, λ_0 the free-space wavelength, λ the wavelength in the surrounding medium, and k_0 and k the angular wave number in free space and in the medium, respectively. [69]

3.7.1 Metallic nanoparticles and localized surface plasmons

Metal nano-objects support electronic resonances known as LSPs that can be excited upon illumination. The frequency of LSP resonances strongly depends on the morphology of the metal nano-object and its dielectric environment. For instance, elongating a sphere into a rod-like shape tends to red-shift the LSP resonance. For noble metals, such as gold, silver or copper, this property allows accurate tuning of LSP resonances from the visible to the near-infrared (NIR) frequency range. Recent advances in both bottom-up and top-down fabrication techniques offer a tremendous variety of metal NP sizes and shapes. On the one hand, chemists have developed synthesis procedures to produce colloidal noble metal NPs with numerous geometries including rods, cubes, triangles, shells, stars, etc. [34]. On the other hand, techniques such as e-beam lithography and focused ion beam milling are convenient means to design planar metal nanostructures on a flat substrate with a resolution down to a few tens of nanometers. The origin of LSP resonances in metal NPs can be simply derived for a metal sphere that is much smaller than the illumination wavelength and can be considered as an electromagnetic dipole. In this case, the sphere polarizability reads

$$\alpha(\omega) = 4\pi R^3 \frac{\epsilon(\omega) - \epsilon_s}{\epsilon(\omega) + 2\epsilon_s}. \tag{3.36}$$

where R is the radius of the sphere. In this expression, the polarizability α is defined such that the complex amplitude of the polarization vector of the NP reads $\mathbf{P} = \epsilon_0\epsilon_s\alpha E_0$. Equation (1) shows that a resonance occurs at the frequency ω at which $\epsilon(\omega) \approx -2\epsilon_s$. For a gold sphere smaller than $\sim$ 30 nm in water, this occurs for $\lambda \approx 530$ nm. However, for larger spheres, this dipolar approximation is no longer valid and more complex models, such as Mie theory, accounting for retardation effects, are required. For more sophisticated geometries, numerical simulations are needed.[70]–[72]

Such a resonance in the polarizability is responsible for a resonance both in absorption and in scattering. For any NP morphology, the efficiency of these processes can be described by absorption and scattering cross-sections [48]:

$$\sigma_{\text{abs}} = k\text{Im}(\alpha) - \frac{k^4}{6\pi}|\alpha|^2, \tag{3.37}$$

$$\sigma_{\text{scat}} = \frac{k^4}{6\pi}|\alpha|^2, \tag{3.38}$$

$$\sigma_{\text{ext}} = \sigma_{\text{abs}} + \sigma_{\text{scat}} = k\text{Im}(\alpha). \tag{3.39}$$

The relative efficiency of absorption and scattering processes can be quantified by the photothermal efficiency $\mu = \sigma_{abs}/\sigma_{ext}$, which depends mostly on the NP morphology. For instance, for spherical gold NPs smaller than 90 nm (in water), absorption is dominant ($\mu \approx 1$), while for bigger gold NPs, scattering dominates ($\mu < 1$). Note that this conclusion is valid when considering the respective maxima of both cross-section spectra, but not the cross-sections at an arbitrary wavelength. This is the consequence of the spectral shift that usually occurs between absorption and scattering spectra for large or non-spherical NPs.

Consequently, even though spherical gold NPs are usually better absorbers than scatterers, the illumination wavelength must be specified to determine what is the actual dominant energy conversion pathway. It is worth noticing that, for this reason, considering experimental extinction spectra to estimate the absorption efficiency of a plasmonic structure, as sometimes seen in the literature [73], is not always reliable. Tuning the plasmonic resonance frequency of a NP can be easily achieved by changing its morphology. Any deviation from the spherical shape tends to red-shift the resonance. Experimental results presented in Fig. 3 illustrate the red-shift of the plasmon resonance of a gold nanorod while increasing its aspect ratio. In the following, we focus on the absorption processes and the subsequent heat generation.

3.7.2 Delivered heat power

The power absorbed (and delivered) by a NP can be simply expressed using the absorption cross-section σ_{abs} introduced in the previous section:

$$Q = \sigma_{abs} I \tag{3.40}$$

where I is the irradiance of the incoming light (power per unit surface). In the case of a plane wave,

$$I = n_s c_0 \epsilon_0 |\mathbf{E_0}|^2/2.$$

The heat generation can be also derived from the heat power density $q(r)$ inside the NP such that $Q = \int_V q(r) d^3r$, where the integral runs over the NP volume V. Since the heat originates from Joule effects, the heat power density reads [10, 11]

$$q(r) = \frac{1}{2}\Re[\mathbf{J}^*(r) \cdot \mathbf{E}(r)] \tag{3.41}$$

where $\mathbf{J}(r)$ is the complex amplitude of the electronic current density inside the NP. As $\mathbf{J}(r) = i\omega\mathbf{P}$ and $\mathbf{P} = \epsilon_0\epsilon(\omega)\mathbf{E}$, one ends up with

$$q(r) = \frac{\omega}{2}\Im(\epsilon(\omega))\epsilon_0|\mathbf{E}(r)|^2. \tag{3.42}$$

The heat generation is thus directly proportional to the square of the electric field inside the metal. This is an important aspect to consider when designing efficient plasmonic nanosources of heat.

In practice there are thus two ways of calculating the heat power Q delivered by a given NP. For geometries for which the absorption cross-section is known (for example for spherical NPs using Eqs. (3.40) and (3.41)), Q can be estimated using Eq. (3.42). However, for more complicated morphologies for which there is no simple analytical expression available, the computation of the inner electric field amplitude $\mathbf{E}(r)$ is required to calculate $q(r)$ from Eq. (3.42). A gold nanorod with a resonance frequency around $\lambda_0 = 760$ nm is illuminated with a plane wave linearly polarized along its long axis. Interestingly, at resonance, most of the heat originates from the center of the rod rather than from its extremities (Fig. 4b). This can

be understood by the fact that the electronic current responsible for the Joule effect mostly flows in the center of the nanorod while the extremities mainly accumulate charges.

While the computation of the delivered heat power Q turns out to be a full-optical problem as explained in the previous section, the determination of the steady-state temperature distribution $T(r)$ inside and outside the NP is based on the resolution of the heat diffusion equation:

$$\nabla \cdot [\kappa(r)\nabla T(r)] = -q(r) \quad \text{inside the NP,} \tag{3.43}$$

$$\nabla \cdot [\kappa(r)\nabla T(r)] = 0 \quad \text{outside the NP} \tag{3.44}$$

where $\kappa(r)$ is the thermal conductivity. For a spherical NP of radius R, simple calculations lead to a temperature increase:

$$\delta T(r) = \delta T_{\text{NP}} \frac{R}{r}, \quad r > R, \tag{3.45}$$

$$\delta T(r) \approx \delta T_{\text{NP}}, \quad r < R \tag{3.46}$$

where δT_{NP} is the temperature increase of the NP. Interestingly, while the heat power density $q(r)$ can be highly non-uniform within the NP, the temperature at equilibrium is, on the contrary, generally perfectly uniform inside the NP [13]. This is due to the much larger thermal conductivity of metals as compared with that of the surroundings (liquid, glass, etc.). The actual temperature increase experienced by a NP is dependent on numerous parameters, namely its absorption cross-section, its shape, the thermal conductivity of the surrounding medium and the wavelength and irradiance of the incoming light. For a spherical NP, the NP temperature increase is related to the absorbed power $Q = \sigma_{\text{abs}} I$ according to

$$\delta T_{\text{NP}} = \frac{Q}{4\pi\kappa_s R} \tag{3.47}$$

where κ_s is the thermal conductivity of the surrounding medium.

To give an order of magnitude, a spherical gold NP in water, 20 nm in diameter, illuminated at $\lambda_0 = 530$ nm with an irradiance of $I = 1\ \text{mW}/\mu\text{m}^2$ experiences a temperature increase of $\sim 5\,^{\circ}\text{C}$. Importantly, this simple model may no longer be valid when several NPs are in close proximity as thermal collective effects can occur [27], [29], [70]. In this case, reduced irradiance can be used to achieve the same temperature increase.

The establishment of this steady-state temperature profile is usually very fast when working with NPs. The typical duration τ_{tr} of the transient regime is not dependent on the temperature increase but on the characteristic size L of the system (for instance the radius R for a sphere):

$$\tau_{\text{tr}} \sim \frac{L^2 \rho c_p}{3\kappa_s} \tag{3.48}$$

where ρ is the mass density of the NP and c_p its specific heat capacity at constant pressure. For example, for spherical NPs of diameters 10 nm, 100 nm and 1 μm, one gets τ_{tr} of the order of 0.1 ns, 10 ns and 1 μs, respectively.

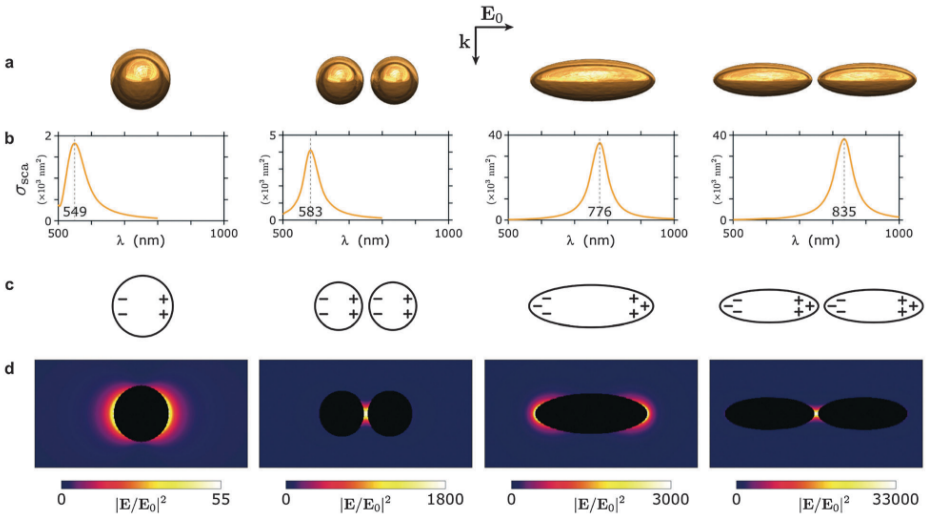

FIGURE 3.10: Influence of the NP geometry on the optical confinement and spectral features of the LSP resonance: (a) four geometries of gold NPs are considered: an isolated 50 nm sphere, a plasmonic dimer formed by two adjacent 40 nm NPs separated by 5 nm, an isolated oblate NP (100 nm long, aspect ratio of 3) and a dimer of oblate NPs (82 nm long, aspect ratio 3) separated by 5 nm. All four structures feature the same volume of gold. We consider an illumination from the top by a plane wave polarized horizontally. Sphere: 50 nm in diameter. (b) Simulations of the corresponding scattering cross sections showing the evolution of the LSP resonance (c) schematic of the charge distribution at a given time during the period of the charge oscillation. (d) Simulations of the distribution of the optical enhancement around the NPs at the respective LSP resonance wavelengths (simulations performed using the Boundary Element Method)

Chapter 4

Numerical Methods for Plasmonic Coupling

Investigating the thermo-plasmonic behavior of metallic nanostructures necessitates numerical approaches coupling optics and thermodynamics. The **boundary element method (BEM)** [74], [75], **discrete dipole approximation (DDA)** and **Green dyadic tensor (GDT)** [51], [68], [76] are the methods that have recently been extended to compute the steadystate temperature in metallic nanostructures under continuous wave illumination [62], [77].
We utilizes numerical methods to investigate the impact of plasmonic coupling and thermal accumulation on the photothermal behavior of randomly distributed silver nanoparticles. Here, to compute the light scattering and absorption by nanoparticles, we have used the DDA method in **chapter 5** and to compute the spatial distribution of temperature in steady state regime, the thermal Green's function method has been used in **chapter 5**.

4.1 Boundary Element Method (BEM)

The boundary element method (BEM) is a numerical computational method of solving linear partial differential equations which have been formulated as integral equations (i.e. in boundary integral form), including fluid mechanics, acoustics, electromagnetics (where the technique is known as method of moments or abbreviated as MoM)

4.1.1 Introduction of BEM

To provide a detailed mathematical and theoretical explanation of the Boundary Element Method (BEM) as used in the paper, I'll break down the key aspects of the methodology and its application to the problem of plasmonic coupling and photothermal effects in nanoparticles. Here's how BEM is theoretically formulated and applied:

4.1.2 Mathematical Formulation of BEM

1. **Governing Equations:** Maxwell's Equations BEM is used to solve Maxwell's equations, which govern the behavior of electromagnetic fields. The key equations are:

   - Gauss's Law for Electricity: $\nabla \cdot \mathbf{E} = \frac{\rho}{\epsilon_0}$
   - Gauss's Law for Magnetism: $\nabla \cdot \mathbf{B} = 0$
   - Faraday's Law of Induction: $\nabla \times \mathbf{E} = -\frac{\partial \mathbf{B}}{\partial t}$
   - Ampere's Law with Maxwell's Addition: $\nabla \times \mathbf{B} = \mu_0 \mathbf{J} + \mu_0 \epsilon_0 \frac{\partial \mathbf{E}}{\partial t}$

   The Maxwell's equations in the frequency domain can be written as:

$$\nabla \times (\nabla \times \mathbf{E}) - \mu \epsilon \omega^2 \mathbf{E} = -\mu \mathbf{J}$$

where $\mathbf{E}$ is the electric field, μ is the permeability, ϵ is the permittivity, and ω is the angular frequency of the incident wave. The current density $\mathbf{J}$ is related to the surface currents on the nanoparticles.

2. **Integral Representation of Fields:** For boundary element formulation, the fields are represented in terms of surface integrals over the boundaries of the domain. The electric field $\mathbf{E}$ and magnetic field $\mathbf{H}$ on the surface of the nanoparticles are expressed as:

$$\mathbf{E}(\mathbf{r}) = \int_{\Gamma} \mathbf{G}(\mathbf{r}, \mathbf{r}') \cdot \mathbf{J}(\mathbf{r}')\, d\Gamma'$$

where Γ is the surface of the nanoparticles, and $\mathbf{G}(\mathbf{r}, \mathbf{r}')$ is the Green's function that describes the response of the field at point $\mathbf{r}$ due to a unit source at $\mathbf{r}'$.

3. **Boundary Integral Equations:** The integral form of Maxwell's equations on the boundary surface Γ can be written as:

$$\mathbf{E}(\mathbf{r}) = \frac{\omega^2}{c^2} \int_{\Gamma} \mathbf{G}(\mathbf{r}, \mathbf{r}') \cdot \mathbf{J}(\mathbf{r}')\, d\Gamma' + \mathbf{E}^{\text{inc}}(\mathbf{r})$$

where $\mathbf{E}^{\text{inc}}$ is the incident electric field. Boundary Integral Equations BEM transforms the differential form of Maxwell's equations into integral equations. The boundary conditions at the surfaces of the nanoparticles are used to derive these integral equations.

For an electric field $\mathbf{E}$ and a magnetic field $\mathbf{H}$, the boundary integral equations can be written as:

$$\mathbf{E}(\mathbf{r}) = \mathbf{E}^{\text{inc}}(\mathbf{r}) + \int_{S} \left[\mathbf{G}(\mathbf{r}, \mathbf{r}') \cdot \mathbf{J}(\mathbf{r}') - \mathbf{K}(\mathbf{r}, \mathbf{r}') \cdot \mathbf{M}(\mathbf{r}') \right] dS'$$

$$\mathbf{H}(\mathbf{r}) = \mathbf{H}^{\text{inc}}(\mathbf{r}) + \int_{S} \left[\mathbf{G}(\mathbf{r}, \mathbf{r}') \cdot \mathbf{M}(\mathbf{r}') + \mathbf{K}(\mathbf{r}, \mathbf{r}') \cdot \mathbf{J}(\mathbf{r}') \right] dS'$$

where: - $\mathbf{E}^{\text{inc}}$ and $\mathbf{H}^{\text{inc}}$ are the incident electric and magnetic fields. - $\mathbf{J}$ and $\mathbf{M}$ are the electric and magnetic surface currents. - $\mathbf{G}$ and $\mathbf{K}$ are the Green's functions for the electric and magnetic fields, respectively. - S is the surface of the nanoparticle.

4. **Discretization of the Surface:** The surface Γ is discretized into small elements. Each element is typically represented by nodes with unknown surface current densities $\mathbf{J}_i$. The integral equation is then discretized as:

$$\mathbf{E}_i = \sum_j \mathbf{G}_{ij} \cdot \mathbf{J}_j + \mathbf{E}_i^{\text{inc}}$$

where $\mathbf{G}_{ij}$ are the entries of the impedance matrix, which are computed using the Green's function.

5. **Impedance Matrix and System of Equations:** The discretized system of equations can be written in matrix form as:

$$\mathbf{Z} \cdot \mathbf{J} = \mathbf{E}^{\text{inc}}$$

where $\mathbf{Z}$ is the impedance matrix, and $\mathbf{J}$ is the vector of unknown surface currents.

6. **Green's Functions**

The Green's functions $\mathbf{G}$ and $\mathbf{K}$ describe the response of the fields at a point $\mathbf{r}$ due to a unit source at another point $\mathbf{r}'$. For the electric field, the Green's function in free space

is:

$$\mathbf{G}(\mathbf{r}, \mathbf{r}') = \frac{e^{ik|\mathbf{r}-\mathbf{r}'|}}{4\pi|\mathbf{r}-\mathbf{r}'|}\left(\mathbf{I} + \frac{\nabla\nabla}{k^2}\right)$$

where k is the wave number, $\mathbf{I}$ is the identity matrix, and $\nabla\nabla$ represents the dyadic operator.

4.1.3 Mathematical and Theoretical Advantages of BEM

1. **Reduction in Dimensionality**

   - BEM converts a 3D problem into a 2D problem by focusing on the boundaries (surfaces) of the nanoparticles. This reduction in dimensionality significantly reduces the computational cost and complexity.
   - In electromagnetics, the key interactions and boundary conditions are often at the surfaces of the objects. By formulating the problem in terms of surface integrals, BEM directly addresses these critical interactions.

2. **Accurate Boundary Representation**

   - BEM solves integral equations that naturally incorporate the boundary conditions on the surfaces of the nanoparticles. The integral equations for the electric field $\mathbf{E}$ and magnetic field $\mathbf{H}$ are expressed as:

$$\mathbf{E}(\mathbf{r}) = \mathbf{E}^{\text{inc}}(\mathbf{r}) + \int_S \left[\mathbf{G}(\mathbf{r}, \mathbf{r}') \cdot \mathbf{J}(\mathbf{r}') - \mathbf{K}(\mathbf{r}, \mathbf{r}') \cdot \mathbf{M}(\mathbf{r}')\right] dS'$$

$$\mathbf{H}(\mathbf{r}) = \mathbf{H}^{\text{inc}}(\mathbf{r}) + \int_S \left[\mathbf{G}(\mathbf{r}, \mathbf{r}') \cdot \mathbf{M}(\mathbf{r}') + \mathbf{K}(\mathbf{r}, \mathbf{r}') \cdot \mathbf{J}(\mathbf{r}')\right] dS'$$

     where $\mathbf{G}$ and $\mathbf{K}$ are the Green's functions.
   - BEM provides high accuracy in representing the boundary conditions and surface interactions. This is particularly important for nanoparticles where surface effects dominate the optical response.

3. **Efficient Handling of Infinite Domains**

   - - BEM inherently handles problems in infinite or semi-infinite domains without requiring artificial truncation. This is achieved by the nature of the Green's functions, which decay with distance, automatically incorporating the effects of the infinite domain.
   - For scattering problems, the fields extend to infinity. BEM is well-suited for such problems because it avoids the need for approximations or boundary conditions at the edges of a finite computational domain, which are required in methods like FEM or FDTD.

4.1.4 Specific Application to the Paper

1. Modeling Plasmonic Coupling:

   - Plasmonic coupling involves interactions between closely spaced nanoparticles, leading to complex field distributions that are highly localized near the surfaces.
   - BEM accurately captures these surface interactions and the resulting localized fields, which are critical for understanding the photothermal behavior.

2. Computational Efficiency:
    - The study involves simulating a large number of nanoparticles, making computational efficiency crucial.
    - BEM's reduction in dimensionality and efficient handling of boundary conditions make it computationally feasible to simulate large assemblies of nanoparticles.
3. Surface Currents and Fields:
    - The fields and currents on the surfaces of the nanoparticles directly determine their scattering and absorption properties.
    - BEM's formulation in terms of surface integrals directly provides these quantities, allowing for precise computation of the optical response.

4.1.5 Numerical Implementations

1. Surface Discretization: The surface of each nanoparticle is discretized into small elements (e.g., triangles or quadrilaterals). Each element is associated with basis functions that approximate the surface currents **J** and **M**.
2. Formulating the Integral Equations: The boundary integral equations are formulated using the Green's functions. These equations relate the unknown surface currents to the incident fields.
3. Matrix Representation: The integral equations are discretized into a system of linear equations. This results in a matrix equation of the form:

$$\mathbf{ZI} = \mathbf{V}$$

    where: - **Z** is the impedance matrix, representing interactions between surface elements. - **I** is the vector of unknown surface currents. - **V** is the vector representing the incident fields.
4. Solving the Linear System: Numerical methods (e.g., iterative solvers like GMRES) are used to solve the linear system for the surface currents **I**.
5. Field Computation: Once the surface currents are known, the scattered fields are computed using the integral representation of the fields. This involves evaluating the surface integrals of the Green's functions weighted by the surface currents.
6. Post-Processing: The computed fields are used to determine quantities of interest, such as the scattering and absorption cross sections, and the near-field distribution around the nanoparticles.

The Boundary Element Method is a powerful tool for solving electromagnetic scattering problems involving nanoparticles. It leverages the boundary integral equations derived from Maxwell's equations and uses Green's functions to account for interactions at the surfaces of the nanoparticles. This method is particularly suitable for modeling the optical response of complex nanoparticle assemblies, as demonstrated in the paper.In the paper, the Boundary Element Method (BEM) is used to model the electromagnetic response of nanoparticles, particularly focusing on their scattering and absorption prop- erties. BEM particularly suitable for studying the electromagnetic re- sponse of nanoparticles, especially when dealing with plasmonic coupling and photother- mal effects. The method's ability to handle complex geometries and interactions at the sur- faces of nanoparticles is essential for accurately modeling and understanding their behavior.

4.2 Discrete Dipole Approximation (DDA) Method

The discrete dipole approximation (DDA) is a general method to compute scattering and absorption of electromagnetic waves by particles of arbitrary geometry and composition. The Discrete Dipole Approximation (DDA) method is a numerical technique used to compute the optical properties of particles, specifically nanoparticles, by representing them as an array of polarizable points (dipoles). Here's a detailed theoretical and mathematical explanation based on the paper you provided:

4.2.1 Theoretical Explanation

The DDA method is particularly useful for investigating the optical properties of nanoparticles when they are illuminated by an incident electromagnetic field. The method involves the following steps:

1. **Discretization:** The target particle is divided into an array of N sub-wavelength-sized dipoles. Each dipole is located at position $\mathbf{r}_i$ and is characterized by its polarizability $\alpha_i(\omega)$.

2. **Incident Field:** When the particle is illuminated by an incident monochromatic electric field $\mathbf{E}_{\text{inc}}(\mathbf{r}) = \mathbf{E}_0 e^{-i\omega t + i\mathbf{k}\cdot\mathbf{r}}$, each dipole experiences this incident field.

3. **Dipole Moment:** The dipole moment $\mathbf{P}_i$ of the i-th dipole is induced by the local electric field $\mathbf{E}_{\text{ext},i}$ at its location:
$$\mathbf{P}_i = \epsilon_0 \epsilon_m \alpha_i(\omega) \mathbf{E}_{\text{ext},i}$$
Here, $\alpha_i(\omega)$ is the polarizability of the i-th dipole, ϵ_0 is the permittivity of free space, and ϵ_m is the permittivity of the medium surrounding the nanoparticle.

4. **External Electric Field:** The external electric field $\mathbf{E}_{\text{ext},i}$ at the i-th dipole is the sum of the incident field and the fields scattered by all other dipoles:
$$\mathbf{E}_{\text{ext},i} = \mathbf{E}_{\text{inc},i} + \frac{k_0^2}{\epsilon_0} \sum_{j \neq i} \mathbf{G}_{ij} \cdot \mathbf{P}_j$$
where $\mathbf{E}_{\text{inc},i} = \mathbf{E}_{\text{inc}}(\mathbf{r}_i)$ and $\mathbf{G}_{ij}$ is the electric Green's tensor, which accounts for the interaction between dipoles i and j.

4.2.2 Mathematical Formulation

The mathematical steps for implementing the DDA method are as follows:

1. **Polarizability:** The polarizability $\alpha_i(\omega)$ is given by:
$$\alpha_i(\omega) = \frac{\alpha_0(\omega)}{1 - \frac{2}{3} i k^3 \alpha_0(\omega)}$$
where $\alpha_0(\omega)$ is the Clausius-Mossotti polarizability:
$$\alpha_0(\omega) = 4\pi a^3 \frac{\epsilon(\omega) - \epsilon_m}{\epsilon(\omega) + 2\epsilon_m}$$
Here, a is the radius of the dipole and $\epsilon(\omega)$ is the permittivity of the material.

2. **Green's Tensor:** The electric Green's tensor $\mathbf{G}_{ij}$ is defined as:

$$\mathbf{G}(\mathbf{r}_i, \mathbf{r}_j) = \frac{1}{4\pi}\left(\frac{e^{ik|\mathbf{r}_i-\mathbf{r}_j|}}{|\mathbf{r}_i-\mathbf{r}_j|} + \frac{\nabla\nabla e^{ik|\mathbf{r}_i-\mathbf{r}_j|}}{k^2}\right)$$

3. **System of Equations:** The induced dipole moments are found by solving a system of $3N$ linear equations:

$$\mathbf{E}_{\text{inc},i} = \sum_{j=1}^{N} \mathbf{A}_{ij} \cdot \mathbf{E}_{\text{ext},j}$$

where $\mathbf{A}_{ii} = \mathbf{I}$ (the identity matrix) and for $i \neq j$,

$$\mathbf{A}_{ij} = -k_0^2 \epsilon_m \alpha_i \mathbf{G}_{ij}$$

4. **Solution:** By solving this system of equations numerically, the external electric field $\mathbf{E}_{\text{ext},i}$ at each dipole position can be determined.

5. **Absorption and Scattering:** The absorption cross-section σ_{abs} and the scattering cross-section can be calculated from the dipole moments and the polarizability:

$$\sigma_{\text{abs}} = k\text{Im}(\alpha) - \frac{k^4}{6\pi}|\alpha|^2$$

4.2.3 Implementation of the Discrete Dipole Approximation (DDA) Method

The Discrete Dipole Approximation (DDA) method is a numerical technique used to model the interaction between light and a material object by discretizing the object into an array of polarizable points or dipoles. Here is a step-by-step theoretical and mathematical explanation of how to implement the DDA method:[42], [77]

1. **Discretization of the Target :** The first step in the DDA method is to discretize the target object into an array of N dipoles. Each dipole is located at position $\mathbf{r}_i$ and has a polarizability $\alpha_i(\omega)$.

2. **Incident Electromagnetic Field :** When the object is illuminated by an incident electromagnetic field, the electric field at the position of the i-th dipole is given by:

$$\mathbf{E}_{\text{inc}}(\mathbf{r}_i) = \mathbf{E}_0 e^{-i\omega t + i\mathbf{k}\cdot\mathbf{r}_i}$$

where $\mathbf{E}_0$ is the amplitude of the incident electric field, ω is the angular frequency, and $\mathbf{k}$ is the wave vector of the incident light.

3. **Dipole Polarization :** The dipole moment $\mathbf{P}_i$ of the i-th dipole is induced by the local electric field $\mathbf{E}_{\text{ext},i}$ at its position:

$$\mathbf{P}_i = \epsilon_0 \epsilon_m \alpha_i(\omega) \mathbf{E}_{\text{ext},i}$$

where $\alpha_i(\omega)$ is the polarizability of the i-th dipole, ϵ_0 is the permittivity of free space, and ϵ_m is the permittivity of the medium surrounding the nanoparticle.

4. **Local Electric Field :** The local electric field $\mathbf{E}_{\text{ext},i}$ at the i-th dipole is the sum of the incident electric field and the fields scattered by all other dipoles:

$$\mathbf{E}_{\text{ext},i} = \mathbf{E}_{\text{inc}}(\mathbf{r}_i) + \frac{k_0^2}{\epsilon_0}\sum_{j\neq i} \mathbf{G}_{ij} \cdot \mathbf{P}_j$$

where $\mathbf{G}_{ij}$ is the Green's tensor that accounts for the interaction between dipoles i and j.

5. **Green's Tensor :** The electric Green's tensor $\mathbf{G}_{ij}$ for the interaction between dipoles i and j is defined as:

$$\mathbf{G}(\mathbf{r}_i, \mathbf{r}_j) = \frac{1}{4\pi} \left(\frac{e^{ik|\mathbf{r}_i - \mathbf{r}_j|}}{|\mathbf{r}_i - \mathbf{r}_j|} + \frac{\nabla\nabla e^{ik|\mathbf{r}_i - \mathbf{r}_j|}}{k^2} \right)$$

6. **Polarizability :** The polarizability $\alpha_i(\omega)$ is corrected to account for the radiation reaction and dynamic depolarization:

$$\alpha_i(\omega) = \frac{\alpha_0(\omega)}{1 - \frac{2}{3} ik^3 \alpha_0(\omega)}$$

where $\alpha_0(\omega)$ is the Clausius-Mossotti polarizability:

$$\alpha_0(\omega) = 4\pi a^3 \frac{\epsilon(\omega) - \epsilon_m}{\epsilon(\omega) + 2\epsilon_m}$$

Here, a is the radius of the dipole, and $\epsilon(\omega)$ is the permittivity of the material.

7. **System of Equations :** The induced dipole moments are found by solving a system of $3N$ linear equations:

$$\mathbf{E}_{\text{inc},i} = \sum_{j=1}^{N} \mathbf{A}_{ij} \cdot \mathbf{E}_{\text{ext},j}$$

where $\mathbf{A}_{ii} = \mathbf{I}$ (the identity matrix) and for $i \neq j$,

$$\mathbf{A}_{ij} = -k_0^2 \epsilon_m \alpha_i \mathbf{G}_{ij}$$

8. **Numerical Solution :** Solve the system of linear equations to find the local electric field $\mathbf{E}_{\text{ext},i}$ at each dipole. This can be done using numerical techniques such as matrix inversion or iterative solvers.

9. **Calculate Optical Properties :** Once the local fields are known, the optical properties such as the absorption and scattering cross-sections can be computed:

$$\sigma_{\text{abs}} = \frac{k}{|\mathbf{E}_0|^2} \sum_{i=1}^{N} \text{Im} \left(\mathbf{P}_i^* \cdot \mathbf{E}_{\text{ext},i} \right)$$

$$\sigma_{\text{sca}} = \frac{k^4}{6\pi |\mathbf{E}_0|^2} \sum_{i=1}^{N} |\mathbf{P}_i|^2$$

In our work, the DDA method is used to compute the light scattering and absorption by nanoparticles, and the spatial distribution of temperature in the steady state is computed using the thermal Green's function method. The DDA method allows for the detailed analysis of the optical properties and interactions between nanoparticles, which is crucial for understanding their behavior under illumination.

4.3 Thermal Green's Function Method

The Thermal Green's Function method is a mathematical approach used to solve heat conduction problems, particularly in complex systems where direct analytical solutions are difficult or impossible to obtain. It leverages the concept of Green's functions,[74] which are fundamental solutions to differential equations, to construct the temperature distribution resulting from heat sources within a medium.

4.3.1 Theoretical Discussions

1. **Heat Conduction Equation :** The heat conduction (or diffusion) equation in a steady-state regime for a homogeneous medium is given by:

$$\nabla \cdot (\kappa \nabla T) = -q(\mathbf{r})$$

where: - T is the temperature field. - κ is the thermal conductivity of the medium. - $q(\mathbf{r})$ is the volumetric heat source density.

2. **Green's Function:** A Green's function $G(\mathbf{r}, \mathbf{r}')$ is a solution to the differential equation with a delta function source:

$$\nabla^2 G(\mathbf{r}, \mathbf{r}') = -\delta(\mathbf{r} - \mathbf{r}')$$

In the context of heat conduction, the Green's function represents the temperature response at point $\mathbf{r}$ due to a unit point heat source located at $\mathbf{r}'$.

3. **Temperature Distribution :** The temperature at any point $\mathbf{r}$ in the medium due to a distribution of heat sources can be expressed using the Green's function:

$$T(\mathbf{r}) = \int_V G(\mathbf{r}, \mathbf{r}') q(\mathbf{r}')\, d\mathbf{r}'$$

Here, V is the volume of the medium, and $q(\mathbf{r}')$ is the heat source density at point $\mathbf{r}'$.

4.3.2 Application to Nanoparticles of Thermal Green Function :

When applied to the problem of nanoparticles heated by light absorption, the Thermal Green's Function method involves the following steps:

1. **Heat Sources:** Each nanoparticle acts as a localized heat source. The power Q_i absorbed by the i-th nanoparticle can be calculated from the incident light and the absorption properties of the nanoparticle:

$$Q_i = \frac{1}{2} \sigma_{\text{abs}} n \epsilon_0 |\mathbf{E}_{\text{ext},i}|^2$$

where σ_{abs} is the absorption cross-section, n is the refractive index of the medium, ϵ_0 is the permittivity of free space, and $\mathbf{E}_{\text{ext},i}$ is the external electric field experienced by the nanoparticle.

2. **Poisson's Equation**: In the steady-state regime, the temperature distribution $T(\mathbf{r})$ is found by solving Poisson's equation for heat conduction:

$$\kappa_m \nabla^2 T(\mathbf{r}) = -\sum_{j=1}^{N} Q_j \delta(\mathbf{r} - \mathbf{r}_j)$$

Here, κ_m is the thermal conductivity of the surrounding medium, and Q_j is the heat power of the j-th nanoparticle located at $\mathbf{r}_j$.

3. Green's Function Solution: The temperature increase at any point $\mathbf{r}$ due to the heat sources can be expressed using the thermal Green's function $G_t(\mathbf{r}; \mathbf{r}_j)$:

$$\Delta T(\mathbf{r}) = \sum_{j=1}^{N} G_t(\mathbf{r}; \mathbf{r}_j) Q_j$$

For a homogeneous medium, the thermal Green's function is:

$$G_t(\mathbf{r}, \mathbf{r}_j) = \frac{1}{4\pi\kappa_m |\mathbf{r} - \mathbf{r}_j|}$$

This function represents the temperature increase at point $\mathbf{r}$ due to a unit heat source at $\mathbf{r}_j$.

4. Temperature Inside Nanoparticles: For the temperature increase inside a nanoparticle located at $\mathbf{r}_i$, it is given by:

$$\Delta T_i = \sum_{j=1}^{N} G_t(\mathbf{r}_i; \mathbf{r}_j) Q_j$$

where $G_t(\mathbf{r}_i; \mathbf{r}_i) = \frac{1}{4\pi\kappa_m a}$ for a nanoparticle of radius a.

The Thermal Green's Function method provides a systematic way to calculate the temperature distribution in a medium resulting from multiple localized heat sources. It leverages the concept of Green's functions to handle the complexity of solving Poisson's equation for heat conduction. This method is particularly useful in nanoscale applications where the spatial distribution of heat sources, such as nanoparticles, leads to non-uniform and complex temperature profiles. By applying the Green's function approach, one can obtain an accurate temperature distribution accounting for the contributions of all individual heat sources.

4.3.3 Numerical Implementation

This method is used to calculate the temperature distribution around the nanoparticles due to the absorption of light and subsequent heat generation. The thermal Green's function provides a solution to the heat diffusion equation in a steady-state regime.

1. **DDA for External Field**: The DDA method is used to compute the external electric fields $\mathbf{E}_i^{\text{ext}}$ for all nanoparticles by solving the system of linear equations derived from the interactions between dipoles.

2. **Heat Power Calculation**: The heat power absorbed by each nanoparticle is calculated using the electric field:

$$Q_i = \frac{1}{2} \sigma_{\text{abs}} nc\epsilon_0 |\mathbf{E}_i^{\text{ext}}|^2$$

3. **Temperature Distribution**: The temperature distribution $\Delta T(\mathbf{r})$ in the medium is calculated using the thermal Green's function method, accounting for contributions from all heat sources.

4.3.4 Computational Steps

- **Simulation Setup:** A MATLAB code is written to simulate the system, where $N = 1000$ silver nanoparticles are randomly distributed in a spherical region.
- Field Calculation: The DDA method is used to compute $\mathbf{E}_i^{\text{ext}}$ for each nanoparticle.
- **Heat Power Calculation:** Q_i is computed for each nanoparticle using the absorption cross section and the external electric field.
- **Temperature Calculation:** The temperature increase $\Delta T(\mathbf{r})$ is computed using the thermal Green's function method.

4.3.5 Application to Nanoparticle Systems

The work combines the DDA method for optical calculations and the thermal Green's function method for thermal calculations to investigate the photothermal behavior of randomly distributed silver nanoparticles. The numerical approach provides insights into the contributions of plasmonic coupling and thermal accumulation to the temperature increase in the nanoparticle assembly.

- **Green's Function Calculation:** The Green's function $\mathbf{G}(\mathbf{r}, \mathbf{r}')$ typically involves the solution to the Helmholtz equation with appropriate boundary conditions. For a spherical nanoparticle, it can be represented as:

$$\mathbf{G}(\mathbf{r}, \mathbf{r}') = \frac{e^{ikr}}{4\pi r}\hat{\mathbf{n}}$$

  where $k = \omega/c$ is the wave number, $r = |\mathbf{r} - \mathbf{r}'|$, and $\hat{\mathbf{n}}$ is the normal vector.

- **Setting Up the Boundary Integral Equations:** For a surface S of the nanoparticle, the boundary integral equation for the tangential components of the electric field $\mathbf{E}_t$ is:

$$\mathbf{E}_t(\mathbf{r}) = \frac{\omega^2}{c^2} \int_S \mathbf{G}(\mathbf{r}, \mathbf{r}') \cdot \mathbf{J}(\mathbf{r}')\, dS' + \mathbf{E}_t^{\text{inc}}(\mathbf{r})$$

- **Solving the Linear System:** The system of equations $\mathbf{Z} \cdot \mathbf{J} = \mathbf{E}^{\text{inc}}$ is solved using numerical techniques such as:

$$\mathbf{J} = \mathbf{Z}^{-1} \cdot \mathbf{E}^{\text{inc}}$$

4.3.6 Integration with Photothermal Analysis

- **Absorbed Power Calculation:** The power absorbed by each nanoparticle is given by:

$$Q_i = \frac{1}{2}\sigma_{\text{abs}} nc\epsilon_0 |\mathbf{E}_i^{\text{ext}}|^2$$

  where σ_{abs} is the absorption cross-section.

- **Temperature Distribution Using Thermal Green's Function:** The temperature increase $\Delta T(\mathbf{r})$ due to the absorbed power is described by solving the heat conduction equation with a thermal Green's function $G_t(\mathbf{r}, \mathbf{r}')$:

$$\nabla \cdot (\kappa \nabla T(\mathbf{r})) = -\sum_i \frac{Q_i}{\rho c} \delta(\mathbf{r} - \mathbf{r}_i)$$

where κ is the thermal conductivity, ρ is the density, and c is the specific heat capacity.

- **Final Temperature Distribution:** The temperature distribution is then computed as:

$$\Delta T(\mathbf{r}) = \sum_i G_t(\mathbf{r}, \mathbf{r}_i) \cdot \frac{Q_i}{\rho c}$$

These methods allows for a detailed and efficient study of the plasmonic and thermal interactions in nanoparticle systems.

Chapter 5

Light Scattering and Absorption by Nanoparticles

In this thesis work, we propose a unified formalism to model a large class of experimental systems composed of metallic nanostructures where photothermal effects occur. The formalism consists of further extending both the discrete dipole approximation (DDA) and Green's dyadic tensor (GDT) methods—previously devoted to electrodynamic simulations—to the description of photoinduced thermal effects, and, in particular, to compute temperature profiles. the same spirit of DDA and GDT methods, the thermal extension we developed is also based on a Green's function formalism. This thesis work is divided in two sections. The first section is dedicated to the DDA method and its thermal extension. To illustrate this approach, well suited to address problems involving colloidal nanoparticles, we investigate the heat generation and temperature distribution around nanoparticles deposited on a glass substrate. We discuss the influence of the solvent and the substrate on the expected temperature increase, as well as the physics of heat generation throughout nanoparticles arrays. The second section is dedicated to the thermal extension of the GDT method, suited for more complex geometries. This approach turns out to be nontrivial since it requires the computation of a fictive heat generation density inside the metallic structure.

5.1 Investigate the Optical Properties of Illuminated NPs.

Discrete Dipole Approximation

The DDA is a general method to investigate the optical properties of nanoparticles assembly.[51], [78] It can be used to compute absorption and scattering cross sections, optical near-field, or light-radiation diagram. DDA is particularly suited to take into account the presence of a planar interface between two dielectric media to model for example the presence of a substrate. Such a typical system is represented schematically in **figure: 5.1**.

In the following, the particles are assumed dielectric but not magnetic (magnetic permittivity $\mu = \mu_0$). The size of the particle is supposed to be small compared to the wavelength of the incoming light. The electric permittivity and the polarizability of the particles are assumed isotropic to simplify the derivations. However, extension to arbitrary dielectric tensor or ellipsoidal particles is also permitted.

Consider N identical dipolar spherical particles of radius a, polarizability α at the positions $\mathbf{r}_i$ and an incident monochromatic light characterized by a complex electric-field amplitude $\mathbf{E}_0(\mathbf{r}, \omega)$. The polarization amplitude $\mathbf{p}_i(\omega)$ of the nanoparticle i is

$$\mathbf{p}_i = \alpha(\omega)\mathbf{E}_i^{\text{ext}}(\omega) \tag{5.1}$$

$\mathbf{E}_i^{\text{ext}}(\omega)$ is the external electric field amplitude experienced by the particle i. It has two origins: the incident field $\mathbf{E}_0(\mathbf{r}_i, \omega)$ and the field radiated by the $N-1$ neighbor particles.

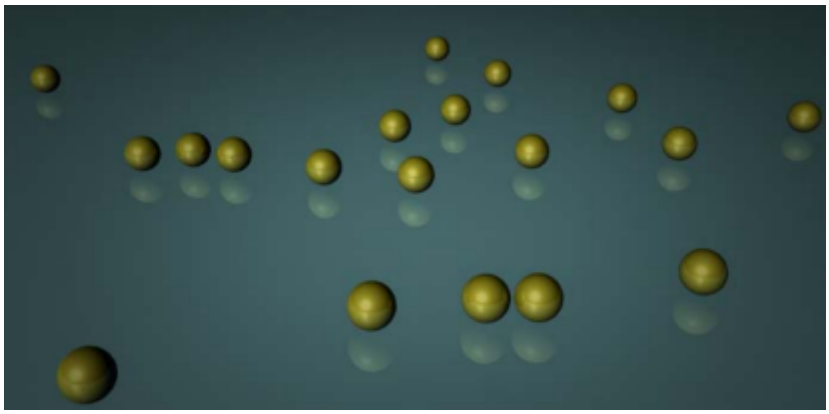

FIGURE 5.1: (Color online) Assembly of gold nanoparticles deposited on a glass substrate, which represents one of the typical systems that the DDA method can investigate.

Henceforth the ω dependency will be omitted in the equations for the sake of clarity. In the dipolar approximation, the polarizability of the particle reads

$$\alpha = \frac{\alpha_0}{1 - (2/3)ik^3\alpha_0} \tag{5.2}$$

where

$$\alpha_0 = 4\pi\epsilon_0 a^3 \frac{\epsilon - \epsilon_m}{\epsilon + 2\epsilon_m}, \tag{5.3}$$

where ϵ and ϵ_m are the electric permittivities of the nanoparticle and the surrounding medium, respectively. Formula (5.2) stands for a correction to the standard Clausius-Mossotti polarizability α_0. This correction is required to verify the optical theorem and energy conservation but can be neglected for small particles, typically less than 20 nm in diameter.

Note that in nanoplasmonics, the use of the bulk permittivity ϵ is *a priori* not straightforward since the electron mean free path is only 50 nm in gold. Some surface effects could be expected additionally to the electron-phonon interaction (Joule effect) occurring in volume and responsible for the temperature increase. However, it has been shown experimentally, in particular by Link and El-Sayed[74] and by Hartland et al.[76], that no size dependence of the electron-electron and electron-phonon relaxations exists in gold nanoparticles down to at least 9 nm in diameter. This is due to the elastic scattering of electrons by the particle surface, which does not lead to any energy transfer from electrons to surface phonons. For this reason the use of the bulk permittivity ϵ is justified.

usually sufficient and justified to describe the physical properties of gold nanoparticles.

The problem consists in calculating the electric field amplitudes $\mathbf{E}_i^{\text{ext}}$ at each particle position $\mathbf{r}_i$. Since all the particles are in interaction with each other, this problem is self-consistent. The use of the Green's dyadic tensor formalism is appropriate to simply express and formally solve the problem. The equations read[77], [78]

$$\mathbf{E}_i^{\text{ext}} = \mathbf{E}_0(\mathbf{r}_i) + \sum_{j \neq i} \mathbf{G}(\mathbf{r}_i, \mathbf{r}_j) \cdot \mathbf{p}_j \tag{5.4}$$

and can be recast using Eq. (1)

$$\mathbf{E}_i^{\text{ext}} = \mathbf{E}_0(\mathbf{r}_i) + \alpha \sum_{j \neq i} \mathbf{G}(\mathbf{r}_i, \mathbf{r}_j) \cdot \mathbf{E}_j^{\text{ext}}, \tag{5.5}$$

where $\mathbf{G}(\mathbf{r}_i, \mathbf{r}_j)$ is the electric field propagator (also called Green's dyadic tensor) associated

to the surroundings. The self-consistency is evidenced by Eq. (5). The Dyson method allows for recasting Eq. (5) into a resolved form where the self-consistency is removed[77], [78]

$$\mathbf{E}_i^{\text{ext}} = \mathbf{E}_0(\mathbf{r}_i) + \alpha \mathbf{K}(\mathbf{r}_i, \mathbf{r}_j) \cdot \mathbf{E}_0(\mathbf{r}_j), \tag{5.6}$$

where $\mathbf{K}(\mathbf{r}_i, \mathbf{r}_j)$ is the Green dyadic function of the complete system (particles plus surrounding surface). The central part of the algorithm consists in calculating the generalized propagators $\mathbf{K}(\mathbf{r}_i, \mathbf{r}_j)$, which can be done by N successive inversions of 3×3 matrices. Once the electric field amplitude $\mathbf{E}_i^{\text{ext}}$ is known at each position $\mathbf{r}_i$, it can be calculated at any position $\mathbf{r}$ using the electric field propagator

$$\mathbf{E}(\mathbf{r}) = \mathbf{E}_0(\mathbf{r}) + \alpha \sum_{j=1}^{N} \mathbf{G}(\mathbf{r}, \mathbf{r}_j) \cdot \mathbf{E}_j^{\text{ext}}. \tag{5.7}$$

External Electric Field of Nanoparticles by DDA Method

The DDA is a suitable method to investigate the optical properties of illuminated NPs. In this method, an assembly of N identical sub wavelength-sized spherical NPs are considered. Nanoparticles have been distributed in a homogeneous medium with permittivity of ϵ_m.[50], [68]

5.1.1 Incident monochromatic electric field and Dipole Moment

1. **Incident Electric Field:** When NPs are illuminated by the incident monochromatic electric field,

$$\mathbf{E}^{\text{inc}}(\mathbf{r}) = \mathbf{E}_0 \exp(-i\omega t + i\mathbf{k} \cdot \mathbf{r}) \tag{5.8}$$

   Here, $\mathbf{E}_0$ is the amplitude of the incident electric field, ω is the angular frequency, and $\mathbf{k}$ is the wave vector of the incident field.

2. **Dipole Moment of the i-th Nanoparticle:** The dipole moment of the ith nanoparticle located at $\mathbf{r}_i$ is,

$$\mathbf{P}_i = \epsilon_0 \epsilon_m \alpha_i(\omega) \mathbf{E}_i^{\text{ext}}, \tag{5.9}$$

   This equation states that the dipole moment is proportional to the external electric field, with the proportionality constant being the product of the permittivity of the medium and the polarizability of the nanoparticle. where $\alpha_i(\omega)$ is the polarizability of the ith particle and $\mathbf{E}_i^{\text{ext}} = \mathbf{E}^{\text{ext}}(\mathbf{r}_i)$ is the external electric field amplitude experienced by the ith particle which has two origins: the incident field $\mathbf{E}_i^{\text{inc}}(\mathbf{r}_i)$ and the field scattered by the $N-1$ neighbor particles.

$$\mathbf{E}_i^{\text{ext}} = \mathbf{E}_i^{\text{inc}} + \frac{k_0^2}{\epsilon_0} \sum_{j \neq i}^{N} G_{ij} \mathbf{P}_j \tag{5.10}$$

5.1.2 Total External Electric Field Experienced by the i-th Nanoparticle:

The external electric field $\mathbf{E}_i^{\text{ext}}$ is composed of the incident electric field $\mathbf{E}_i^{\text{inc}}$ and the field scattered by the $N-1$ neighboring particles:

$$\mathbf{E}_i^{\text{ext}} = \mathbf{E}_i^{\text{inc}} + \frac{k_0^2}{\epsilon_0} \sum_{j \neq i} \mathbf{G}_{ij} \cdot \mathbf{P}_j \tag{5.11}$$

Here, $\mathbf{G}_{ij}$ represents the Green's function that accounts for the propagation of the scattered field from the j-th to the i-th nanoparticle.

Here $\mathbf{E}_i^{\text{inc}} = \mathbf{E}^{\text{inc}}(\mathbf{r}_i)$ and $G_{ij} = G(\mathbf{r}_i, \mathbf{r}_j)$ is the electric Green's tensor defined as:[75]

$$G(\mathbf{r}_i, \mathbf{r}_j) = \frac{1}{4\pi}\left(1 + \frac{\nabla\nabla}{k^2}\right)\frac{e^{ik|\mathbf{r}_i - \mathbf{r}_j|}}{|\mathbf{r}_i - \mathbf{r}_j|}. \tag{5.12}$$

1. **External Electric Field:** The total external electric field $\mathbf{E}_i^{ext}$ at the position of the i-th nanoparticle is the sum of the incident electric field and the electric fields scattered by the other $N-1$ nanoparticles. This can be written as:

$$\mathbf{E}_i^{ext} = \mathbf{E}_i^{inc} + \sum_{j\neq i}^{N} \mathbf{E}_{ij}^{scat} \tag{5.13}$$

   where $\mathbf{E}_{ij}^{scat}$ is the scattered electric field from the j-th nanoparticle to the i-th nanoparticle.

2. **Scattered Electric Field:** The scattered electric field $\mathbf{E}_{ij}^{scat}$ can be expressed using the Green's function $\mathbf{G}_{ij}$ and the dipole moment $\mathbf{P}_j$ of the j-th nanoparticle:

$$\mathbf{E}_{ij}^{scat} = \frac{k_0^2}{\epsilon_0}\mathbf{G}_{ij} \cdot \mathbf{P}_j \tag{5.14}$$

3. **Substitute Scattered Field into Total External Field:** Substituting the scattered field expression into the total external field expression gives:

$$\mathbf{E}_i^{ext} = \mathbf{E}_i^{inc} + \frac{k_0^2}{\epsilon_0}\sum_{j\neq i}^{N} \mathbf{G}_{ij} \cdot \mathbf{P}_j \tag{5.15}$$

4. **Combine Equations:** Combine the expression for the dipole moment $\mathbf{P}_i$ with the expression for the total external electric field:

$$\mathbf{P}_i = \epsilon_0\epsilon_m\alpha_i(\omega)\left(\mathbf{E}_i^{inc} + \frac{k_0^2}{\epsilon_0}\sum_{j\neq i}^{N} \mathbf{G}_{ij} \cdot \mathbf{P}_j\right) \tag{5.16}$$

   Simplifying this, we get:

$$\mathbf{E}_i^{ext} = \mathbf{E}_i^{inc} + \frac{k_0^2}{\epsilon_0}\sum_{j\neq i}^{N} \mathbf{G}_{ij} \cdot \mathbf{P}_j \tag{5.17}$$

   Thus, we have derived Equation (2) from the given information:

$$\mathbf{E}_i^{ext} = \mathbf{E}_i^{inc} + \frac{k_0^2}{\epsilon_0}\sum_{j\neq i}^{N} \mathbf{G}_{ij} \cdot \mathbf{P}_j \tag{5.18}$$

   This equation shows how the external electric field at each nanoparticle is influenced by the incident electric field and the fields scattered by the neighboring nanoparticles.

5. **Dipole Moment Equation:** Substitute $\mathbf{E}_i^{\text{ext}}$ into the dipole moment equation:

$$\mathbf{P}_i = \epsilon_0\epsilon_m\alpha_i(\omega)\left(\mathbf{E}_i^{\text{inc}} + \frac{k_0^2}{\epsilon_0}\sum_{j\neq i} \mathbf{G}_{ij} \cdot \mathbf{P}_j\right) \tag{5.19}$$

In the dipolar approximation, the polarizability $\alpha_i(\omega)$ of the particle reads,[73]

$$\alpha_i(\omega) = \frac{\alpha_0(\omega)}{1 - \frac{2}{3}ik^3\alpha_0(\omega)}. \tag{5.20}$$

5.2 Green's Tensor for Electromagnetic Fields

The Green's tensor $\mathbf{G}(\mathbf{r}_i, \mathbf{r}_j)$ describes how the field scattered by the j-th particle affects the i-th particle. This tensor is derived from the Helmholtz equation in the frequency domain and represents the response of the medium to a point source.[30], [68]

1. **Helmholtz Equation**

   The Helmholtz equation in the frequency domain for a scalar field $\Phi(\mathbf{r})$ is given by:

   $$\nabla^2\Phi(\mathbf{r}) + k^2\Phi(\mathbf{r}) = -\delta(\mathbf{r} - \mathbf{r}') \tag{5.21}$$

   where k is the wavenumber and $\delta(\mathbf{r} - \mathbf{r}')$ is the Dirac delta function representing a point source at $\mathbf{r}'$.

2. **Green's Function**

   The Green's function $G(\mathbf{r}, \mathbf{r}')$ for the Helmholtz equation satisfies:

   $$\nabla^2 G(\mathbf{r}, \mathbf{r}') + k^2 G(\mathbf{r}, \mathbf{r}') = -\delta(\mathbf{r} - \mathbf{r}') \tag{5.22}$$

   In free space, the solution to this equation is:

   $$G(\mathbf{r}, \mathbf{r}') = \frac{e^{ik|\mathbf{r}-\mathbf{r}'|}}{4\pi|\mathbf{r} - \mathbf{r}'|} \tag{5.22}$$

3. **Vector Potential and Green's Tensor**

   For electromagnetic fields, we work with the vector [69] potential $\mathbf{A}$ and the electric field $\mathbf{E}$, related by:

   $$\mathbf{E} = -i\omega\mathbf{A} - \nabla\Phi \tag{5.23}$$

   The vector potential $\mathbf{A}$ satisfies a vector Helmholtz equation:

   $$\nabla^2\mathbf{A} + k^2\mathbf{A} = -\mu_0\mathbf{J} \tag{5.24}$$

   where $\mathbf{J}$ is the current density.

   The solution for $\mathbf{A}$ in terms of the Green's function is:

   $$\mathbf{A}(\mathbf{r}) = \mu_0 \int G(\mathbf{r}, \mathbf{r}')\mathbf{J}(\mathbf{r}')d^3\mathbf{r}' \tag{5.25}$$

4. **Green's Tensor for the Electromagnetic Field**

   To generalize for vector fields, we introduce the dyadic Green's function or Green's [48] tensor $\mathbf{G}(\mathbf{r}, \mathbf{r}')$ such that:

   $$\mathbf{A}(\mathbf{r}) = \mu_0 \int \mathbf{G}(\mathbf{r}, \mathbf{r}')\mathbf{J}(\mathbf{r}')d^3\mathbf{r}' \tag{5.26}$$

The Green's tensor $\mathbf{G}(\mathbf{r}, \mathbf{r}')$ satisfies:

$$\nabla^2 \mathbf{G}(\mathbf{r}, \mathbf{r}') + k^2 \mathbf{G}(\mathbf{r}, \mathbf{r}') = -\mathbf{I}\delta(\mathbf{r} - \mathbf{r}') \tag{5.27}$$

where $\mathbf{I}$ is the identity matrix.
The Green's tensor $\mathbf{G}(\mathbf{r}_i, \mathbf{r}_j)$ is derived from the vector Helmholtz equation, which governs the propagation of electromagnetic waves. It encapsulates the response of the medium to a point source and is fundamental in describing how the scattered fields from one nanoparticle influence another in the system.

5. **Electric Green's Tensor** The Green's tensor $\mathbf{G}(\mathbf{r}_i, \mathbf{r}_j)$ describes the electric field at point $\mathbf{r}_i$ due to a unit dipole located at $\mathbf{r}_j$. It is given by:

$$\mathbf{G}(\mathbf{r}_i, \mathbf{r}_j) = \frac{1}{4\pi}\left(1 + \frac{\nabla\nabla}{k^2}\right)\frac{e^{ik|\mathbf{r}_i - \mathbf{r}_j|}}{|\mathbf{r}_i - \mathbf{r}_j|} \tag{5.28}$$

6. **Solution for the Green's Tensor**

   For the electromagnetic Green's tensor, the solution in free space is:

$$\mathbf{G}(\mathbf{r}, \mathbf{r}') = \frac{1}{4\pi}\left(\mathbf{I} + \frac{\nabla\nabla}{k^2}\right)\frac{e^{ik|\mathbf{r} - \mathbf{r}'|}}{|\mathbf{r} - \mathbf{r}'|} \tag{5.29}$$

   The Green's tensor $\mathbf{G}(\mathbf{r}_i, \mathbf{r}_j)$ is derived from the vector Helmholtz equation, which governs the propagation of electromagnetic waves. It encapsulates the response of the medium to a point source and is fundamental in describing how the scattered fields from one nanoparticle influence another in the system.

   The external electric field experienced by each particle is the sum of the incident electric field and the fields produced by all other particles' dipole moments. The Green's tensor $\mathbf{G}_{ij}$ describes how the field propagates from one dipole to another. By solving these coupled equations for all particles, one can determine the response of the entire system to the incident electromagnetic field.

5.3 Polarizability of Nanoparticles

5.3.1 Clausius-Mossotti polarizability expression:

- **Induced Dipole Moment:** When an external electric field $\mathbf{E}_0$ is applied, the dipole moment $\mathbf{p}$ induced in the sphere is: **N45**

$$\mathbf{p} = \alpha_0 \mathbf{E}_0 \tag{5.30}$$

- **Potential Inside and Outside the Sphere:** - Inside the sphere, the potential is:

$$\Phi_{\text{in}} = -Br\cos\theta \tag{5.31}$$

  - Outside the sphere, the potential is:

$$\Phi_{\text{out}} = -E_0 r\cos\theta + \frac{p\cos\theta}{4\pi\epsilon_m r^2} \tag{5.32}$$

- **Boundary Conditions:** The potential and the displacement field must be continuous at the boundary $r = a$.

- **Matching Potentials:**

$$-E_0 a\cos\theta + \frac{p\cos\theta}{4\pi\epsilon_m a^2} = -Ba\cos\theta \tag{5.33}$$

$$E_0 a - \frac{p}{4\pi\epsilon_m a^2} = Ba \tag{5.34}$$

- **Matching Displacement Fields:**

$$\epsilon_m\left(E_0 + \frac{p}{4\pi\epsilon_m a^3}\right) = \epsilon(\omega)B \tag{5.35}$$

- **Solving for B:**

$$B = E_0 - \frac{p}{4\pi\epsilon_m a^3} \tag{5.36}$$

$$\epsilon_m\left(E_0 + \frac{p}{4\pi\epsilon_m a^3}\right) = \epsilon(\omega)\left(E_0 - \frac{p}{4\pi\epsilon_m a^3}\right) \tag{5.37}$$

$$\epsilon_m E_0 + \frac{p}{4\pi a^3} = \epsilon(\omega)E_0 - \frac{\epsilon(\omega)p}{4\pi\epsilon_m a^3} \tag{5.38}$$

- **Solving for p:**

$$\epsilon_m E_0 - \epsilon(\omega)E_0 = -\frac{p}{4\pi a^3} - \frac{\epsilon(\omega)p}{4\pi\epsilon_m a^3}$$

$$(\epsilon_m - \epsilon(\omega))E_0 = -p\left(\frac{1}{4\pi a^3} + \frac{\epsilon(\omega)}{4\pi\epsilon_m a^3}\right)$$

$$(\epsilon_m - \epsilon(\omega))E_0 = -p\frac{\epsilon(\omega) + 2\epsilon_m}{4\pi\epsilon_m a^3} \tag{5.39}$$

- **Final Expression for p:**

$$p = 4\pi\epsilon_m a^3 \frac{\epsilon(\omega) - \epsilon_m}{\epsilon(\omega) + 2\epsilon_m} E_0 \tag{5.40}$$

- **Polarizability $\alpha_0(\omega)$:**

$$\alpha_0(\omega) = \frac{p}{E_0} = 4\pi\epsilon_m a^3 \frac{\epsilon(\omega) - \epsilon_m}{\epsilon(\omega) + 2\epsilon_m}$$

$$\alpha_i(\omega) = \frac{\alpha_0(\omega)}{1 - \frac{2}{3}ik^3\alpha_0(\omega)} \tag{5.41}$$

where $\alpha_0(\omega)$ is the standard Clausius-Mossotti polarizability,

$$\alpha_0(\omega) = 4\pi a^3 \frac{\epsilon(\omega) - \epsilon_m}{\epsilon(\omega) + 2\epsilon_m}. \tag{5.42}$$

Here a and $\epsilon(\omega)$ are the radius and electric permittivity of the nanoparticles, respectively.

5.3.2 Polarizability for Radiation Damping:

1. **Dipole Moment and Radiation Reaction Force:**

   The radiative reaction force on a dipole can be understood by considering the self-interaction of the dipole's radiated field.[79] For a dipole moment $\mathbf{p} = \mathbf{p}_0 e^{-i\omega t}$, the

electric field at a distance r from the dipole is:

$$\mathbf{E}_{\text{rad}} = \frac{e^{ikr}}{r}\left(\mathbf{p}_0 \frac{\omega^2}{4\pi\epsilon_0 c^2}\right) \tag{5.43}$$

- **Dipole Radiation**
  When an oscillating dipole emits electromagnetic radiation, it loses energy. The power radiated by an oscillating dipole moment $\mathbf{p}$ with angular frequency ω is given by:
  $$P_{\text{rad}} = \frac{\omega^4 |\mathbf{p}|^2}{12\pi\epsilon_0 c^3} \tag{5.44}$$
  where ϵ_0 is the permittivity of free space and c is the speed of light in vacuum.
- **Force on the Dipole:**
  The back-action or self-force due to this radiated field can be written as:
  $$\mathbf{F}_{\text{rad}} = \frac{2}{3}\frac{e^2\omega^2}{4\pi\epsilon_0 c^3}\mathbf{p}_0 \frac{d^2}{dt^2}\mathbf{p} \tag{5.45}$$

2. **Effective Polarizability with Radiation Damping:**

The self-force introduces a damping term in the equation of motion for the dipole moment:

$$m\frac{d^2\mathbf{p}}{dt^2} + \gamma\frac{d\mathbf{p}}{dt} + k\mathbf{p} = q\mathbf{E}_0 e^{-i\omega t}$$

where γ includes the radiation damping contribution. The damping force is proportional to the third derivative of the dipole moment:

$$\mathbf{F}_{\text{rad}} = \frac{2}{3}\frac{\omega^3}{c^3}\mathbf{p} \tag{5.46}$$

- **Equation of Motion for the Dipole**
  The dipole moment $\mathbf{p}$ induced by an external electric field $\mathbf{E}$ can be written as:
  $$\mathbf{p}(t) = \epsilon_0 \epsilon_m \alpha(\omega)\mathbf{E}(t) \tag{5.51}$$
  Considering the time-dependent field $\mathbf{E}(t) = \mathbf{E}_0 e^{-i\omega t}$, the induced dipole moment will oscillate at the same frequency:
  $$\mathbf{p}(t) = \mathbf{p}_0 e^{-i\omega t} \tag{5.47}$$
- **Radiative Reaction Force:** The radiative reaction force arises from the interaction of the dipole with its own radiated field. This self-interaction introduces a damping term proportional to the acceleration of the dipole. The force can be written as:
  $$\mathbf{F}_{\text{rad}} \propto \frac{d^3\mathbf{p}}{dt^3} \tag{5.48}$$
  For an oscillating dipole $\mathbf{p}(t) = \mathbf{p}_0 e^{-i\omega t}$, the third time derivative introduces a term proportional to $-i\omega$:
  $$\frac{d^3\mathbf{p}}{dt^3} = -i\omega^3\mathbf{p} \tag{5.49}$$
- **Effective Equation of Motion**

The equation of motion for the dipole moment, including the radiation damping term, becomes:

$$m\frac{d^2\mathbf{p}}{dt^2} + \gamma\frac{d\mathbf{p}}{dt} + k\mathbf{p} = q\mathbf{E}e^{-i\omega t} \tag{5.50}$$

The damping term γ due to radiative reaction is:

$$\gamma = \frac{2}{3}\frac{\omega^3\alpha_0}{c^3} \tag{5.56}$$

This leads to the modified polarizability:

$$\mathbf{p} = \epsilon_0\epsilon_m\alpha_0\left(\mathbf{E} - \frac{2}{3}ik^3\mathbf{p}\right) \tag{5.51}$$

3. **Solving for Modified Polarizability**

To find the effective polarizability $\alpha(\omega)$, we rearrange the equation:

$$\mathbf{p} = \epsilon_0\epsilon_m\alpha_0\mathbf{E} - \frac{2}{3}ik^3\epsilon_0\epsilon_m\alpha_0\mathbf{p} \tag{5.52}$$

Express $\mathbf{p}$ in terms of $\alpha(\omega)$:

$$\mathbf{p} = \epsilon_0\epsilon_m\alpha_0\mathbf{E} - \frac{2}{3}ik^3\epsilon_0\epsilon_m\alpha_0\mathbf{p}$$

$$\mathbf{p}\left(1 + \frac{2}{3}ik^3\alpha_0\right) = \epsilon_0\epsilon_m\alpha_0\mathbf{E}$$

$$\mathbf{p} = \epsilon_0\epsilon_m\frac{\alpha_0}{1 - \frac{2}{3}ik^3\alpha_0}\mathbf{E} \tag{5.53}$$

Therefore, the modified polarizability including radiation damping is:

$$\alpha(\omega) = \frac{\alpha_0(\omega)}{1 - \frac{2}{3}ik^3\alpha_0(\omega)} \tag{5.54}$$

5.3.3 Solving the Linear System:

In the dipolar approximation, the polarizability $\alpha_i(\omega)$ of the particle reads,[30]
By substituting $\mathbf{P}_j$ from Eq. (1) into Eq. (2), we can obtain

$$\mathbf{E}_i^{\text{inc}} = \sum_{j=1}^{N} A_{ij} \cdot \mathbf{E}_j^{\text{ext}}. \tag{5.55}$$

In Eq. (5.55), $A_{ii} = I$ (I is a 3×3 unitary matrix) and A_{ij} is defined as:

$$A_{ij} = -k_0^2\epsilon_0\epsilon_m\alpha_i G_{ij}, \quad (j \neq i). \tag{5.56}$$

For a set of N nanoparticles that their positions are defined by $\mathbf{r}_i$, the N values of $\mathbf{E}_i^{\text{inc}}$ can be obtained directly. By inserting $\mathbf{E}_i^{\text{inc}}$ into Eq. (6) and solving the system of $3N$ linear equations numerically, the external electric field amplitude, $\mathbf{E}_i^{\text{ext}}$, at each particle position $\mathbf{r}_i$, can be calculated.

Given Equations

- **Dipole Moment:**

$$\mathbf{P}_i = \epsilon_0 \epsilon_m \alpha_i(\omega) \mathbf{E}_i^{ext} \tag{5.57}$$

- **Total External Electric Field:**

$$\mathbf{E}_i^{ext} = \mathbf{E}_i^{inc} + \frac{k_0^2}{\epsilon_0} \sum_{j \neq i}^{N} \mathbf{G}_{ij} \cdot \mathbf{P}_j \tag{5.58}$$

- **Green's Tensor:**

$$\mathbf{G}(\mathbf{r}_i, \mathbf{r}_j) = \frac{1}{4\pi} \left(1 + \frac{\nabla\nabla}{k^2}\right) \frac{e^{ik|\mathbf{r}_i - \mathbf{r}_j|}}{|\mathbf{r}_i - \mathbf{r}_j|} \tag{5.59}$$

- **Polarizability:**

$$\alpha_i(\omega) = \frac{\alpha_0(\omega)}{1 - (2/3)ik^3\alpha_0(\omega)} \tag{5.68}$$

$$\alpha_0(\omega) = 4\pi a^3 \frac{\epsilon(\omega) - \epsilon_m}{\epsilon(\omega) + 2\epsilon_m} \tag{5.60}$$

Substitution and Formulation

Substitute $\mathbf{P}_j = \epsilon_0 \epsilon_m \alpha_j(\omega) \mathbf{E}_j^{ext}$ into the expression for the external electric field:

$$\mathbf{E}_i^{ext} = \mathbf{E}_i^{inc} + \frac{k_0^2}{\epsilon_0} \sum_{j \neq i}^{N} \mathbf{G}_{ij} \cdot (\epsilon_0 \epsilon_m \alpha_j(\omega) \mathbf{E}_j^{ext}) \tag{5.61}$$

Simplify the expression:

$$\mathbf{E}_i^{ext} = \mathbf{E}_i^{inc} + k_0^2 \epsilon_m \sum_{j \neq i}^{N} \mathbf{G}_{ij} \cdot \alpha_j(\omega) \mathbf{E}_j^{ext} \tag{5.62}$$

Formulate the Linear System of Equations:

For the entire set of nanoparticles, we need to solve for the external electric field amplitudes $\mathbf{E}_i^{ext}$ at each particle position $\mathbf{r}_i$. This forms a system of linear equations:

$$\mathbf{E}_i^{inc} = \sum_{j=1}^{N} A_{ij} \cdot \mathbf{E}_j^{ext} \tag{5.63}$$

where A_{ij} is defined as:

$$A_{ij} = \begin{cases} I & \text{if } i = j \\ -k_0^2 \epsilon_m \alpha_i(\omega) \mathbf{G}_{ij} & \text{if } i \neq j \end{cases} \tag{5.64}$$

Matrix Formulation:

In matrix form, the system of equations can be written as:

$$\mathbf{E}^{inc} = \mathbf{A} \cdot \mathbf{E}^{ext} \tag{5.65}$$

Here:
- $\mathbf{E}^{inc}$ is a vector of incident electric fields.
- $\mathbf{A}$ is a matrix with elements A_{ij}.
- $\mathbf{E}^{ext}$ is a vector of external electric fields at the nanoparticles.

Solving the System:

By solving this system of $3N$ linear equations (since each $\mathbf{E}$ is a 3-dimensional vector), we can determine the external electric field amplitudes $\mathbf{E}_i^{ext}$ at each particle position $\mathbf{r}_i$.

Final Equations

Equation (5.75):

$$\mathbf{E}_i^{inc} = \sum_{j=1}^{N} A_{ij} \cdot \mathbf{E}_j^{ext} \tag{5.66}$$

Equation (5.76):

$$A_{ij} = \begin{cases} I & \text{if } i = j \\ -k_0^2 \epsilon_m \alpha_i \mathbf{G}_{ij} & \text{if } i \neq j \end{cases} \tag{5.67}$$

By solving the matrix equation $\mathbf{E}^{inc} = \mathbf{A} \cdot \mathbf{E}^{ext}$, the external electric field $\mathbf{E}_i^{ext}$ at each particle position $\mathbf{r}_i$ can be calculated. This involves inverting the matrix $\mathbf{A}$ and solving for $\mathbf{E}^{ext}$.

5.3.4 Value of External Electric Field

When NPs are illuminated by the incident monochromatic electric field,

$$\mathbf{E}_i^{\text{in}} = \sum_{j=1}^{N} A_{ij} \mathbf{E}_j^{\text{ext}} \tag{5.68}$$

Here, $A_{ii} = I$ (I is a unitary 3×3 matrix) and A_{ij} is the Interaction Matrix:

$$A_{ij} = -k_0^2 \epsilon_0 \epsilon_m \alpha_i G_{ij}, \quad (j \neq i) \tag{5.69}$$

$$\mathbf{E}_i^{\text{ext}} = \sum_{j=1}^{N} A_{ij} \mathbf{E}_j^{\text{ext}} + \frac{k_0^2}{\epsilon_0} \sum_{j \neq i} G_{ij} \mathbf{P}_j \tag{5.70}$$

Final equation is

$$\mathbf{E}_i^{\text{ext}} = \sum_{j=1}^{N} (-k_0^2 \epsilon_m \alpha_i(\omega) G_{ij}) \mathbf{E}_j^{\text{ext}} + \frac{k_0^2}{\epsilon_0} \sum_{j \neq i} G_{ij} (k_0^2 \epsilon_m \alpha_j(\omega) \mathbf{E}_j^{\text{ext}}) \tag{5.71}$$

For a set of N nanoparticles that their positions are defined by $\mathbf{r}_i$, the N values of $\mathbf{E}_i^{\text{inc}}$ can be obtained directly. Solving the system of $3N$ linear equations numerically (by **MATLAB**), the external electric field amplitude, $\mathbf{E}_i^{\text{ext}}$, at each particle position $\mathbf{r}_i$, can be calculated.

Chapter 6

Spatial Distribution of Temperature in Steady State Regime

Calculation of the Thermal Field

We now explain how the steady-state temperature distribution can be obtained from the knowledge of the electric field distribution $\mathbf{E}_i^{\text{ext}}$ [50]calculated in the previous chapter. From now on, the temperature T has to be understood as a temperature increase above the ambient temperature. In a steady-state regime, the temperature profile $T(\mathbf{r})$ throughout the system is the solution of the Poisson equation

$$\kappa \nabla^2 T(\mathbf{r}) = -q(\mathbf{r}), \tag{6.1}$$

where κ is the thermal conductivity of the medium at $\mathbf{r}$. The thermal conductivities of all the media are supposed homogeneous and isotropic. $q(\mathbf{r})$ is the heat source density. Due to light absorption, the particles are the sources of heat of the problem. For a single particle, the light absorption cross section reads

$$\sigma_{\text{abs}} = \frac{k}{4\pi\epsilon_0}\Im(\alpha) - \frac{2}{3}\frac{k^4}{(4\pi\epsilon_0)^2}|\alpha|^2. \tag{6.2}$$

The second term is usually negligible for small particles. The heat power Q_i delivered by a particle i is

$$Q_i = \sigma_{\text{abs}} In \frac{c\epsilon_0}{2} \left|\mathbf{E}_i^{\text{ext}}\right|^2 \tag{6.3}$$

where n is the optical index of the surrounding medium.

Let us consider first the case of a single isolated spherical nanoparticle ($N = 1$) at the position $\mathbf{r}_i$ in a homogeneous medium of the thermal conductivity κ. Since no heat source is present in the medium surrounding the nanoparticle, the temperature distribution outside the nanoparticle can be determined from the Laplace equation

$$\nabla^2 T(\mathbf{r}) = 0. \tag{6.4}$$

The problem can be solved analytically and easily in spherical coordinates and yields

$$T(\mathbf{r}) = T_0 \frac{a}{|\mathbf{r} - \mathbf{r}_i|} \quad \text{for} \quad |\mathbf{r} - \mathbf{r}_i| \geq a. \tag{6.5}$$

In the following, we will suppose that the thermal conductivity of the nanoparticle is much higher than the one of the surrounding medium. This approximation is usually

very good for metallic nanoparticles in a dielectric environment such as water or glass. In this case, the temperature can be considered as uniform inside the nanoparticle

$$T(\mathbf{r}) = T_0 \quad \text{for} \quad |\mathbf{r} - \mathbf{r}_i| \leq a. \tag{6.6}$$

The particle temperature T_0 can be retrieved by writing an energy conservation equation. The power going through the particle interface must equal the heat power Q delivered by the particle

$$Q = -\int_S \kappa \nabla T(\mathbf{r}) \cdot d\mathbf{S}, \tag{6.7}$$

which naturally yields

$$T_0 = \frac{Q}{4\pi\kappa a}. \tag{6.8}$$

and

$$T(\mathbf{r}) = \frac{Q}{4\pi\kappa|\mathbf{r} - \mathbf{r}_i|} \quad \text{for} \quad |\mathbf{r} - \mathbf{r}_i| \geq a. \tag{6.9}$$

Note that formula (16) involves the scalar Green's function $G(\mathbf{r}, \mathbf{r}_i)$ (that vanishes at the infinity) associated to the Poisson Eq. (8) and a Dirac source distribution $\delta(\mathbf{r} - \mathbf{r}_i)$ in an infinite homogeneous medium

$$G(\mathbf{r}, \mathbf{r}_i) = \frac{1}{4\pi\kappa|\mathbf{r} - \mathbf{r}_i|}. \tag{6.10}$$

Interestingly, it has been recently reported that the thermal energy transfer between a plasmonic nanoparticle and a surrounding liquid can be affected by a molecular coating on the nanoparticle surface since acting as a surface thermal resistance. This effect is not taken into account in our method, but we show in Appendix A that, while the nanoparticle inner temperature can be indeed modified, a thermal surface resistance does not change the temperature profile in the surrounding medium, which is what usually matters while investigating thermodinduced phenomena.
Another effect that could modify and distort the calculated temperature distribution around plasmonic structures is a possible thermoinduced fluid convection, similar to the Marangoni effect**marangoni**. We show in Appendix B that any thermoinduced fluid motion has no influence regarding the temperature profile for usual temperature increase and length scales in plasmonics.

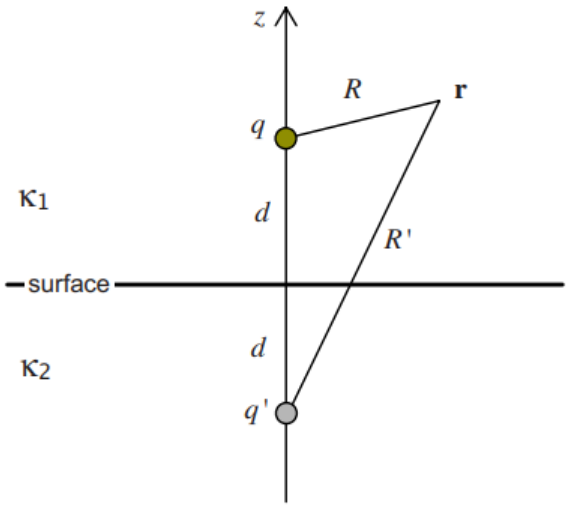

FIGURE 6.1: (Color online) The temperature distribution originating from a heat source q facing a surface can be derived by the image method usually used in electrostatics.

Let us consider now the presence of a planar interface separating two infinite media 1 and 2 [Fig. 2]. The first infinite medium has a thermal conductivity κ_1 and contains the particle and the second one has a thermal conductivity κ_2 and can stand for a glass substrate. We consider an arbitrary distance d between the center of the spheric particle and the interface. The problem consisting in calculating the temperature profile is formally equivalent to the electrostatic problem consisting in calculating the electric potential distribution created by a charge facing an interface between two dielectric media. This problem can be solved using the image method**image**. In this analogy, the temperature is equivalent to the electric potential and the thermal conductivity is equivalent to the electric permittivity. The thermal Green's function now reads

$$G(\mathbf{r},\mathbf{r}_i) = \frac{1}{4\pi\kappa_1}\left[\frac{1}{R} + \frac{\kappa_2-\kappa_1}{\kappa_2+\kappa_1}\frac{1}{R'}\right] \quad \text{for} \quad z \geq 0, \tag{6.11}$$

$$G(\mathbf{r},\mathbf{r}_i) = \frac{1}{4\pi\kappa_2 R}\left[\frac{2\kappa_2}{\kappa_2+\kappa_1}\right] \quad \text{for} \quad z \leq 0, \tag{6.12}$$

where

$$R = \sqrt{(x-x_i)^2+(y-y_i)^2+(z-d)^2}, \tag{6.13}$$

$$R' = \sqrt{(x-x_i)^2+(y-y_i)^2+(z+d)^2}. \tag{6.14}$$

Then, the temperature profile is simply given by

$$T(\mathbf{r}) = G(\mathbf{r},\mathbf{r}_i)Q. \tag{6.15}$$

Let us consider now the case of an assembly of metallic particles under illumination. At any position $\mathbf{r}$ of the medium, the temperature $T(\mathbf{r})$ is given by a linear superposition

$$T(\mathbf{r}) = \sum_{j=1}^{N} G(\mathbf{r},\mathbf{r}_j)Q_j, \tag{6.16}$$

where $G(\mathbf{r},\mathbf{r}_j)$ is the Green's function associated to the system that is given by formula (17) if the particles are in a homogeneous medium or by formula (18) if there is an

interface separating two different media.

Then, the inner temperature T_i of each particle can be retrieved this way

$$T_i = \sum_{j=1}^{N} G(\mathbf{r}_i, \mathbf{r}_j) Q_j, \tag{6.17}$$

where $G(\mathbf{r}_i, \mathbf{r}_i) = 1/(4\pi\kappa a)$ accordingly to Eq. (6.11).

Thermal Green's function method

6.1 Power Absorbed by a Nanoparticle

6.1.1 Heat Power Absorbed by the i-th Nanoparticle

- Expression for Heat Power Q_i:[47]
  The heat power Q_i absorbed by the i-th nanoparticle is given by:

$$Q_i = \frac{1}{2}\sigma_{\text{abs}} n c \epsilon_0 |\mathbf{E}_i^{\text{ext}}|^2 \tag{6.18}$$

  - σ_{abs} is the light absorption cross section of the particle.
  - $n = \sqrt{\epsilon_m}$ is the refractive index of the surrounding medium.
  - c is the speed of light in vacuum.
  - ϵ_0 is the permittivity of free space.
  - $\mathbf{E}_i^{\text{ext}}$ is the external electric field at the i-th nanoparticle.
- Light Absorption Cross Section σ_{abs}: The light absorption cross section σ_{abs} can be obtained from the polarizability $\alpha(\omega)$:

$$\sigma_{\text{abs}} = k\Im(\alpha) - \frac{k^4}{6\pi}|\alpha|^2 \tag{6.19}$$

  - k is the wave number in the medium.
  - $\Im(\alpha)$ represents the imaginary part of the polarizability α.

6.1.2 Heat Power Absorption:

The expression for the heat power Q_i absorbed by the i-th nanoparticle due to the external electric field $\mathbf{E}_i^{\text{ext}}$ is derived from the power absorbed by a dipole in an electromagnetic field. For a dipole moment $\mathbf{P}_i$, the absorbed power is given by:

$$Q_i = \frac{1}{2}\Re(\mathbf{P}_i \cdot \mathbf{E}_i^{\text{ext}*}) \tag{6.20}$$

Using the relationship $\mathbf{P}_i = \epsilon_0 \epsilon_m \alpha_i \mathbf{E}_i^{\text{ext}}$, we get:

$$Q_i = \frac{1}{2}\Re(\epsilon_0 \epsilon_m \alpha_i \mathbf{E}_i^{\text{ext}} \cdot \mathbf{E}_i^{\text{ext}*}) \tag{6.21}$$

Considering that the time-averaged power absorbed is:

$$Q_i = \frac{1}{2}\sigma_{\text{abs}} n c \epsilon_0 |\mathbf{E}_i^{\text{ext}}|^2 \tag{6.22}$$

6.1.3 Absorption Cross Section:

The absorption cross section σ_{abs} can be derived from the polarizability α. The power absorbed by a dipole can also be written as:

$$Q_i = \frac{1}{2}\omega\Im(\mathbf{P}_i \cdot \mathbf{E}_i^{\text{ext}*}) \tag{6.23}$$

Substituting $\mathbf{P}_i = \epsilon_0\epsilon_m\alpha_i\mathbf{E}_i^{\text{ext}}$ into the power absorbed expression:

$$Q_i = \frac{1}{2}\omega\epsilon_0\epsilon_m\Im(\alpha_i|\mathbf{E}_i^{\text{ext}}|^2) \tag{6.24}$$

The absorption cross section in terms of $\alpha(\omega)$ is:

$$\sigma_{\text{abs}} = k\Im(\alpha) - \frac{k^4}{6\pi}|\alpha|^2 \tag{6.25}$$

Here, the first term $k\Im(\alpha)$ represents the absorption due to the imaginary part of the polarizability, and the second term $\frac{k^4}{6\pi}|\alpha|^2$ accounts for radiative losses.

Final Equations

Equation (6.26):

$$Q_i = \frac{1}{2}\sigma_{\text{abs}}nc\epsilon_0|\mathbf{E}_i^{\text{ext}}|^2 \tag{6.26}$$

Equation (6.27):

$$\sigma_{\text{abs}} = k\Im(\alpha) - \frac{k^4}{6\pi}|\alpha|^2 \tag{6.27}$$

These equations describe the power absorbed by a nanoparticle due to light absorption and the absorption cross section in terms of the polarizability of the nanoparticle.

6.2 Poisson's Equation in a steady-state regime.

Poisson's Equation for Temperature Profile

- **Poisson's Equation:** In a steady-state regime, the temperature profile $T(\mathbf{r})$ throughout the system is the solution of Poisson's equation:

$$\nabla \cdot (\kappa(\mathbf{r})\nabla T(\mathbf{r})) = -q(\mathbf{r}) \tag{6.28}$$

  Here: - $\kappa(\mathbf{r})$ is the thermal conductivity of the medium at position $\mathbf{r}$.
  - $q(\mathbf{r})$ is the heat source density at position $\mathbf{r}$.

- **Heat Source Density:** The absorbed power Q_i of the i-th nanoparticle and the heat source density $q(\mathbf{r})$ are related by the integral over the volume V_i of the nanoparticle:

$$Q_i = \int_{V_i} q(\mathbf{r}')\, d\mathbf{r}' \tag{6.29}$$

- **Assumption of Uniform Temperature**: It is assumed that the thermal conductivity of the nanoparticle is much higher than that of the surrounding medium. This means the temperature within the nanoparticle can be considered uniform.

Relationship Between Absorbed Power and Heat Source Density

- **In a steady-state regime, the temperature distribution** $T(\mathbf{r})$ in a medium with spatially varying thermal conductivity $\kappa(\mathbf{r})$ due to a heat source density $q(\mathbf{r})$ is governed by: [80]

$$\nabla \cdot (\kappa(\mathbf{r}) \nabla T(\mathbf{r})) = -q(\mathbf{r}) \tag{6.30}$$

  This equation describes how heat diffuses through a medium and how it is affected by internal heat sources.

- **Heat Source Density** $q(\mathbf{r})$: The heat power Q_i absorbed by a nanoparticle is distributed over its volume, leading to a heat source density $q(\mathbf{r})$. For the i-th nanoparticle:

$$Q_i = \int_{V_i} q(\mathbf{r}')\, d\mathbf{r}' \tag{6.31}$$

  This relationship shows that the total power absorbed by the nanoparticle is the integral of the heat source density over the volume of the nanoparticle.

- U**niform Temperature Approximation**: For metallic nanoparticles in a dielectric environment (e.g., water or glass), the thermal conductivity of the nanoparticle is much higher than that of the surrounding medium. Hence, the temperature within the nanoparticle can be approximated as uniform. This simplifies the problem, as the temperature gradient inside the nanoparticle is negligible, and the heat source density can be considered constant over the nanoparticle volume.

- **Combining the Equations**: Using the fact that the temperature T is uniform inside the nanoparticle, we can rewrite the integral in terms of the volume V_i and the uniform heat source density $q(\mathbf{r})$:

$$Q_i = q_i V_i \tag{6.32}$$

  Here, q_i is the average heat source density within the nanoparticle.

- **Poisson's Equation for Temperature Profile (Equation 10):**

$$\nabla \cdot (\kappa(\mathbf{r}) \nabla T(\mathbf{r})) = -q(\mathbf{r}) \tag{6.34}$$

- **Relationship Between Absorbed Power and Heat Source Density (Equation 11):**

$$Q_i = \int_{V_i} q(\mathbf{r}')\, d\mathbf{r}' \tag{6.35}$$

  This describes how the temperature profile in the medium is affected by the absorbed power of the nanoparticles and how the absorbed power is related to the heat source density within the nanoparticle's volume.

6.2.1 Poisson's Equation for Temperature Profile

(a) **Poisson's Equation**: From Equation (10), in a homogeneous medium with thermal conductivity κ_m, the temperature profile $T(\mathbf{r})$ is given by:

$$\kappa_m \nabla^2 T(\mathbf{r}) = -q(\mathbf{r}) \tag{6.36}$$

(b) **Point Sources of Heat**: If we consider nanoparticles as point sources of heat, the heat source density $q(\mathbf{r})$ can be represented using Dirac delta functions $\delta(\mathbf{r} - \mathbf{r}_j)$

centered at the positions of the nanoparticles. Thus, for N nanoparticles:

$$q(\mathbf{r}) = \sum_{j=1}^{N} Q_j \delta(\mathbf{r} - \mathbf{r}_j) \tag{6.37}$$

Substituting this into the Poisson's equation, we get:

$$\kappa_m \nabla^2 T(\mathbf{r}) = -\sum_{j=1}^{N} Q_j \delta(\mathbf{r} - \mathbf{r}_j) \tag{6.38}$$

(c) **Simplifying Poisson's Equation**: Rearranging, we obtain:

$$\nabla^2 T(\mathbf{r}) = -\frac{1}{\kappa_m} \sum_{j=1}^{N} Q_j \delta(\mathbf{r} - \mathbf{r}_j) \tag{6.39}$$

Solving Poisson's Equation using Green's Function

(d) **Green's Function Solution**: The solution to the Poisson equation can be expressed using the Green's function $G(\mathbf{r}; \mathbf{r}_j)$, which satisfies:

$$\nabla^2 G(\mathbf{r}; \mathbf{r}_j) = -\delta(\mathbf{r} - \mathbf{r}_j) \tag{6.40}$$

For a homogeneous medium, the Green's function is given by:

$$G(\mathbf{r}; \mathbf{r}_j) = \frac{1}{4\pi|\mathbf{r} - \mathbf{r}_j|} \tag{6.41}$$

(e) **Temperature Increase:** The temperature increase at position $\mathbf{r}$ due to a heat source at $\mathbf{r}_j$ is:

$$\Delta T(\mathbf{r}) = \frac{Q_j}{4\pi\kappa_m|\mathbf{r} - \mathbf{r}_j|} \tag{6.42}$$

Summing over all heat sources (nanoparticles), the total temperature increase is:

$$\Delta T(\mathbf{r}) = \sum_{j=1}^{N} \frac{Q_j}{4\pi\kappa_m|\mathbf{r} - \mathbf{r}_j|} \tag{6.43}$$

i. **Temperature Distribution Outside Nanoparticles:**

$$\Delta T(\mathbf{r}) = \sum_{j=1}^{N} G(\mathbf{r}; \mathbf{r}_j) Q_j \tag{6.44}$$

where:

$$G(\mathbf{r}; \mathbf{r}_j) = \frac{1}{4\pi\kappa_m|\mathbf{r} - \mathbf{r}_j|} \tag{6.45}$$

ii. **Temperature Inside Nanoparticles:** Considering the temperature inside the i-th nanoparticle at $\mathbf{r}_i$:

$$\Delta T_i = \sum_{j=1}^{N} G(\mathbf{r}_i; \mathbf{r}_j) Q_j \tag{6.46}$$

where:

$$G(\mathbf{r}_i; \mathbf{r}_i) = \frac{1}{4\pi\kappa_m a} \tag{6.47}$$

(f) **Explanation and Analysis**

i. Thermal Green's Function $G(\mathbf{r}; \mathbf{r}_j)$: The Green's function describes the temperature response at $\mathbf{r}$ due to a unit heat source at $\mathbf{r}_j$.

$$G(\mathbf{r}; \mathbf{r}_j) = \frac{1}{4\pi\kappa_m |\mathbf{r} - \mathbf{r}_j|} \tag{6.48}$$

ii. **Temperature Profile:** The temperature profile outside the nanoparticles is obtained by summing the contributions from all heat sources, each weighted by their respective Green's function. Inside a nanoparticle, the temperature is considered uniform and is influenced by the heat sources both within and outside it.

iii. **Inverse Proportional Dependence**: The inverse proportional dependence of $G(\mathbf{r}; \mathbf{r}_j)$ on $|\mathbf{r} - \mathbf{r}_j|$ indicates that the temperature increase is more significant closer to the heat source and decreases with distance.

In summary, these steps outline how the Poisson equation for temperature distribution in a medium with point heat sources is solved using Green's functions, leading to the expressions for temperature increase both inside and outside the nanoparticles.

6.3 Thermal Accumulation Effect on steady state regime

The thermal accumulation effect [51], [76] concerns the thermal diffusion process in the nanoparticle ensemble. The temperature increase ΔT experienced by the i^{th} nanoparticle is the sum of the temperature increase due to its own heat generation ΔT_S and the temperature increase due to the heat generated by the other $N-1$ nanoparticles, ΔT_{ext}.

- **Total Temperature Increase at the i^{th} Nanoparticle:**
  The temperature increase $\Delta T(\mathbf{r}_i)$ at the position of the i^{th} nanoparticle due to all the heat sources is:

$$\Delta T(\mathbf{r}_i) = \sum_{j=1}^{N} G_t(\mathbf{r}_i, \mathbf{r}_j) Q_j \tag{6.49}$$

- **Contribution from Own Heat Generation and External Sources:**
  The total temperature increase $\Delta T(\mathbf{r}_i)$ at the i^{th} nanoparticle is split into two contributions:
  - ΔT_S: Temperature increase due to its own heat generation.
  - ΔT_{ext}: Temperature increase due to the heat generated by the other $N-1$ nanoparticles.

  Then,

$$\Delta T(\mathbf{r}_i) = \Delta T_S + \Delta T_{\text{ext}} \tag{6.50}$$

- **Own Heat Generation Contribution (ΔT_S):**
  The temperature increase at $\mathbf{r}_i$ due to its own heat generation is:

$$\Delta T_S = G_t(\mathbf{r}_i, \mathbf{r}_i) Q_i \tag{6.51}$$

- **Heat Generation from Other Nanoparticles (ΔT_{ext}):** The temperature increase at $\mathbf{r}_i$ due to the heat generated by the other nanoparticles is:

$$\Delta T_{\text{ext}} = \sum_{j \neq i}^{N} G_t(\mathbf{r}_i, \mathbf{r}_j) Q_j \tag{6.52}$$

- **Final Expression:**

$$\Delta T(\mathbf{r}_i) = G_t(\mathbf{r}_i, \mathbf{r}_i) Q_i + \sum_{j \neq i}^{N} G_t(\mathbf{r}_i, \mathbf{r}_j) Q_j = \frac{Q_i}{4\pi\kappa_m a} + \sum_{j \neq i} \frac{Q_j}{4\pi\kappa_m |\mathbf{r}_i - \mathbf{r}_j|} \tag{24}$$

$$\Delta T(\mathbf{r}_i) = \Delta T_S + \Delta T_{\text{ext}} \tag{6.53}$$

The thermal accumulation effect corresponds to the second term at the right hand in Eq. (24). When the thermal accumulation effect is negligible, the second term at the right hand in Eq. (24) is negligible. Each nanoparticle in the nanoparticle ensemble can be treated as an isolated hot spot.

$$\Delta T(\mathbf{r}_i) = \Delta T_S + \Delta T_{\text{ext}} \tag{6.54}$$

6.3.1 Find the value of ΔT_{ext}:

To combine the three equations into one, we need to express the temperature increase ΔT_{ext} in terms of the absorbed power Q_i and the absorption cross section σ_{abs}.
Here are the equations provided:

- Heat power absorbed by the i-th nanoparticle:

$$Q_i = \frac{1}{2} \sigma_{\text{abs}} nc\epsilon_0 |\mathbf{E}_i^{\text{ext}}|^2 \tag{6.55}$$

- Absorption cross section:

$$\sigma_{\text{abs}} = k\Im(\alpha) - \frac{k^4}{6\pi} |\alpha|^2 \tag{6.56}$$

- Temperature increase due to external sources:

$$\Delta T_{\text{ext}} = \sum_{j \neq i}^{N} G_t(\mathbf{r}_i, \mathbf{r}_j) Q_j \tag{6.57}$$

We will substitute the expression for Q_i into the equation for ΔT_{ext}.

Express Q_i using σ_{abs}:

$$Q_i = \frac{1}{2} \left(k\Im(\alpha) - \frac{k^4}{6\pi} |\alpha|^2 \right) nc\epsilon_0 |\mathbf{E}_i^{\text{ext}}|^2 \tag{6.58}$$

Substitute Q_j into ΔT_{ext}:

$$\Delta T_{\text{ext}} = \sum_{j \neq i}^{N} G_t(\mathbf{r}_i, \mathbf{r}_j) \left[\frac{1}{2} \left(k\Im(\alpha) - \frac{k^4}{6\pi} |\alpha|^2 \right) nc\epsilon_0 |\mathbf{E}_j^{\text{ext}}|^2 \right] \tag{6.59}$$

Final Combined Equation Combining all these, we get:

$$\Delta T_{\text{ext}} = \sum_{j \neq i}^{N} G_t(\mathbf{r}_i, \mathbf{r}_j) \left[\frac{1}{2} \left(k \Im(\alpha) - \frac{k^4}{6\pi} |\alpha|^2 \right) nc\epsilon_0 |\mathbf{E}_j^{\text{ext}}|^2 \right] \tag{6.60}$$

This single equation encapsulates the relationship between the temperature increase ΔT_{ext}, the absorbed power Q_j, and the absorption cross section σ_{abs} through the Green's function G_t and the external electric field $\mathbf{E}_j^{\text{ext}}$.

To combine the equations and find the final expression for ΔT_{ext}, we'll incorporate the given expression for $\mathbf{E}_i^{\text{ext}}$ into the already combined equation.

- **Temperature increase due to external sources:**

$$\Delta T_{\text{ext}} = \sum_{j \neq i}^{N} G_t(\mathbf{r}_i, \mathbf{r}_j) Q_j \tag{6.61}$$

- **External electric field:**

$$\mathbf{E}_i^{\text{ext}} = \sum_{j=1}^{N} \left(-k_0^2 \epsilon_m \alpha_i(\omega) \mathbf{G}_{ij} \mathbf{E}_j^{\text{ext}} + \sum_{j \neq i} \mathbf{G}_{ij} (k_0^2 \epsilon_m \alpha_j(\omega) \mathbf{E}_j^{\text{ext}}) \right) \tag{6. 62}$$

- **Express Q_i using σ_{abs}:**

$$Q_i = \frac{1}{2} \left(k \Im(\alpha) - \frac{k^4}{6\pi} |\alpha|^2 \right) nc\epsilon_0 |\mathbf{E}_i^{\text{ext}}|^2 \tag{6.63}$$

- **Substitute $\mathbf{E}_i^{\text{ext}}$ into the expression for Q_i:** Substitute the expression for $\mathbf{E}_i^{\text{ext}}$ into the Q_i equation:

$$\mathbf{E}_i^{\text{ext}} = \sum_{j=1}^{N} \left(-k_0^2 \epsilon_m \alpha_i(\omega) \mathbf{G}_{ij} \mathbf{E}_j^{\text{ext}} + \sum_{j \neq i} \mathbf{G}_{ij} (k_0^2 \epsilon_m \alpha_j(\omega) \mathbf{E}_j^{\text{ext}}) \right) \tag{6.64}$$

- Final Combined Expression
  Combining everything together:

$$\Delta T_{\text{ext}} = \sum_{j \neq i}^{N} G_t(\mathbf{r}_i, \mathbf{r}_j) \left[\frac{1}{2} \left(k \Im(\alpha) - \frac{k^4}{6\pi} |\alpha|^2 \right) nc\epsilon_0 |\mathbf{E}_j^{\text{ext}}|^2 \right] \tag{6.65}$$

This expression captures the relationship between the temperature increase ΔT_{ext}, the absorbed power Q_j, the absorption cross section σ_{abs}, the external electric field $\mathbf{E}_i^{\text{ext}}$, and the Green's function G_t.

Chapter 7

Experimental Methods and Results

7.1 Experimental Data

In this thesis work, We explored the influence of plasmonic coupling on the thermal properties of a randomly distributed collection of silver nanoparticles. The temperature rise profiles for these illuminated nanoparticles were calculated using the discrete dipole approximation method and the thermal Green's function. The findings indicate that plasmonic coupling with neighboring nanoparticles and thermal accumulation lead to a photothermal response in a nanoparticle assembly that differs from that of an isolated nanoparticle. The individual impacts of plasmonic coupling and thermal accumulation on the temperature increase have been qualitatively determined.
Building on the theoretical framework outlined in the preceding section, we developed a MATLAB program capable of calculating the spatial temperature distribution in a system of N identical spherical nanoparticles dispersed randomly within a homogeneous medium. This software first calculates the external electric field $\mathbf{E}_i^{ext}$ experienced by each nanoparticle using the discrete dipole approximation (Eq. 5.71) and determines the heat generation Q_i from Eq. 6.58. Subsequently, using the thermal Green's function method (Eqs. (6.44) and (6.46)), it evaluates the spatial distribution of the temperature rise both inside and outside the nanoparticles. The computational time required to process the temperature increase for $N = 1000$ nanoparticles on an Intel® Core™ i5-4150 CPU with 8.00 GB RAM is 105.51 seconds. Additionally, the time to compute the temperature rise in a two-dimensional area of the surrounding medium on a 1500 × 1500 grid, with a resolution of $\Delta x = \Delta y$ (or Δz) = 0.5 nm, is 323.21 seconds.

TABLE 7.1: Experimental Data

Parameter	**Value**
No. of Nanoparticles (N)	1000
Diameter of NPs	10 nm
Radius of Spherical Regiona (R)	250 nm
Incident Light I_0	$I_0 = 0.5mW/\mu m^2$
Thermal conductivity κ_m	$0.6Wm^1K^1$

7.2 Experimental Methods

7.2.1 Photothermal behavior of a single nanoparticle

By setting $N = 1$ in our simulation code, the temperature increase of a single NP can be obtained. **figure: 7.1**, displays the calculated temperature increase versus free space wavelength of incident light for a single NP.

As it can be seen in the figure, the maximum temperature increase, $\Delta T_{\max} = 2.7\,\mathrm{K}$, occurs at the wavelength of $\lambda_{sp} = 380\,\mathrm{nm}$, which corresponds to plasmonic resonance wavelength of silver NP in water [22] . For wavelengths far from plasmonic resonance, the temperature increase is insignificant.

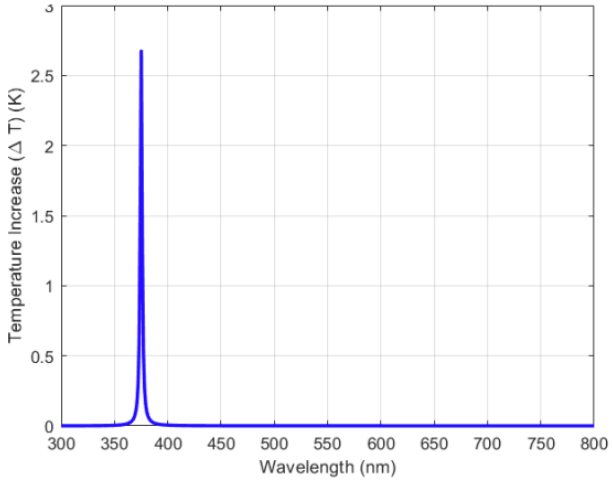

FIGURE 7.1: Temperature increase versus incident light wavelength, for a single silver nanoparticle in water. The diameter of NP is 10 nm and the intensity of incident light is 0.5 $mW/\mu m^2$. [81]

7.2.2 Photothermal behavior of a random distribution of nanoparticles

The spatial profile of temperature increase for an assembly of $N = 1000$, non-overlapping nanoparticles which randomly distributed inside a spherical region in water was calculated. The random distribution that we have used in our simulation is a uniform random distribution generated by MATLAB® software. The wavelength of the incident light was the plasmonic resonance wavelength of single NP.
Nanoparticles exhibit intriguing properties when exposed to light, especially in the context of localized heating. Here, we investigate the photothermal behavior of a system comprising 1000 NPs randomly positioned within a spherical volume filled with water. Our simulation employs a uniform random distribution to ensure that the NPs do not overlap, allowing us to study their individual and collective responses.

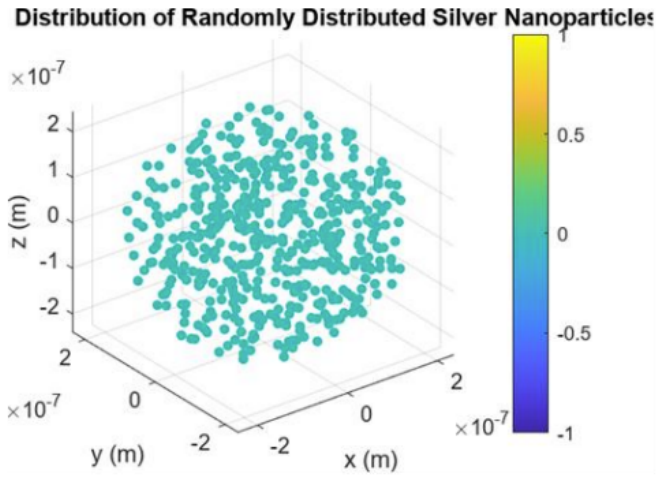

FIGURE 7.2: Randomly Distributed 1000 Nanoparticles in 3D Region [81]

When incident light interacts with an NP, energy is absorbed, leading to electron excitation. This absorbed energy subsequently dissipates as heat, raising the NP's temperature. The spatial distribution of temperature within the NP assembly depends on several factors. Our experimental setup is as follows:

- Radius of the Spherical Region: $R = 250$ nm
- Simulation Software: MATLAB and Python
- Device Configuration: Intel Core i5 and 16 GB RAM

7.3 Experimental Outcomes:

7.3.1 Plasmonic Coupling Between NPs

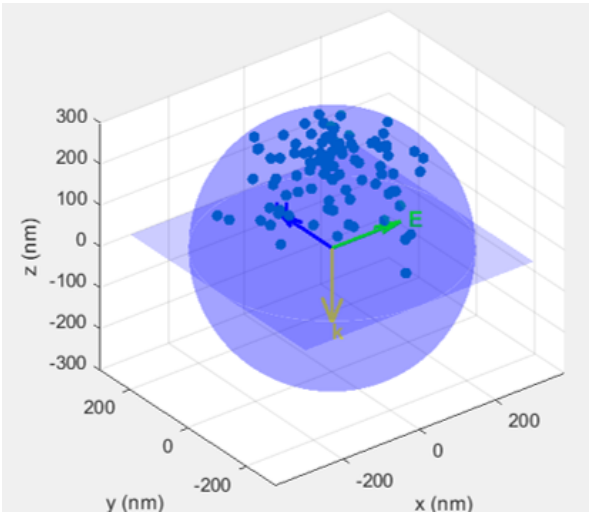

FIGURE 7.3: Schematic drawing of the structure under study, where silver nanoparticles have been distributed randomly inside a spherical region in water and a $\hat{x}$ polarized light illuminates them. [81]

The random distribution that we have used in our simulation is a uniform random distribution generated by MATLAB® software. The wavelength of the incident light was the plasmonic resonance wavelength of a single NP.

The spatial profile of temperature increase for an assembly of $N = 1000$, non-overlapping nanoparticles which randomly distributed inside a spherical region in water (the structure depicted in Fig. 7.3) was calculated.

In Fig. 7.4, we have presented the $2D$ map of calculated temperature increase on the surfaces of $z = 0$ and $y = 0$ (cross section of the region in which NPs have been distributed with the x-y plane and x-z plane, respectively).

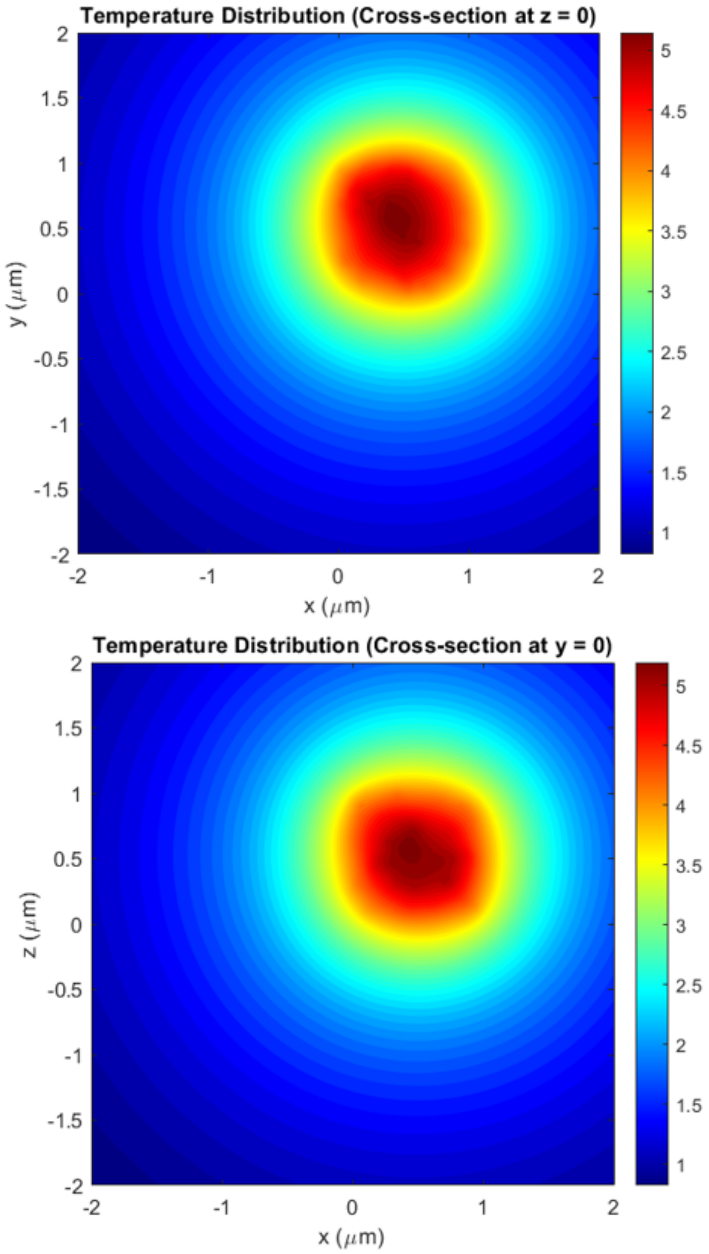

FIGURE 7.4: The 2D maps of spatial profiles of temperature increase on the surfaces of $z = 0$(a) and $y = 0$(b) for an assembly of 1000 interacting silver nanoparticles. The diameter of NPs is 10 nm and the wavelength and intensity of incident light are $\lambda_p = 380$ nm and $I_0 = 0.5$ mW/μm^2, respectively. [81]

According to the obtained results, different NPs, depending on their location in the distribution, have different temperature increases ranging from 42 K to 82.6 K. These temperatures are higher than the temperature of a single isolated NP (Fig. 6.1).

This difference is due to two effects: thermal superposition effects (where each NP experiences the diffused heat flux of nearby NPs, governed by Eq. (15)) and the effect of plasmonic coupling between NPs (the second term on the right-hand side of Eq. (2)).

In order to check the generality of the results that have been obtained for one random distribution, we repeated our calculation for 10 different random distributions. In Table 1, the mean value of temperature increase of NPs and its standard deviation for each random distribution have been presented. The grand mean (mean of these 10 mean values) of temperature increase and its grand standard deviation are 64.59 (K) and 0.52 (K), respectively. So we can say that changing random distribution does not change the results significantly.

TABLE 7.2: The mean values of temperature increase of NPs and standard deviations for 10 different random distributions.

No.	**1**	**2**	**3**	**4**	**5**	**6**	**7**	**8**	**9**	**10**
δT_{mean} (K)	64.26	65.47	63.90	63.97	65.12	64.16	64.88	64.88	64.84	64.44
Std (K)	9.66	9.97	9.81	9.60	9.84	9.36	9.89	9.89	9.63	9.17

7.3.2 Without Plasmonic Coupling

To investigate the contribution of the plasmonic coupling effect, we recalculated the temperature profile (for the same random distribution of NPs as in Fig. 7.4) under the condition where plasmonic coupling was assumed to be ignored. By ignoring the second term on the right-hand side of Eq. (6.54), we assumed that all NPs experienced only the electric field of incident light. It means the ith NP of the assembly only absorbs the heat power of $Q_i = \sigma_{abs} I_0$, and NPs can only interact via thermal superposition effect. The result of this calculation has been presented in Fig. 7.5.

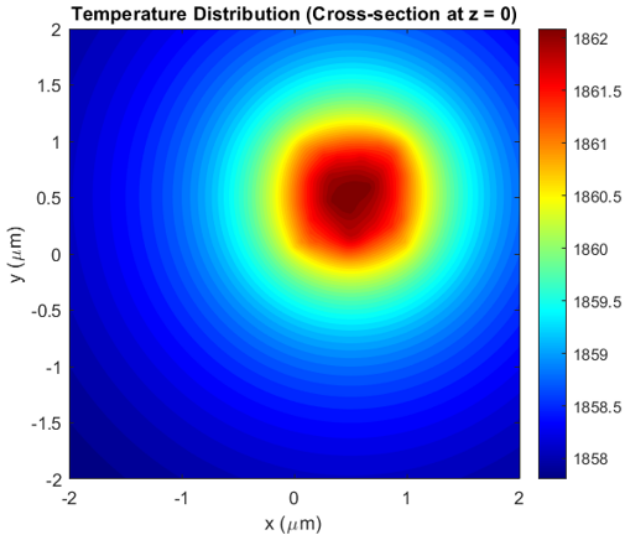

FIGURE 7.5: The *2D* map of spatial profile of temperature increase for the case which plasmonic coupling between NPs has assumed to be ignored. [81]

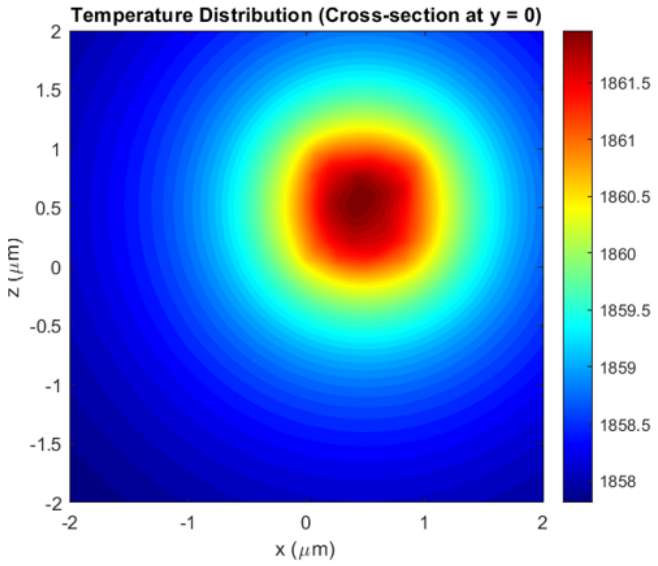

FIGURE 7.6: The *2D* map of spatial profile of temperature increase for the case which plasmonic coupling between NPs has assumed to be ignored. [81]

The results show that in this condition, the temperature increase of NPs is significantly higher in comparison with the case where NPs are coupled.

It should be noted that Eq. (6.54) (for the case with plasmonic coupling) includes the effect of light attenuation. As we can see from Fig. 7.5(b), due to this effect, there is an overall temperature decrease in the direction of light incidence ($\hat{z}$). In the case of uncoupled NPs (Fig.7.5(b)), this attenuation effect is absent. Ignoring this light attenuation has a consequence: in the case of without plasmonic coupling, the temperature we calculate for NPs in the lower part of the sphere (farther from the light source) is higher than their real values because these NPs should receive the attenuated light intensity. As can be seen from Fig. 7.4(b), in the case of coupled NPs, light attenuation caused a temperature difference in the order of 10 K in the z direction. By ignoring the light attenuation, an inaccuracy in the order of 10 K occurs in calculating the temperature for those NPs which are in the lower part of the spherical region.

On the other hand, NPs on the most upper part of the sphere (closer to the light source) receive almost the full intensity of light. So we can say that for these NPs, the calculated temperatures (in the case of without plasmonic coupling) are close to their real values. If we compare the temperature of these NPs in both cases (Figs.7.4(b) and 7.5(b)), we can see that decoupling leads to a temperature increase in the order of 100 K. This temperature increase, which occurs due to the decoupling of NPs, is one order of magnitude higher than the inaccuracy that may occur due to ignoring light attenuation.

7.3.3 Plasmonic Coupling and Thermal Superposition

To investigate the combined effects of plasmonic coupling and plasmonic superposition, we have recalculated the temperature profile (for the same random distribution of NPs as in Fig. 7.4) considering both phenomena. By including the second term on the right-hand side of Eq. (6.54), we accounted for the interactions between NPs due to both plasmonic coupling and the electric field of the incident light. This means each NP in the assembly not only absorbs heat power $Q_i = \sigma_{\text{abs}} I_o$ but also interacts via plasmonic superposition and coupling effects.

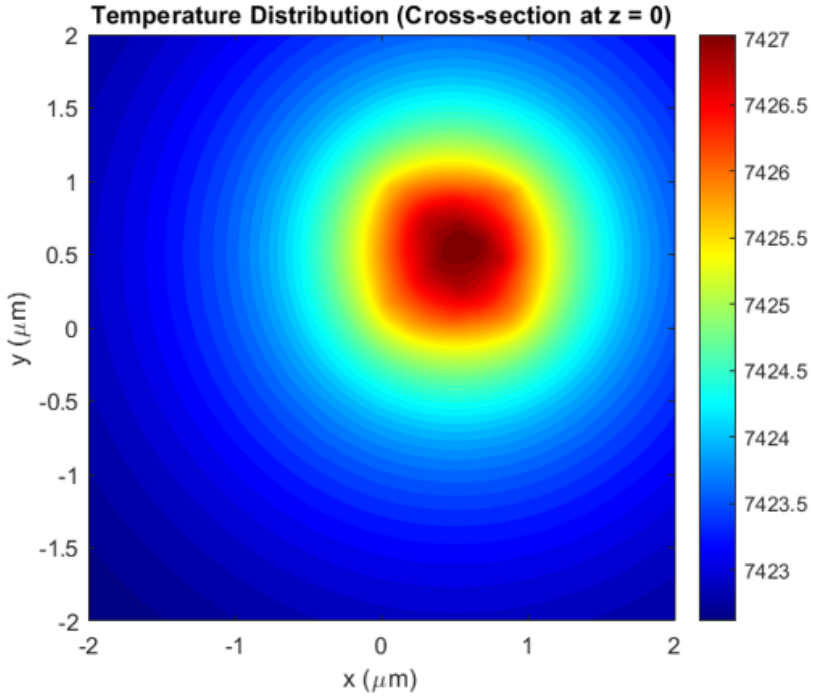

FIGURE 7.7: The 2D maps of spatial profiles of temperature increase on the surfaces of Z = 0, for an assembly of 1000 interacting silver nanoparticles. Which shows Plasmonic Coupling with Thermal Superposition effetcs.[81]

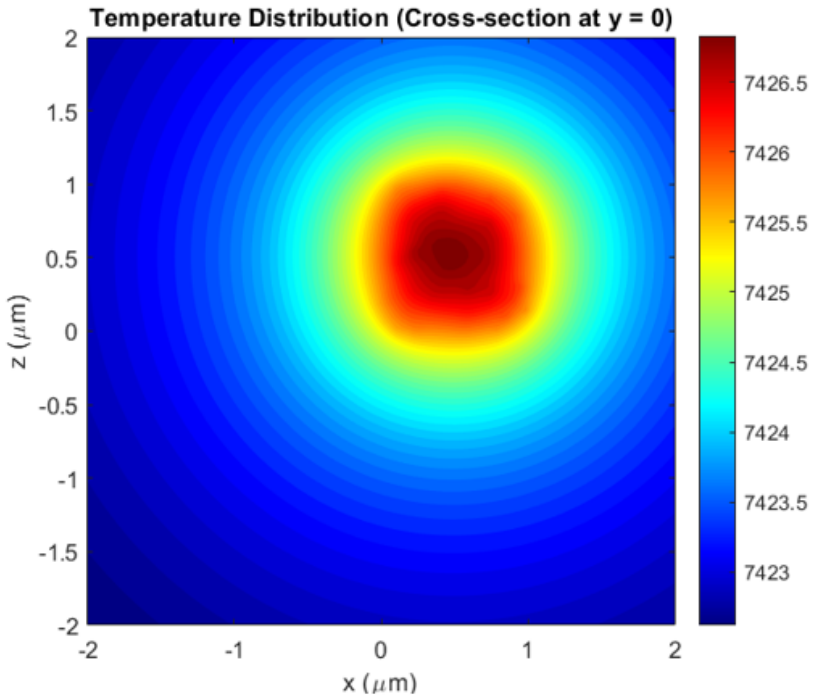

FIGURE 7.8: The 2D maps of spatial profiles of temperature increase on the surfaces of X = 0, for an assembly of 1000 interacting silver nanoparticles. Which shows Plasmonic Coupling with Thermal Superposition effetcs.[81]

The results show that under these conditions, the temperature increase of NPs is significantly affected by the combined effects of plasmonic coupling and superposition, compared to the case where only plasmonic coupling was considered.

It should be noted that Eq. (6.54) (for the case with plasmonic coupling and superposition) includes the effect of light attenuation. As we can see from Fig. 3(b), due to this effect, there is an overall temperature decrease in the direction of light incidence ($-\hat{z}$). In the case of considering both plasmonic coupling and superposition (Fig. 7.8), the attenuation effect is accurately represented. This accurate representation is because when we include the second term on the right-hand side of Eq. (6.54), we also account for the attenuation of light due to absorption by individual NPs and their mutual interactions.

Incorporating this light attenuation ensures that the calculated temperature for NPs in the lower part of the sphere (farther from the light source) reflects their true values, as these NPs receive attenuated light intensity. As observed from Fig. 3(b), in the case of coupled NPs, light attenuation causes a temperature difference in the order of 10 K in the z direction. Thus, including this attenuation leads to a more accurate temperature calculation.

NPs in the upper part of the sphere (closer to the light source) receive nearly the full intensity of light. Therefore, for these NPs, the calculated temperatures (considering plasmonic coupling and superposition) are close to their real values. Comparing the temperature of these NPs in both cases (Figs.7.5 and 7.7, we see that the combined effects of coupling and superposition result in a temperature increase of approximately 100 K.This temperature increase which occurs due to the decoupling of NPs is one order of magnitude higher than the inaccuracy which may occur due to ignoring light attenuation.

7.3.4 Thermal Accumulation Effect

To investigate the contribution of the thermal accumulation effect, we have recalculated the temperature profile (for the same random distribution of NPs as in Fig. 3) under the condition where thermal accumulation is considered.

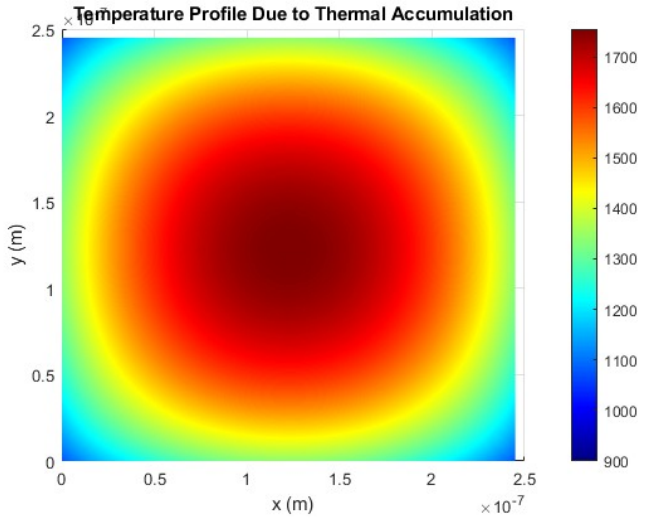

FIGURE 7.9: The 2D map of spatial profile of temperature increase for the case of thermal accumulation

By including the second term on the right-hand side of Eq. (2), we accounted for the interactions between NPs due to the thermal accumulation effect. This means each NP in the assembly not only absorbs heat power $Q_i = \sigma_{\text{abs}} I_o$ but also interacts via the thermal accumulation effect.

The results show that under these conditions, the temperature increase of NPs is significantly affected by the thermal accumulation effect compared to the case where this effect was ignored.

From the thermal side, light absorption by each nanoparticle in the ensemble heated the whole nanoparticle ensemble cumulatively, namely accumulative (collective) heating effect.

Chapter 8

Result Analysis and Conclusion

8.1 Experimental Outcomes:

As our goal was calculate the the effect of plasmonic coupling on the photothermal behavior of random NPs is that will plasmonic coupling work in favor of the application, because of the field enhancement? Or will it work against it, because it shifts the plasmonic resonance wavelength? Based on theoretical model presented in the previous section, a computer code was written in MATLAB® software which is capable to compute the spatial distribution of temperature in a system of N identical spherical NPs distributed randomly in a homogeneous medium. This code first calculates $\mathbf{E_i}^{ext}$ experienced by each nanoparticle by means of DDA method (Eq. (6)) and obtains the values of Q_i from Eq. (8). Next, by means of thermal Green's function method (Eqs. (13) and (15)), it computes the spatial distribution of temperature increase outside and inside of the nanoparticles

Temperature Distribution among NPs :

The histogram diagrams (fig 8.2) of temperature increase distribution among NPs for both cases related to Figures from 8.2 have been shown. To explain the obtained higher temperature in the case of non interacting NPs, we can say that when the plasmonic coupling is ignored, all of the NPs behave as single NP which the illuminated wavelength coincides with their plasmonic resonance wavelength.
So, every NP absorbs the maximum heat power and heats up to the maximum temperature increase (2.7 K) individually. In addition, each NP picks up extra temperature from the diffused heat flux of nearby particles due to the thermal superposition. In the case of coupled NPs, each groups of nearby NPs in distribution form a cluster and each cluster has plasmonic resonance wavelength which is different from the wavelength of incident light (which has been considered as wavelength of plasmonic resonance of single NP). Hence, in this situation, NPs absorb lower heat power in comparison with the resonant non-interacting NPs.

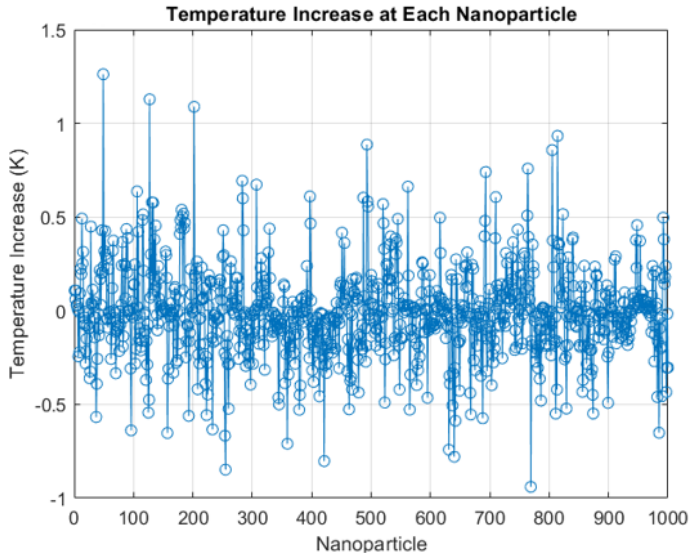

FIGURE 8.1: Temperature increase due to plasmonic coupling and thermal effects each nanoparticle

In Fig. 9.2, the absorption spectra of the system of coupled NPs have been compared with the one without plasmonic coupling. The total absorbed power of the system of NPs assembly is the sum of absorbed power by all NPs ($Q_t = \sum Q_i$). Where, for the case with plasmonic coupling, the absorbed power, Q_i, by each NP is calculated by using Eq. (8). And when the plasmonic coupling between NPs is assumed to be ignored, all of NPs absorb the same power of $Q_i = \sigma_{abs} I_0$.

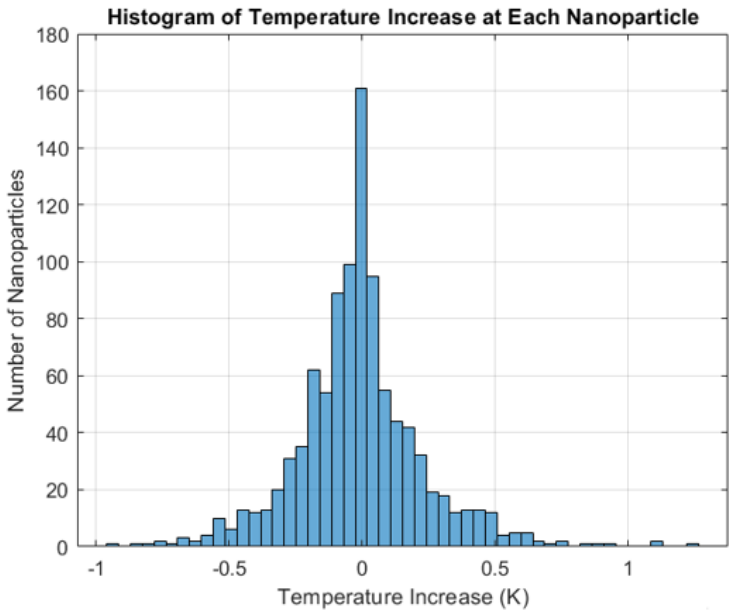

FIGURE 8.2: Temperature increase due to plasmonic coupling and thermal effects each nanoparticle [81]

As can be seen from this figure, at the single particle resonance wavelength ($\lambda_{sp} = 380$ nm), plasmonic coupling causes that the hole system of NPs, absorbs less power in comparison with the case of uncoupled NPs.

Absorption spectra of the system of NPs:

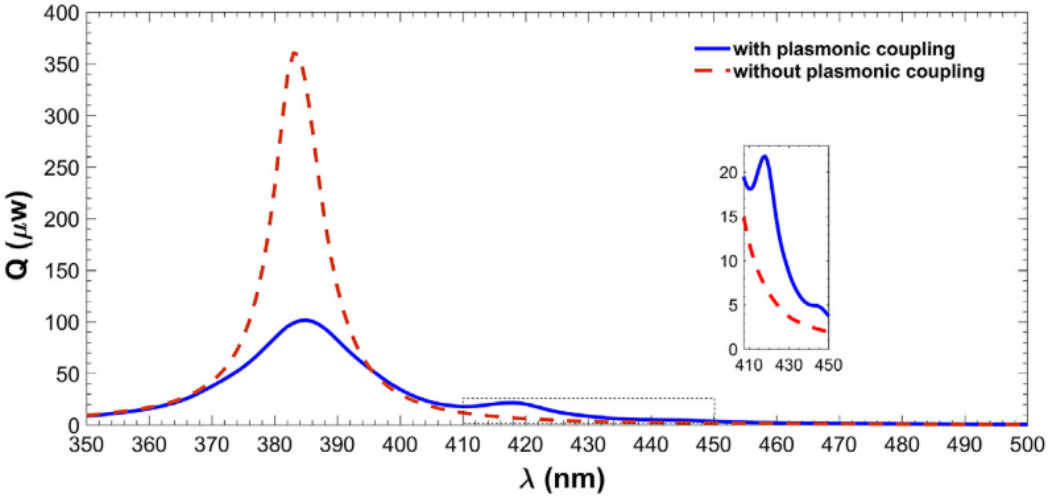

FIGURE 8.3: Two different cases where in the one case NPs are coupled (solid line) and in the other case the plasmonic coupling has assumed to be ignored (dashed line) [81]

On the other hand, for the wavelengths far from single NP plasmonic resonance (especially around $\lambda = 400$ nm), clustering can lead to heat up NPs to higher temperatures in compression with non-coupled NPs.

In Fig. 7, the histogram diagrams of temperature increase distribution among NPs, for both cases of coupled and non-coupled NPs, at the wavelength of $\lambda = 400$ nm, have been shown.

Thermal Superposition

According to Fig. 2, the temperature increase of a single NP at the wavelength of $\lambda = 400$ nm, is insignificant (about 0.17 K) and as can be seen from Fig. 7, without plasmonic coupling, due to thermal superposition, NPs could heat up to temperature increase ranging from 3.3 K to 5.1 K.

In the real case coupled NPs heat up to higher temperature increase ranging from 9.4 K to 13.5 K. These observed high temperatures are related to NP clusters which their plasmonic resonance wavelengths are close to wavelength of incident light.

For this case, the absorbed power, Q_i, by each NP of the assembly was calculated and the histogram diagram of absorbed powers has been shown in Fig. 8. If the plasmonic coupling between NPs be assumed to be ignored, at the wavelength of $\lambda = 400$ nm, all of NPs absorb the same power $Q \sim 0.01\mu$w.

As can be seen from Fig. 8, in the case with plasmonic coupling, there are dimer, trimer and tetramer NP clusters which absorb high amount of powers in comparison with the absorbed power by most of NPs in assembly. These are the clusters which their plasmonic resonance is close to the incident light wavelength. These resonant clusters by absorbing the high amount of power and diffusing heat to their surroundings raise the temperature of the whole assembly.

Investigating other cases with different concentrations of NPs approved the generality of our results. These investigations showed that for higher concentration, the number

of resonant clusters (for the wavelength far from the plasmonic resonance of a single NP) is increased.

This can be a consequence of increasing the probability of aggregation of NPs in higher concentrations.

Final Discussions:

In this part of the study, we hypothesized that increasing the interparticle distances to gradually decouple the nanoparticles would cause the distributions depicted in Figure 8.3 to converge. To test this, we examined another set of 1000 nanoparticles, keeping all parameters the same as in the previous setup except for setting the radius R at 300 nm and ensuring that the interparticle distances were no less than 30 nm. The resulting temperature increase histograms for this modified distribution are presented in Figure 8.2. Reducing the plasmonic coupling effect between the nanoparticles, the two distributions start to merge.

TABLE 8.1: Number of Nanoparticles for different temperature changes (ΔT) with and without plasmonic coupling

ΔT **(K)**	**Number of Nanoparticles (with coupling)**	**Number of Nanoparticles (without coupling)**
0-2	160	150
2-4	120	110
4-6	80	70
6-8	40	30
8-10	20	10
10-12	60	50
12-14	40	30
14-16	20	10
16-18	10	5
18-20	5	2
20-22	2	1
22-24	1	0
24-26	0	0
26-28	0	0
28-30	0	0
30-32	0	0
32-34	0	0

TABLE 8.2: Distribution of absorbed power (Q) among coupled NPs at $\lambda = 420$ nm

Q (μW)	Number of Nanoparticles
0.0 - 0.05	1000
0.05 - 0.1	30
0.1 - 0.15	20
0.15 - 0.2	10
0.2 - 0.25	0
0.25 - 0.3	0
0.3 - 0.35	20
0.35 - 0.4	40
0.4 - 0.45	30

TABLE 8.3: Temperature Increase Distribution Among Nanoparticles (NPs)

ΔT (K)	With Plasmonic Coupling	Without Plasmonic Coupling
30 - 50	10	0
50 - 70	30	0
70 - 90	60	0
90 - 110	50	0
110 - 130	20	0
130 - 150	0	10
150 - 170	0	40
170 - 190	0	60
190 - 210	0	50
210 - 230	0	30
230 - 250	0	20
250 - 270	0	10

8.2 Conclusion

In this thesis work, we quantitatively assessed the distinct impacts of plasmonic coupling and thermal accumulation on the temperature elevation in a randomly distributed array of silver nanoparticles when illuminated. Our findings reveal that at wavelengths distant from a single nanoparticle's plasmonic resonance, plasmonic coupling among neighboring nanoparticles in a cluster can significantly elevate temperatures beyond what is observed in non-coupled nanoparticles. Conversely, at the plasmonic resonance wavelength of a single nanoparticle, plasmonic coupling tends to decrease the temperature rise compared to a group of resonant, non-coupled nanoparticles. Overall, this study demonstrates that in a random nanoparticle ensemble, while thermal accumulation consistently enhances photothermal applications, the effect of plasmonic coupling on heating depends on the wavelength of the incident light.

Chapter 9

Applications

In recent years, thermo-plasmonics found a wide range of applications in nanotechnologies especially in biology and medicine such as Photothermal cancer therapy [82] [83], Drug delivery [84], Nanosurgery[85][86] and Photothermal imaging [87]. Almost in all the applications, we encounter with a random distribution of many NPs. In the case of low concentration, where NPs are far enough from each other and the interaction between them can be ignored, the photothermal behavior of the distribution can be considered as the summation of the response of individual noninteracting NPs [88].

A nano-source of heat is certainly one of the most fundamental tools from which science can benefit to investigate some of the most intimate processes in nature. The high level of heat control at the nanoscale achieved by plasmonic NPs provides scientists with a powerful tool that has already been exploited in a variety of fields. The aim of this section is to review some of the most active applications of thermo-plasmonics. Most of these applications are based on the use of gold NPs [89]. The predominance of gold over other noble metals is justified by its unique combination of advantages:

- Gold leads to resonances that can be tuned from the visible to the NIR, by adjusting the size and the shape of the NPs; it is thus well suited for applications in biology since tissues are less absorbent in the NIR range;
- Gold offers rich and simple surface chemistry that allows functionalization of gold NPs with a variety of chemical compounds;
- The oxidation of gold remains very weak; and
- Gold is not cytotoxic [90]–[92].

9.1 Plasmonic photothermal therapy

Photothermal therapy uses photothermal nano-agents to treat disease by local hyperthermia [93]–[97]. In the specific case of cancer, the main idea of this emerging therapy is to artificially enhance the optical absorption contrast between cancerous and healthy tissues. This way, a suitable illumination enables specific photo-damage of cancer tissues without affecting the healthy surrounding. Among available photothermal agents, plasmonic NPs are very good candidates to achieve photo-damage using moderate laser intensity. To eventually end up with an efficient treatment using gold NPs, several requirements have to be fulfilled.

First, gold NPs need to be specifically delivered to the cancer cells in order to limit the heat generation to the malignant tissues and not to the surrounding healthy tissues. Targeting of cancer cells with gold NPs can be either passive or active [95]. The passive approach exploits the fact that, due to their rapid growth, cancer cells are endowed with vasculatures (up to 2 μm in size) that facilitate NP uptake. Additionally,

the lymphatic drainage of tumors is reduced compared with healthy tissues, making it harder for NPs to leave the tumor once they get into it. In the active approach, targeting of cancer cells is achieved by coating the NP surface with antibodies, proteins or other ligands that have a specific binding affinity with receptors overexpressed at the membrane of cancer cells.
The second aspect that has to be considered is the wavelength of the incident light used to heat the NPs. Indeed, light absorption of human tissues is minimum in the socalled transparency window (between 700 and 900 nm). Working in this region of the spectrum allows reaching tumors that can be up to several centimeters deep, along with minimum absorption and thus less heating from the rest of the exposed tissues that are not targeted with NPs. While light absorption of spherical gold NPs peaks in the green, LSP resonances can be shifted to the infrared by using nonspherical NPs. This explains why hyperthermia experiments are mainly based on the use of gold nanoshells [96][98]–[100] (formed by a dielectric core surrounded by a thin gold layer), gold nanorods [101] or gold nanocages[102], which allow accurate tuning of LSPs to the NIR spectral region. In somecases, the use of spherical gold NPs can also be efficient due to agglomeration of NPs that tends to red-shift the NP absorption spectrum [103]–[105].
In the original work introducing the use of gold NPs for plasmonic photothermal therapy (PPTT), Hirsch and co-workers used human breast carcinoma cells incubated with gold nanoshells in vitro [106]. The cells were found to have undergone photothermally induced morbidity upon exposure to NIR light (820 nm, $35W/cm^2$). Conversely, cells without nanoshells displayed no loss in viability using the same NIR illumination conditions. Also, exposure to low doses of NIR light (820 nm, $4W/cm^2$) in solid tumors treated with metal nanoshells reached average maximum temperature increases capable of inducing irreversible tissue damage ($\Delta T = 37.4 \pm 66^0C$) within 4–6 min. Importantly, controls treated without nanoshells demonstrated significantly lower average temperature increase on exposure to NIR light ($\Delta T > 10^0C$). Shortly after [107], the feasibility of this approach was successfully tested in vivo on a mouse model. Gold nanoshells coated with polyethylene glycol (PEG) were intravenously injected into mice. The tumor was then illuminated with a diode laser over sessions of 3 min. After 10 days of treatment, complete resorption of the tumor was observed. More than 90 days after the treatment, all treated mice remained healthy and free of tumors. At about the same time, Pitsillides et al. proposed to use nanosecond-pulsed laser irradiation for more efficient PPTT [108]. This series of experiments was performed in the visible range using spherical gold NPs. Those authors demonstrated that when using pulsed laser illumination, the brief but intense temperature increase following a short laser pulse yields a fast vaporization of a thin layer around the NPs causing more efficient cancer cell denaturation as compared with CW illumination. The use of gold nanorods was first proposed by the El-Sayed group a few years later [100].

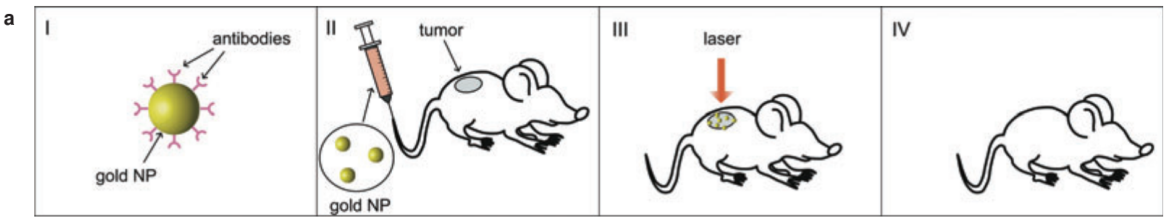

FIGURE 9.1: (online color at: www.lpr-journal.org) a) Schematic illustrating the usual approach in PPTT. First, gold NPs are functionalized with small molecules or antibodies that specifically target the cancer cells. Then, a NP solution is directly injected into the tumor location or intravenously through the tails of nude mice. After a given period of incubation, the tumor is illuminated to heat the NPs and generate hyperthermia. This procedure is repeated until healing occ

In 2008, Stern et al. carried out NP-based laser ablation on an apparent subcutaneous tumor around 1 cm in diameter (Fig. 9.1) [109]. In this work, gold NPs were introduce passive targeting via tail vein injection. Measurements were carried out on 46 tumors separated in 6 different groups corresponding to different conditions. Tumor necrosis or regression of 93% was observed for the group of mice that received 8.5 ml/g body weight, while the tumors of the mice that received a saline solution instead kept growing despite identical illumination conditions. In this work, the need for NP accumulation was emphasized. No discernible toxicity attributable to the gold NPs was identified. Since then, numerous studies have been carried out to push this initial proposal towards clinical trials [96]. Special attention has been given to investigating new particle geometries and their specific targeting to cancer cells. In recent years, the company Nanospectra (www.nanospectra.com) has initiated some clinical tests on head and neck cancer using gold nanoshells.

9.2 Nano-surgery

Laser surgery, which consists of using laser light to cut tissues, has become a reliable alternative to the conventional scalpel in fields such as ophthalmology and dermatology [110], [111]. It offers bloodless and more accurate cutting along with reduced risks of infection. At a smaller scale, laser light can be used as a tool to assist transfection of individual cells by forming a transient pore in the cell membrane that permits the introduction of either therapeutic agents (proteins, DNA, RNA) or imaging agents (fluorophores, quantum dots, nanoparticles) through the cell membrane and as a tool to cut individual neurons [112]. Optical transient poration in cell membranes has been demonstrated using a variety of illumination conditions, involving different mechanisms depending on the laser–cell interaction [113]. While CW illumination mainly induces a local heating at the cell membrane, femtosecond pulsed illumination with high repetition rate induces membrane permeability that is mainly the result of a low-density plasma originating from the generation of free electrons. Interestingly, this technique permits the study of one cell at a time. However, it suffers from potential photo-damage originating from the high laser power that is required. In this context, the use of plasmonic NPs makes it possible to locally increase the absorption and thus reduce the intensity requirements. Also, the possibility of controlling heating near few to single particles is expected to significantly reduce the dimension of the pore. Along this line, Urban and co-workers have recently proposed the use of a single gold NP,

trapped at the focus of a CW green laser, to perforate phospholipid membranes (Fig. 9.2) [114]. In their experiment, an 80 nm spherical gold NP was trapped and brought to a vesicle membrane. By increasing the laser intensity, the particle was heated until it crossed the membrane and penetrated the vesicle. The resulting pore was a few hundreds of nanometers in size and remained open for several minutes.

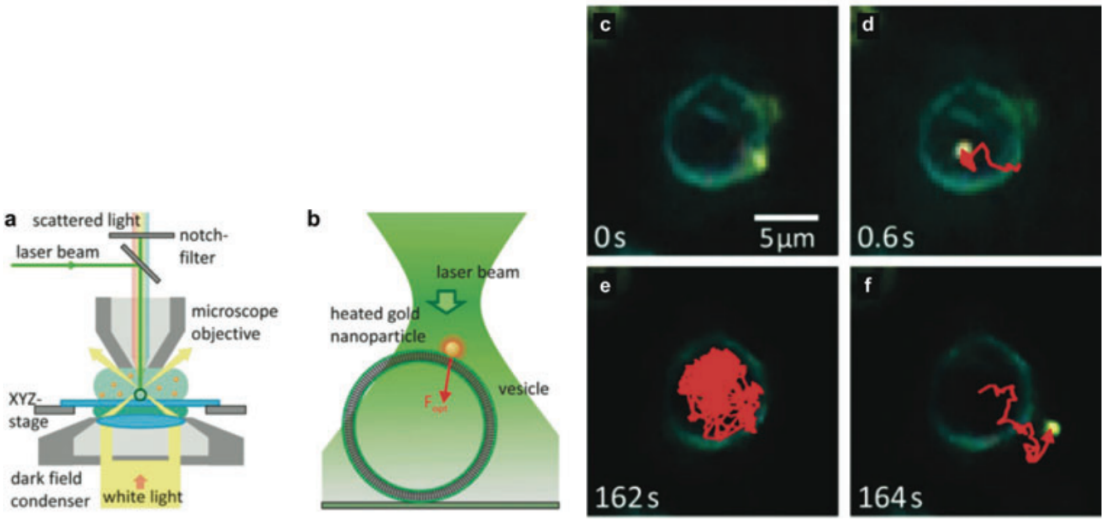

FIGURE 9.2: (online color at: www.lpr-journal.org) Illustration of the perforation of a phospholipid membrane using a trapped single gold NP. a) Schematic of the experimental setup used for optical injection and imaging [114]. b) Gold NPs are attached to the membrane of giant unilamellar vesicles prior to injection. The laser is defocused, resulting in a spot size of $6\mu m$ at the focal plane of the microscope objective. c) A dipalmitoylphosphatidylcholine vesicle before injection of a gold NP attached to the membrane. d,e) Tracking of the movement of the gold NP (red trace) shows it is confined to the inside of the vesicle. f) Often, after a certain time, the NP was observed leaving the vesicle at the same position at which it was injected. This suggests that the injection process forms a pore in the gel-phase membrane. (Reprinted with permission of ACS.)

9.3 Plasmonic photothermal delivery

Another biomedical application in thermo-plasmonics focuses on targeted delivery of drugs or genes for therapeutic purposes. The therapeutic agents are attached to gold NPs that act as nano-carriers through the human body. Once at the desired location, the active agents can be detached and released by remotely heating the NPs using laser illumination [115]–[117]. Hence, in this kind of application, plasmonic NPs have two roles: they act as both nano-carriers and nanosources of heat. This approach allows unprecedented control of the location, the timing, the duration and the magnitude of drug release. Sufficient incident light intensity must be used to release drugs or nucleotides, but must remain below the intensity threshold causing photothermal damage of cells and tissues [118]. Plasmonic photothermal delivery (PPTD) has been demonstrated using various geometries of plasmonic systems, such as nanospheres [119]–[121], nanorods [122]–[125], nanoshells [126], nanocages [127] and liposomes [128]–[130], as described below.

In 2005, the Yamada group demonstrated the feasibility of PPTD by using NIR pulsed

radiation to remotely control gene expression in specific Hela cells [131]. Those authors used gold nanorods functionalized with the gene related to the expression of GFP. Efficient gene release and expression was evidenced by monitoring the expression of GFP inside cells. Induced GFP expression was specifically observed in cells that were locally exposed to NIR radiation. In this work, the gene release was triggered by a morphological change of the NPs: under illumination, the nanorods melt and turn into spheres, which markedly reduces the NP interface available for keeping DNA strands attached. In 2006, the El-Sayed group used femtosecond-pulsed illumination at λ_0=400 nm combined with complexes formed by DNA strands covalently attached to spherical gold NPs [120]. Since no shape modification is expected in that case, it was suggested that gold–sulfur bond breaking is not only triggered by local heating but also by the transfer of hot electrons created within the metal. Another PPTD approach was proposed for the first time in 2007 by Paasonen et al. [128]. The idea was to use liposomes that can release their content under pulsed illumination. Gold NPs were incorporated into the lipid bilayer or the core of the liposomes to generate the photothermal effect required to induce the phase transition of the phospholipid membrane and its permeability. This approach can be advantageous as it can potentially make the drug delivery mechanism biologically more compatible. The use of liposomes or gold nanocages permits the conveyance of the therapeutic agent on the inside of the nano-carrier, as a cage.
In most of the PPTD experiments, the actual photoactivated process responsible of the release is not well identified. Recent experiments performed by the Halas group on gold nanoshells and nanorods aimed at discriminating the respective contribution of heat and hot electrons to the release mechanism in PPTD. It was shown that these contributions depend on the geometry of the NPs [126][132]. In 2009, the Halas group used gold nanoshells and a CW infrared laser to release single-strand DNA. In such an approach the dehybridization and release of DNA were triggered by the temperature increase of the medium surrounding the NPs [126]. In 2011, by comparing PPTD using gold nanorods and nanoshells, the same group came up with the conclusion that non-thermal mechanisms may play a role in plasmon resonant, light-triggered DNA release. In 2011, the Lapotko group proposed a novel PPTD approach that takes advantage of the formation of transient nanobubbles generated by gold NPs heated under pulsed illumination [121][100]. These nanobubbles could briefly open the cellular membrane and create an inbound transient jet that could inject extracellular molecules into individual specific cells without damaging them.

9.4 Photothermal imaging

When a metal NP is illuminated, the temperature increase experienced by the surrounding medium induces a local variation of refractive index. In 2002, Boyer et al. [133] took advantage of this effect to develop an optical microscopy technique aimed at detecting metal NPs ($\sim 10nm$) that are normally too small to be detected using any conventional optical microscopy. The local variation of the refractive index, also known as the nanolens effect [134], was detected by measuring the phase difference between two separated beams of an interferometer. One of the two beams propagates through the heated region while the other one serves as a reference. An improved signal over noise is achieved by modulating the heating laser using an acousto-optic modulator.

This approach originally led to the detection of 10 nm NPs, provided that their associated temperature increase reached $\sim 15K$. In this context, metallic NPs turn into efficient contrast agents that overcome many drawbacks of conventional fluorescent markers, such as autofluorescence, blinking, bleaching or fluorescence saturation. In 2003, Cognet and co-workers demonstrated that this technique could have valuable applications in biology [135]. Those authors managed to visualize single membrane proteins labeled with 10 nm gold NPs in fixed **COS7** cells. Because of the absence of photobleaching, the proteins can be visualized for arbitrarily long times, offering new opportunities for efficient protein tracking in three dimensions. This is a great advantage compared with regular fluorescent markers, which tend to photobleach very rapidly in tracking experiments. However, the authors pointed out that the high temperature increase required to obtain reasonable signal-tonoise ratio can induce damage to living biological systems. In 2004, Berciaud and co-workers solved this issue by improving the sensitivity by two orders of magnitude using heterodyne detection [136]. Using this new approach, gold NPs smaller than 5 nm could be detected with an associated local temperature increase of only 1 K. Such an achievement opened the path to experiments in living cells: in 2006, the same group reported on the real-time two-dimensional tracking of membrane protein in living **COS7** cells and neurons [137], and later of mitochondria [138]. In 2010, the Orrit group investigated the detection limit in photothermal microscopy. Those authors managed to detect a dissipated power of 3 nW from a single gold NP with a signal-to-noise ratio of 8, and an integration time of 10 ms. This corresponds to a less than 0.1 K surface temperature rise for a 20 nm diameter gold nanosphere (0.4 K for 5 nm) (Fig. 9.3). Very recently, the same group managed to push the sensitivity of this method by detecting single dye molecules instead of gold NPs [135].

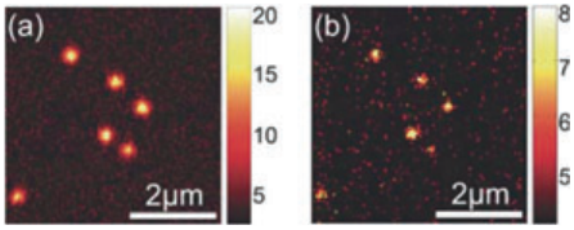

FIGURE 9.3: (online color at: www.lpr-journal.org) Photothermal imaging of 20 nm gold NPs in glycerol using a heating laser power of a) 9 μW (3 ms exposure time) and b) 1 μW (10 ms). Dissipated powers and temperature rises are 24 and 2.6 nW, and 0.7 K and 80 mK, respectively [139]. (Reprinted with permission of RSC.)

9.5 Photoacoustic imaging

In order to enable the early detection of cancerous lesions in situ, medical imaging techniques have to combine high resolution, high detection depth and high specificity to malignant tissues. On the one hand, optical imaging techniques usually provide a good contrast, but low resolution and penetration depth due to the diffusive nature of biological tissues. On the other hand, acoustic imaging techniques (like ultrasonography) lead to high penetration depth and resolution due to the relatively unhindered propagation of ultrasonic waves. However, such a full-acoustic approach suffers from

a low contrast between different tissues with similar acoustic properties. Photoacoustic (PA) (or optoacoustic) tomography combines the advantages of light and ultrasound to achieve the detection of deep tumors with high resolution ($< 1mm$) and contrast [140], [141]. The basis of PA tomography is the generation of acoustic signals using short laser pulses. Working with NIR light ensures a maximal light penetration in tissues. The absorption of a focused pulsed laser generates a rapid and localized temperature increase ($< 1^0C$). The subsequent thermal-induced expansion of the tissue triggers the formation and propagation of an acoustic wave (or stress wave) that can be detected at the surface of the body by using an array of ultrabroad-band acoustic transducers. Finally, a deconvolution algorithm is used to render a three-dimensional image of the absorbing tissues. Since hemoglobin usually has orders of magnitude larger absorption than surrounding tissues, PA imaging is often used to visualize blood vessels or abnormal angiogenesis (formation of new blood vessels from existing ones) in advanced tumors. Low acoustic attenuation allows the detection of tumors 5 to 6 cm deep, typical of breast or prostate cancers. The duration and time of arrival of the acoustic signal to the ultrasonic detector reveals the size and location of the target. In early stages of disease, however, angiogenesis is not sufficient to differentiate cancer tissues from healthy ones. The use of plasmonic NPs as efficient photoabsorbers to enhance PA contrast was first proposed in 2004 by Copland et al. [141]. Those authors demonstrated the concept by performing in vitro experiments on breast cancer cells embedded in a gelatin phantom designed to mimic breast tissue. Spherical 40 nm gold NPs were bound to the cancer cells via active targeting. In 2007, the first gold-NP-assisted PA signal in vivo was reported by the same group [142]. In this work, gold nanorods were used to enhance the photothermal contrast in the infrared region and were simply injected subcutaneously at a specific region in a mouse. In 2009, Zhang and co-workers conducted passive targeting experiments on living mice [143]. The authors used PEGylated spherical gold NPs injected via the tail vein and illuminated at 532 nm. The accumulation of gold NPs in the tumor location via passive targeting was evidenced. In the same year, Wang et al. addressed a field of research different from oncology [144]. They managed to image macrophages in atherosclerotic plaques. Mouse monocytes– macrophages, which are characterized by a high rate of non-specific uptake, were incubated with PEGylated NPs overnight. Interestingly, multiple wavelength illumination was used to discriminate between NPs internalized by the microphages that accumulated to form clusters from individual NPs that were not internalized. Recently, alternative NP geometries have demonstrated enhanced PA contrast. For instance, nanocages led to an enhancement of the PA signal due to their extraordinarily enhanced absorption crosssection (Fig. 9.4)[145].

In the case of silica-coated gold nanorods, it was suggested that the reduction of the gold interfacial thermal resistance with the solvent due to the silica coating could contribute to a stronger PA signal [146]. Note that in PA experiments using gold NPs, the actual origin of the acoustic waves remains unclear. In particular, the possible occurrence of cavitation and bubble formation has not been clearly evidenced. The thermodynamics at the vicinity of metallic gold NPs under pulsed illumination is a very intricate problem that is still under active investigation.

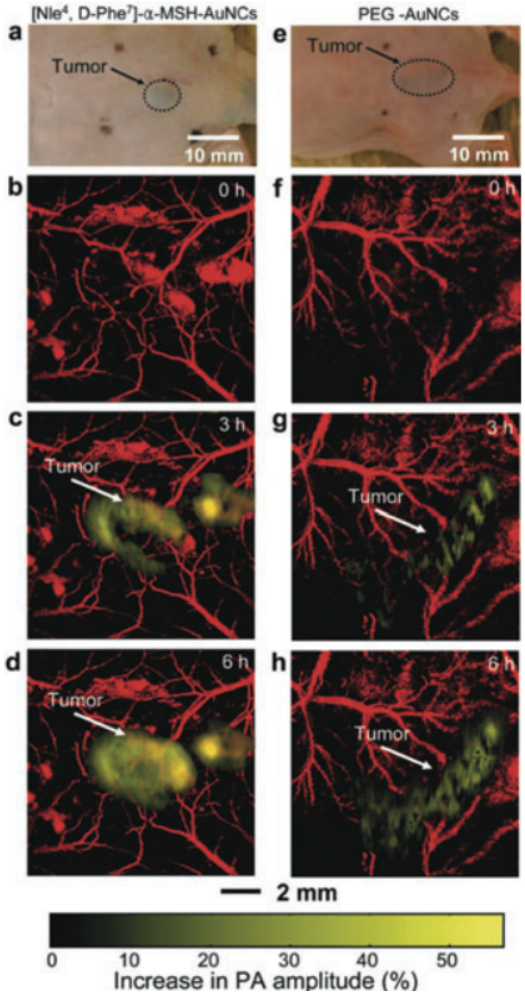

FIGURE 9.4: (online color at: www.lpr-journal.org) In vivo non-invasive PA images of B16 melanomas using gold nanocages [145]. Photographs of nude mice transplanted with B16 melanomas before injection of a) bioconjugated and e) PEGylated nanocages. PA images of the B16 melanomas after intravenous injection with 100 μl of 10 nM b–d) bioconjuated and f–h) PEGylated nanocages through the tail vein. Color scheme: red, blood vessels; yellow, increase in PA amplitude. (Reprinted with permission of ACS.)

9.6 Plasmon-assisted optofluidics

Accurate manipulation of fluids in integrated micrometric channels, known as microfluidics, is a fast-growing field that has become a key ingredient in the development of future miniaturized analytical devices. There is much current expectation for incorporating in a microfluidic platform all necessary components and functionalities to achieve a labbon-a-chip capable of performing parallel chemical and biological analyses. Along this direction, different approaches are considered in order to control fluid dynamics through elementary operations including fluid routing and mixing. Among the various strategies, photo-heating is attractive owing to its simplicity, its being free of any complex microfluidic designs, pumps, valves or electrode patterning. Two main thermal effects leading to light-induced fluid motion can be potentially exploited: thermocapillary forces and Marangoni convection. On the one hand, the thermocapillary force applies at a fluid–gas interface. It results from the dependence

of the surface tension on the temperature. For instance, Baroud et al. managed to guide and sort droplets in microfluidics channels using a focused laser beam [147]. On the other hand, Marangoni convection is characterized by an upward (Archimedes) fluid convection resulting from a decrease of the mass density of the fluid under heating.
Once again, using plasmonic nanostructures for this purpose appears as the most natural means to enlarge the potential of this field of research. In 2005, Farahi et al. proposed enhancing the thermocapillary effect by using a surface plasmon polariton (SPP) supported by a flat gold film[148] . More precisely, those authors managed to manipulate droplets of silicone oil and glycerol via surface tension driven forces sustained by surface plasmon de-excitation energy. Along the same lines, Liu and co-workers proposed an approach in which fluid heating was enhanced by dispersing plasmonic NPs in the liquid (Fig. 9.4) [149]. In their experiment, the fluid was pulled at velocities as high as 500 $\mu m/s$ within a microfluidic channel by displacing the laser beam. This approach was also successfully used to route fluids at microfluidic junctions.

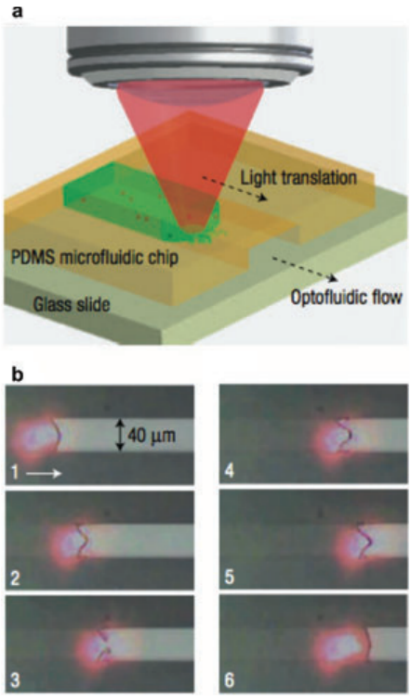

FIGURE 9.5: (online color at: www.lpr-journal.org) LSP-assisted optofluidic control in straight microfluidic channels [149]. a) Illustration of the experimental system configuration. b) Optofluidic control in a 40 μm wide channel. The video prints show that the flow of the fluid containing gold NPs follows the optical guiding of a 10 mW, 785 nm laser spot at a speed of 50 $\mu m/s$ (frames 1–5) and stops otherwise (frame 6). (Reprinted with permission of NPG.

Moving a fluid through microscale thermal-induced convection using a gold nanostructure (Marangoni convection) has been investigated experimentally by Garces-Ch ´ avez and ´ co-workers. Those authors demonstrated that Marangoni convection (combined with thermophoresis) induced by a SPP at a flat gold film can be used to self-assemble a large number of colloidal microparticles on a substrate [150]. Similarly, Miao et al. achieved fluid mixing near a surface patterned with a monolayer of

plasmonic NPs supporting LSP [151]. Recently, Donner and co-workers have theoretically studied the photothermally induced fluid convection around plasmonic structures [152]. In particular, all the orders of magnitude of temperature and fluid velocity were discussed as a function of the morphology of the plasmonic structure and the illumination conditions (Fig. 9.5). Characteristic temperature, velocity, spatial scales and time scales depend on the dimensions of the plasmonic structure and on the delivered heat. For instance, the resulting characteristic fluid velocity at the vicinity of the structure is given by

$$\tilde{V} \sim R^2 \rho \beta g \delta T / \eta \tag{9.1}$$

where g is the gravitational acceleration, δT the temperature increase of the structure, β the dilatation coefficient of water and η the dynamical fluid viscosity. While the fluid velocity is negligible (10 nm/s) for nanometer-sized structures due to a very small Reynolds number, it plays a significant role for either micrometer-sized plasmonic structures or assemblies of nanostructures. Note that, at the considered scales, equilibrium is reached very fast, typically after 1 ns to 1 μs, depending on the size of the structure but not on the temperature increase.

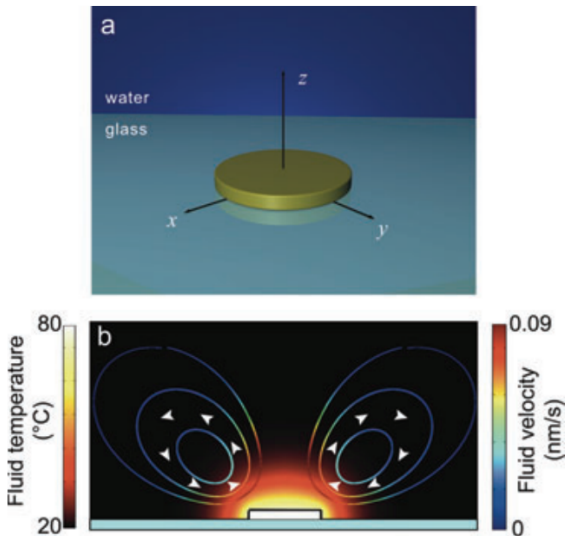

FIGURE 9.6: (online color at: www.lpr-journal.org) Thermal-induced fluid convection using a single gold disc. a) Representation of the system: a gold disc, 500 nm in diameter and 40 nm thick, immersed in water. b) Side view of the temperature distribution and the thermal-induced fluid velocity field of the fluid surrounding the gold nanodisc (numerical simulations) [152]. (Reprinted with permission of ACS.